# A SIMPLIFIED MODEL FOR LATERAL RESPONSE OF CAISSON FOUNDATIONS

A Thesis
Presented to
The Academic Faculty

by

VARUN

In Partial Fulfillment
Of the Requirements for the Degree
Master of Science in Civil Engineering

Georgia Institute of Technology
DECEMBER, 2006

# A SIMPLIFIED MODEL FOR LATERAL RESPONSE OF CAISSON FOUNDATIONS

Approved by:

Dr. Dominic Assimaki, Advisor
School of CEE (Geosystems)
*Georgia Institute of Technology*

Dr. Paul Mayne
School of CEE (Geosystems)
*Georgia Institute of Technology*

Dr. Glen Rix
School of CEE (Geosystems)
*Georgia Institute of Technology*

Dr. Reignald DesRoches
School of CEE (SEMM)
*Georgia Institute of Technology*

Date Approved: November 17, 2006

To My Parents

# ACKNOWLEDGEMENTS

I wish to thank my advisor, Dr. Dominic Assimaki for her thoughtful guidance and advice during the research. Several teachers including Dr. Santamarina, Dr. Rix, Dr. Assimaki and Dr. Mayne helped with the foundation of this research by means of courses that provided insight as well as useful tools for this research. The discussions with research group partner, Wei Li were also very productive. Special thanks to Information Systems Group (ISG) for excellent support and troubleshooting with software applications.

More importantly, I would like to thank my parents, sister and old friends for their love, support and encouragement throughout these years.

# TABLE OF CONTENTS

# LIST OF TABLES

## LIST OF FIGURES

# LIST OF SYMBOLS AND ABBREVIATIONS

| | |
|---|---|
| $D$ : | Depth of pier/caisson foundation |
| $B$ : | Diameter of pier/caisson foundation |
| $E$ : | Elasticity modulus of soil |
| $E_p$ : | Elasticity modulus of pier |
| $G$ : | Shear modulus of soil |
| $\nu$ : | Poisson ratio of soil |
| $D'$ : | Material Damping Ratio |
| $P_k$ : | Lateral resistance per unit length along shaft of pier |
| $P_b$ : | Lateral base resistance |
| $M_k$ : | Resisting moment per unit length along shaft of pier |
| $M_b$ : | Base resisting moment |
| $r$ , $z$ , $\psi$ : | Cylindrical coordinate system |
| $\sigma_r$ : | Normal stress in radial direction |
| $\sigma_z$ : | Normal stress in z direction |
| $\tau_{r\psi}$ , $\tau_{rz}$ : | Shear stresses in radial direction on planes z and $\psi$ planes |
| $k_x$ and $k_x^*$ : | Static and complex dynamic lateral distributed translational spring |
| $k_\theta$ and $k_\theta^*$ : | Static and complex dynamic lateral distributed rotational spring |
| $k_{bx}$ and $k_{bx}^*$ : | Static and complex dynamic base translational spring |
| $k_{b\theta}$ and $k_{b\theta}^*$ : | Static and complex dynamic base rotational spring |
| $V$ : | Horizontal Load |
| $M$ : | Overturning Moment |
| $u$ : | Displacement |

$u_t$: Displacement or translation at top of pier

$\theta$: Rotation of the pier

$K_{xx}$ and $K^*_{xx}$: Static and complex dynamic global translation stiffness

$K_{xr}$ and $K^*_{xr}$: Static and complex dynamic global coupled stiffness

$K_{rr}$ and $K^*_{rr}$: Static and complex dynamic global rocking stiffness

$f$ : Frequency of excitation/wave

$\omega$: Circular frequency of excitation/wave

$\rho$ : Density of material

$V$ : Wave velocity

$\sigma_i$ : Stress at a point (node)

$\dot{u}_i$ : Velocity at the point (node)

$\alpha$ : Mass proportional damping

$\beta$ : Stiffness proportional damping

$\alpha'$ : Coefficient to characterize attenuation of waves

$A(\omega, x)$ : Attenuation function for wave amplitude

$a_o$ : Dimensionless frequency

$t$: Time

$T$ : Time period of a wave or vibration

$\kappa$: Ratio of maximum element size in the mesh to diameter of pier

$\lambda$: Wavelength of wave

$U_b$: Displacements in free field

$U_b^*$: Modified displacements due to presence of foundation

$S_b$: Stresses in free field

| | |
|---|---|
| $S_b^*$: | Modified stresses due to presence of foundation |
| $X$ : | Frequency dependent dynamic impedance matrix of free-field |
| $u_V$ : | Displacement at top of pier upon the application of a unit force |
| $\theta_V$ : | Rotation of the rigid pier upon the application of a unit force |
| $u_M$ : | Displacement at top of pier upon the application of a unit moment |
| $\theta_M$ : | Rotation of pier upon the application of a unit moment |
| $e$ : | The embedment depth of shallow foundations |
| $R$ : | Radius of circular foundation |
| $H$ : | Thickness of soil layer |
| $V_s$ : | Shear wave velocity of the medium |
| $k_x'$ : | Lateral side resistance dynamic stiffness coefficient |
| $k_{bx}'$ : | Lateral base resistance dynamic stiffness coefficient |
| $k_\theta'$ : | Rotational resistance dynamic stiffness coefficient |
| $C_x$ : | Attenuation coefficient for lateral side resistance |
| $C_{bx}$ : | Attenuation coefficient for lateral base resistance |
| $C_\theta$ : | Attenuation coefficient for rotational side resistance |
| $u*$ : | Complex Displacement (magnitude and phase) |
| $\theta*$ : | Complex rotation (magnitude and phase) |
| $u_{ff}$ : | Free field translation |
| $\theta_{ff}$ : | Free field rotation |
| $H_u(a_o)$ : | Transfer function for translational motion at top of pier |
| $H_\theta(a_o)$ : | Transfer function for rocking motion of pier |

# SUMMARY

Caisson, pier or drilled shaft foundations are encountered as part of the foundation system of tall structures such as bridges, transmission towers, heliostats, etc, and correspond to rigid blocks of length-to-diameter (D/B) ratio on the order of D/B = 2-6. As a result of their geometry and stiffness characteristics, the mechanisms of load transfer from the superstructure to the surrounding soil and their kinematic response to seismic wave propagation are governed by a complex stress distribution at the pier-soil interface, which cannot be adequately represented by means of simplified Winkler models for shallow foundations or flexible piles. Continuum model solutions, such as 3D finite elements (FE), may be employed to simulate this complex soil-structure problem, but are infrequently employed in practice for the design of non-critical facilities due to the cost and effort associated with these analyses. Prompted by the drawbacks of simplified and elaborate models available for the design of caisson foundations, the objective of this work is to develop a Winkler-type model for the analysis of transversely-loaded caissons, which approximately accounts for the complex soil resistance mechanisms mobilized at the base and the circumference of these elements, while retaining the advantages of simplified methodologies for design at intermediate levels of target accuracy. Investigation of the governing load-transfer mechanisms and development of complex spring functions is formulated on the basis of 3D FE simulations. Initially, the soil-structure stiffness matrix is computed by subjecting the pier to transverse static and dynamic loading at the top, and numerically estimating the response. Complex frequency-dependent functions are next developed for the spring constants by equating

the stiffness matrix terms to the analytical expressions developed for the four-spring model. Sensitivity analyses are conducted for optimization of the truncated numerical domain size, finite element size and far-field dynamic boundary conditions to avoid spurious wave reflections; the latter is ensured by means of a so-called “sponge” layer of progressively increasing viscous damping to simulate the infinite domain energy radiation damping. Simulations are next conducted to evaluate the transient response of the foundation subjected to vertically propagating shear waves, and results are compared to the response predicted by means of the 4-spring model. Finally, the applicability of the method is assessed for soil profiles with depth-varying properties. While the methodology developed is applicable for linear elastic media with no material damping, the expressions of complex spring functions may be extended include material hysteretic energy absorption (damping), nonlinear soil behavior and soil-foundation interface separation, as shown in the conclusion of this study.

# CHAPTER 1

# INTRODUCTION

## 1.1 Pier foundations

Pier, caisson or drilled shafts are terms typically used interchangeably to describe permanent substructures or foundation elements which are either prefabricated and sunk into position, thus providing excavation support by protecting the walls against water pressure and soil collapse, or are cast in-situ at soil or rock sites.

These massive concrete foundation elements always require steel reinforcement, and occasionally also comprise a steel casing or jacket. The term corresponds to a wide range of foundations, generally classified with respect to their dimensions and geometry as:

(a) Deep or shallow, depending on the depth of foundation;

(b) Small or large, depending on the diameter of foundation; and

(c) Circular, square or rectangular, depending on the geometry of their cross section.

Typical pier or caisson foundations are characterized by a diameter on the order of 2-12 feet and depth to diameter ratio in the range between 2- 15. As can be readily seen, their embedment depth is larger than the corresponding depth of shallow embedded foundations, and lower than typical values of pile foundations. **Figure 1.1** depicts schematically the dimensional and geometrical differences between the alternative foundation element types, namely shallow, caisson and pile foundations.

Large diameter caisson foundations are used for the most part as bridge foundation elements, as well as deep-water wharves, and overpasses. On the other hand, small caissons are extensively encountered either as single foundation components of transmission towers (power lines or cellular towers) and heliostats, or in groups as part of the foundation system of high rise buildings, multi-storey parking decks and most importantly scour vulnerable structures. A typical bridge foundation system, comprising both caisson and pile group foundation elements is illustrated in **Figure 1.2**.

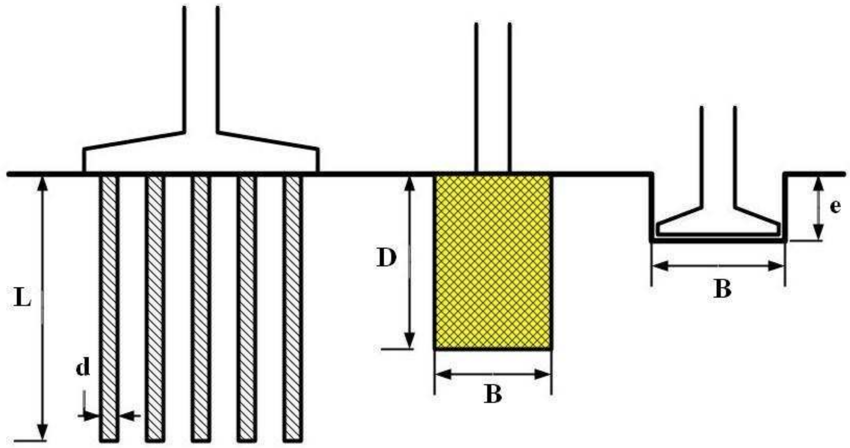


**Figure 1.1** Comparison between relative dimensions of different types of foundations.

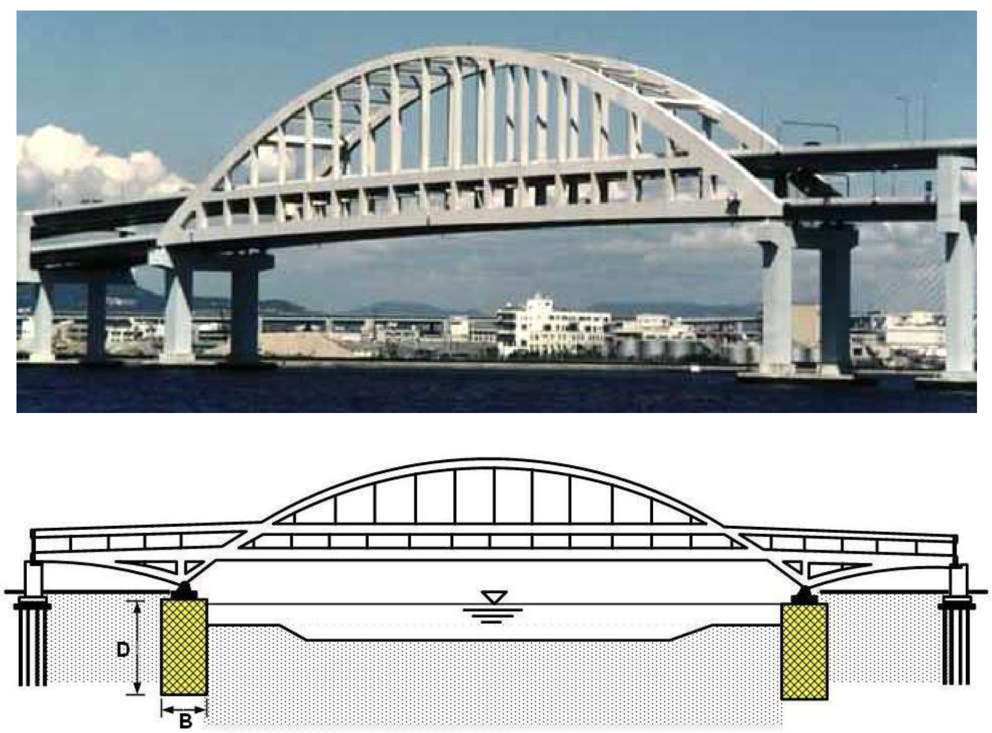


**Figure 1.2** Use of caisson foundation in bridges: the Rokko Island Bridge in Kobe, Japan, a double-deck loose arch bridge of length 217m, constructed in 1992

Alternatively, drilled shafts are also used for purposes such as slope stabilization, foundation for transmission towers, foundation elements in the vicinity of existing structures, cantilever or tie-back walls, foundations at marine sites and navigation aid systems; the alternative applications of caisson foundations are schematically shown in **Figure 1.3**. For further information, the reader is referred to O'Neil and Reese (1999).

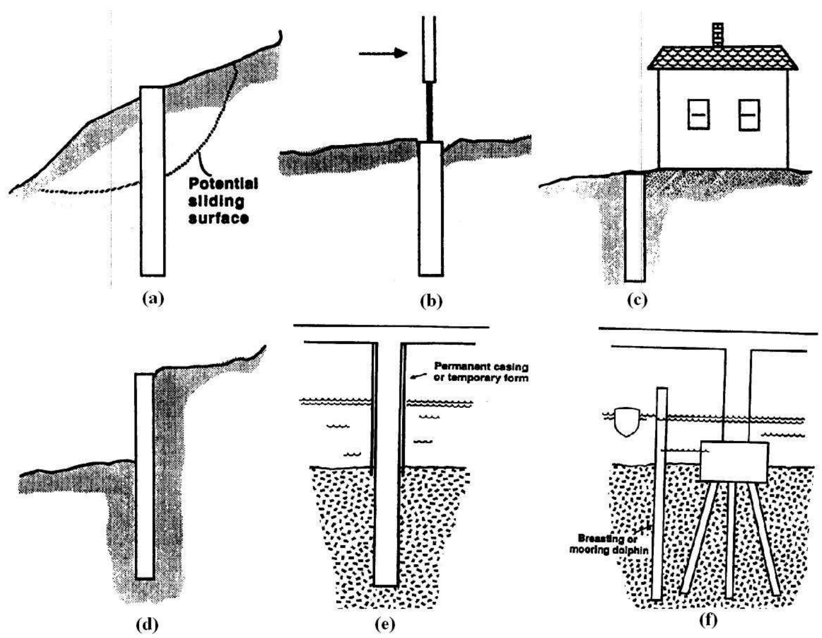


**Figure 1.3** Uses of drilled shafts (a) Stabilizing a slope (b) Foundation for transmission tower (c) Foundation near existing structure (d) Closely spaced shafts to serve as a cantilever or tie-back wall (e) foundation at marine site (f) Pier protection or navigation aid (O'Neil and Reese, 1999).

### 1.2 Advantages of pier foundations

Drilled shafts are highly versatile in constructability for a wide variety of soil formations, and can be installed in virtually any soil type including residual soils, karstic formations, soft soils and marine sites (O'Neil and Reese, 1999). Among other advantages of these elements, no dewatering is necessary upon installation in soft soils or for sites where excessive groundwater is considered to be critical for the selection of the excavation and support method. Instead, bentonite slurry or steel casings are used to stabilize the excavation pit, and concrete is pumped using ‘slurry displacement’ or ‘underwater placement’ method.

Other advantages include the high capacity of single elements in axial as well as lateral loading, which enables large diameter caissons to effectively replace pile groups and renders *drilled shafts* a popular choice for structures anticipated to be subjected to significant lateral loads. It should be noted herein that when caisson foundations are selected instead of using pile groups, the structural columns may be directly connected to the foundation, thus eliminating the need for pile caps.

In a thorough review of the applicability and advantages of caisson foundations, O’Neil and Reese (1999) also present case studies which demonstrate large economic savings through the selection of caisson foundations or drilled shaft as alternative methods to regular design methodologies, when the structure and site conditions enable such an option.

Due to all the aforementioned advantages of these foundations, including the ease of construction, caisson or pier foundations are used extensively in the United States and world wide, particularly by private or public agencies that focus on the design and construction of lifelines in a wide variety of site conditions, such as the Departments of Transportation in the US.

### 1.3 Design methodologies for pier foundations

The main advantage of caisson foundations compared to shallow or pile foundations is the high lateral load carrying capacity of single members. For static load design purposes, load-deflection curves (often referred to as p-y curves) are employed for the estimation of their bearing capacity, typically obtained by means of empirical correlations for different soil types which are based on results of lateral load tests. In the current state-of-practice, many commercial software packages are available for the purpose, facilitating thus the design process. As an example, Lam and Chaudhury (1997) present such p-y curves, further modified to account for the effect of cyclic loading and thus extend the approach to seismic loading. However, almost all the methods follow the same semi-empirical approach as used for flexible pile foundations.

Nonetheless, it can be readily seen that for intermediate D/B ratios, the pier foundations are more likely to behave as rigid elements rather than as a flexible piles (see also **Figure 1.1**). Thus, a design approach similar to rigid embedded shallow foundations seems more reasonable. Analytical solutions that provide the response such foundations to lateral loading have been developed by Elsabee and Morray (1977), Kausel (1974) and Wolf (1997), restricted -however- to low embedment depths.

Compared to shallow foundations, soil-structure interaction effects for pier foundations that comprise the load-transfer mechanisms from the superstructure to the surrounding soil, and the potential altering of loads transferred through the foundation from the soil to the structural elements (e.g. during seismic motion) are associated with a much more complex stress distribution at pier-soil interface. Continuum model solutions like 3D finite element methods (FEM) are feasible but are rarely employed in practice for the design of non-critical facilities due to the associated site investigation cost, computational time, and user expertise required. Nonetheless, dynamic Winkler models that properly account for the multitude of soil resistance mechanisms mobilized at the base and the circumference of laterally loaded piers may be used to predict the dynamic response of these foundations, given an intermediate level of target design sophistication.

The main objective of this research project is to develop an improved and simplified methodology for the analysis of pier foundations (drilled shafts) of intermediate length subjected to lateral dynamic loading, which, while retaining the advantages of Winkler-type models will allow for realistic representation of the complex soil-structure interaction effects associated with these foundation elements.

In particular, this work comprises the development and application of a Winkler-type model for pier foundations, based on results obtained by means of 3D FE analyses, and involves the following steps:

1. Formulation of global stiffness matrix at the top of pier for the four spring Winker Model
2. Calibration of springs for static loading and sensitivity to Poisson ratio using numerical simulations
3. Calibration of springs as a function of dimensionless frequency for dynamic loading
4. Analytical solution for transfer functions to account for kinematic interaction and their comparison with numerical results
5. Sample calculations to demonstrate application to multi layered soil profiles and comparison with numerical results

# CHAPTER 2

# OVERVIEW OF SOIL-STRUCTURE INTERACTION METHODOLOGIES

## 2.1 Definition

Soil-structure interaction is the mechanism that accounts for the flexibility of the foundation support beneath the structure and potential variations between foundation and free-field motions. It determines the actual loading experienced by the structure-foundation-soil system resulting from the free-field seismic ground motions.

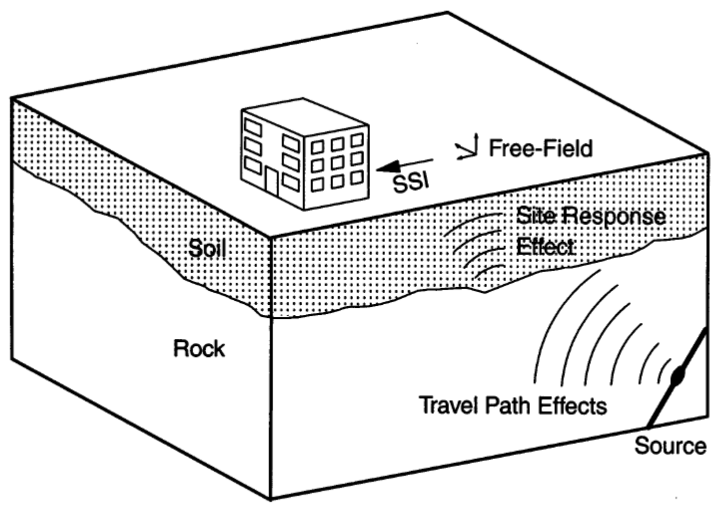


**Figure 2.1** Context of SSI in engineering assessment of seismic loading for a structure (Stewart et al. 1998)

## 2.2 Components of the soil-structure interaction

During a dynamic loading like ground shaking during an earthquake, the deformations of a structure are affected by interactions between three linked systems: the structure, the foundation, and the geologic media (soil and rock) underlying and surrounding the foundation. A soil-structure interaction (SSI) analysis evaluates the collective response of these systems to a specified free-field ground motion (**Figure 2.2a**). Two physical phenomena comprise the mechanisms of interaction between the structure, foundation, and soil:

(a) *Inertial interaction*: This mechanism refers to the response of the complete structure-foundation-soil system to excitation by D' Alembert forces associated with the acceleration of the super-structure due to kinematic interaction as shown in **Figure 2.2b**.

(b) *Kinematic interaction*: Provided that the principle of superposition can be applied -at least approximately- the mass of structure in this mechanism is set as zero and there are no inertial effects. Nonetheless, the presence of stiff foundation elements either on the formation or embedded in the underlying soil, may result in the deviation of the foundation motion with respect to the corresponding motion of the so-called *free-field*, namely the response of the soil formation in absence of the structure (**Figure 2.2c)**. Three mechanisms can potentially contribute to such deviations (Stewart et. al, 1998):

   i. <u>Base-slab averaging</u>: Free-field motions associated with inclined and/or incoherent wave fields are "averaged" within the footprint area of the base -slab due to the kinematic constraint of essentially rigid-body motion of the slab.

   ii. <u>Embedment effects</u>: The reduction of seismic ground motion due to embedment. Since the foundation is rigid and cannot deflect in exactly the same shape as far-field, the far field motion is filtered by the foundation depending on the wavelength of excitation. This is similar to 'Base Slab' averaging effect but is observed in case of coherent wave fields as well.

   iii. <u>Wave Scattering</u>: Scattering of seismic waves off of corners and asperities of the foundation.

The effect of kinematic interaction is generally captured by complex-valued transfer functions, namely functions that relate the free-field motion to foundation response.

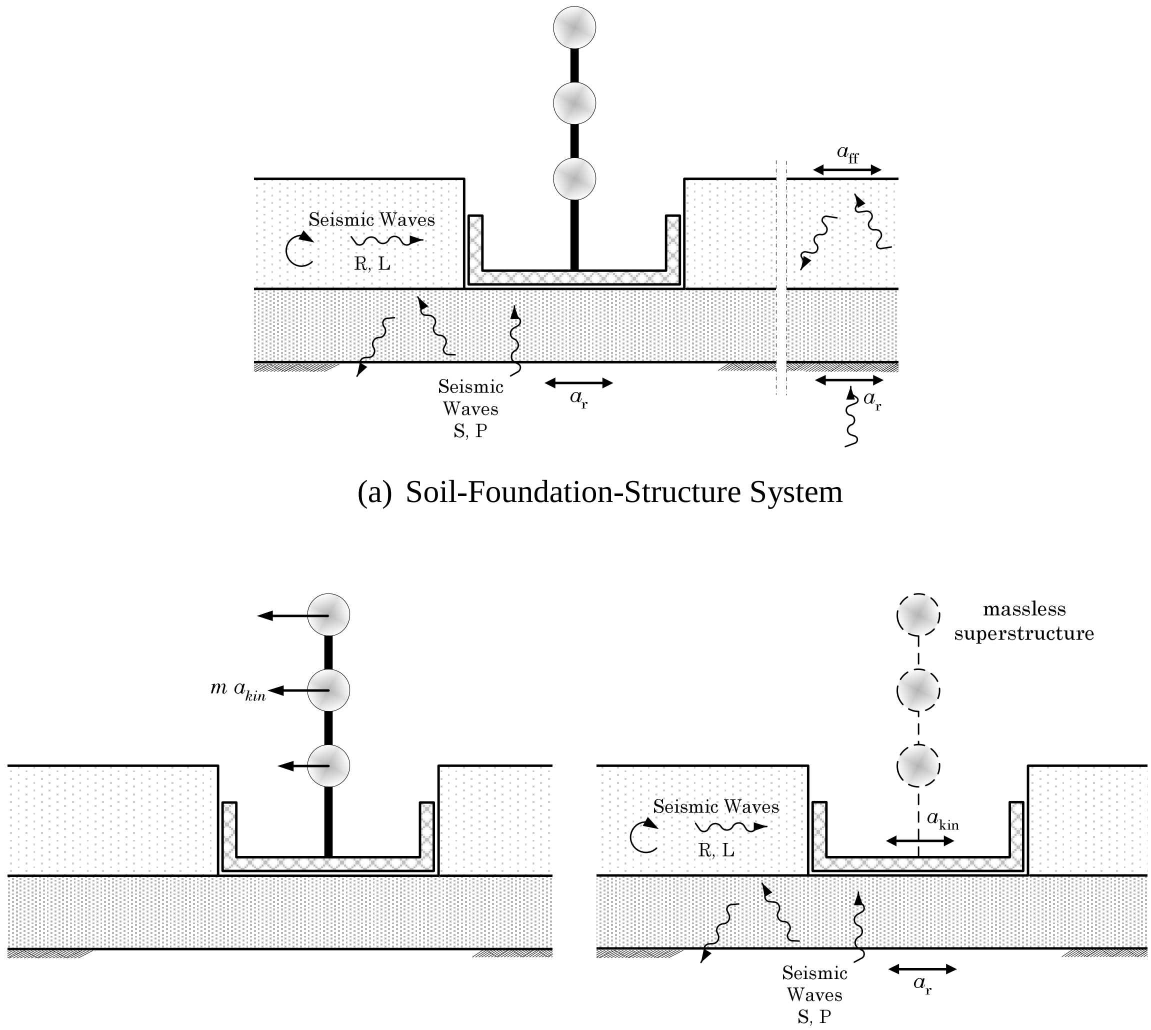


(a) Soil-Foundation-Structure System

(b) Inertial Interaction

(c) Kinematic Interaction

**Figure 2.2** Geometry and decomposition of a soil-structure interaction problem

In the case of linear elastic or moderately nonlinear soil-foundation systems of surface or embedded foundations, inertial interaction analysis (**Figure 2.2b**) may be conveniently performed in two steps as shown in **Figure 2.3** (after Kausel & Rosset, 1975):

(a) Compute the foundation dynamic impedances (springs and dashpots) associated with each mode of vibration

(b) Determine the seismic response of structure and foundation supported by these springs and dashpots and subjected to the kinematic accelerations of the base.

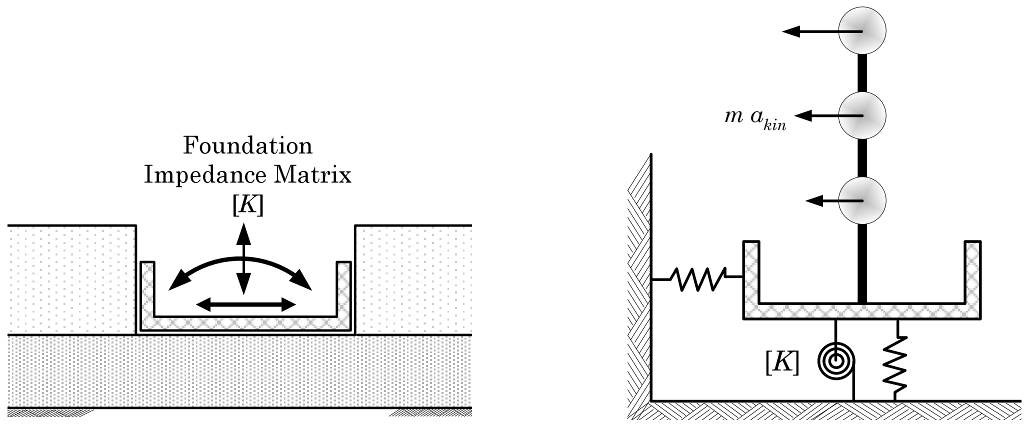


**Figure 2.3** Schematic representation of two-step inertial interaction analysis

The dynamic impedance is a complex function, where the real and imaginary parts represent the dynamic stiffness and energy attenuation of the system, respectively. The attenuation represented by the imaginary part of the impedance function is a consequence of hysteretic damping in the soil and foundation, and radiation of seismic energy away from the foundation through the soil. Generally it is the radiation damping that mostly dominates the imaginary part because the energy loss due to hysteretic damping is quite small (5-10%). In most cases the analytical expressions are derived for elastic medium with no damping and then the damping is taken into account using the correspondence principle by multiplying the impedance function with (1+i2D'), where D' is the coefficient of material damping.

As can be readily seen, accounting for the effects of soil-structure interaction may significantly alter the predicted response of the soil-foundation-structural system, a fact that renders these phenomena critical in engineering design. It should be also noted that for the fictional condition of an infinitely stiff soil, the amplitude of the transfer function for translational motion is unity and the phase is zero (i.e. the foundation and free-field motions are identical), and the impedance function has infinite real part and zero imaginary part. As a result, ignoring the effects of soil-structure interaction effects (which is common practice in structural design) inherently implies the unrealistic assumption of an infinitely rigid underlying soil medium.

### 2.3 Methodologies for Soil-Structure Interaction Analysis

The general methods to quantify soil structure interaction effects are:

*Direct approach*: In a direct approach, the soil and structure are simultaneously accounted for in the mathematical model and analyzed in a single step. Typically, the soil is discretized with solid finite elements and the structure with finite beam elements. Since assumptions of superposition are not required, true nonlinear analyses are possible in this case. Nonetheless, the analyses remain quite expensive from a computational standpoint. Hence, direct SSI analyses are more commonly performed for structures of very high importance and are not employed for the design of regular structures.

*Substructure approach*: In a substructure approach, the SSI problem is decomposed into three distinct parts discussed above which are combined to formulate the complete solution. The superposition principle is exact only for linear soil, foundation and structure behavior. Nevertheless, approximations of soil nonlinearity by means of iterative wave propagation analyses allow the superposition to be applied for moderately-nonlinear systems. The principal advantage of the substructure approach is its flexibility. Because each step is independent of the others, it is easy to focus resources on the most significant aspects of the problem.

For each one of the three analysis steps, several alternative formulations have been developed and published in the literature, including finite-element, boundary-element, semi-analytical and analytical solutions, a variety of simplified methods, and semi-empirical methods. In addition to the dynamic finite element methods, the most popular approaches used in practice for the analysis of soil-structure interaction problems are briefly presented in the ensuing:

(a) Boundary element type methods: The methods of this class are essentially semi analytical in the sense that they use closed-form solutions to the pertinent wave equations for the soil domain, and discretize only the boundaries and interfaces of the system. These closed-form solutions (referred to as fundamental solutions or Green's functions depending on the particular solution) have the ability to reproduce exactly the radiation of wave energy to infinity, without requiring special lateral boundaries –as is the case for the finite element methods. Evidently, this class of methods is the most versatile in treating a variety of incident wave fields (such as inclined body waves and Rayleigh waves, in addition to vertical waves). Usually however, they cannot accommodate material and interface nonlinearities associated with foundation seismic motion. Therefore in current state of practice, such sophisticated tools are also used in conjunction with finite element methods, which can better model the nonlinear soil-structure response.

(b) Winkler models: Used primarily for the inertial interaction analysis, the foundation in these methods is supported by a series of independent vertical, rotational and horizontal springs and dashpots along the soil-footing interface, which correspond to the vibration modes. For elastic analyses, the most important factors affecting the dynamic impedance of foundations are: (i) the shape of the foundation; (ii) the stratigraphy (homogeneous halfspace, surface soil layer over rigid bedrock or halfspace); and (iii) the amount of embedment.

For the estimation of the dynamic impedance of footings, algebraic expressions have been developed that account for arbitrary foundation shape and degree of embedment, and for a variety of soil conditions. For more details, the reader is referred among others to Dobry & Gazetas (1986), Wong & Luco (1985), Gazetas (1983), Kausel & Roesset (1975) and Luco (1974).

In these studies, the dynamic impedance of foundations is shown to be very sensitive to the underlying soil stratigraphy. The response of a foundation on a non-homogeneous halfspace can be substantially different from the response of an identical foundation resting on a homogeneous halfspace. This effect arises both from the increase of static stiffness and the decrease of radiation damping and is more prominent for the vertical and horizontal oscillations. Subsequently, the amplitude of the motion to be exerted by the supported structure increases as a result of the resonant peaks which appear in the amplitude-frequency response curves (Kausel 1974, Kausel & Ushijima 1979, Gazetas 1983)

# CHAPTER 3

# WINKLER TYPE MODEL FOR ANALYSIS OF CAISSON FOUNDATIONS

## 3.1 Stress Distribution on Pier-Soil Interface

When a lateral load is applied to a pier foundation, the stress distribution at the pier-soil interface is as shown in **Figure 3.1**.

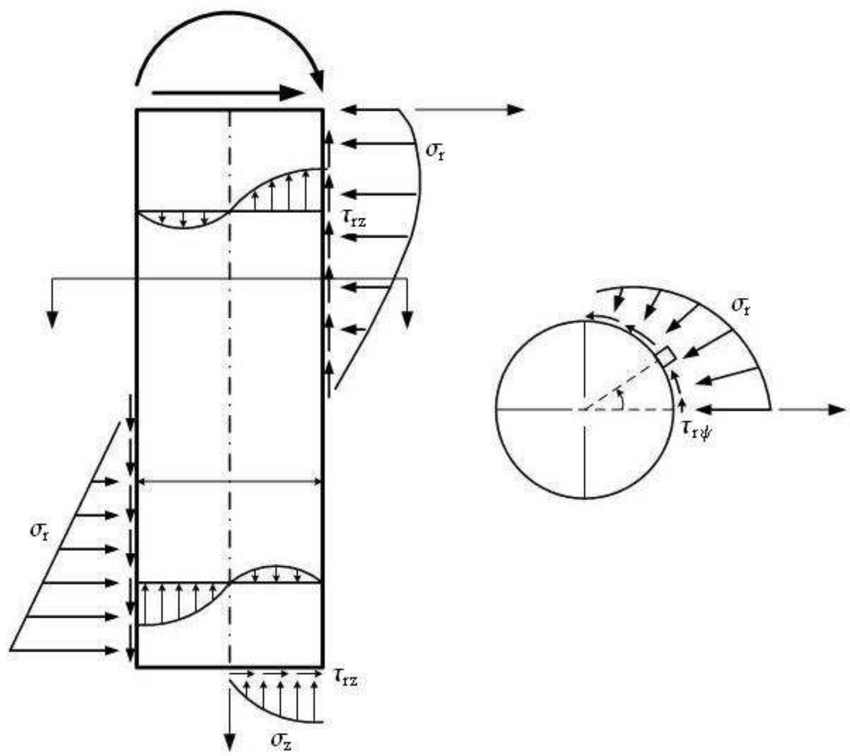


**Figure 3.1** Various mechanisms of soil resistance on lateral loading

Four mechanisms are identified that can contribute significantly to the pier response. The mathematical expressions for the resistance mobilized by these mechanisms are presented below and comprise the following:

(a) *Lateral resistance per unit length* due to normal stresses along the shaft:

$$P_h = \int_0^{2\pi} [\sigma_r \cos\psi + \tau_{r\psi} \sin\psi] r d\psi \tag{3.1}$$

(b) *Resisting moment per unit length* due to vertical shear stress along the shaft:

$$M_h = \int_0^{2\pi} \tau_{rz} (B/2)^2 \cos\psi d\psi \tag{3.2}$$

(c) *Lateral base resistance* due to horizontal shear stress:

$$P_b = \int_0^{\frac{B}{2}} \int_0^{2\pi} (-\tau_{rz} \cos\psi + \tau_{\psi z} \sin\psi) r d\psi dr \tag{3.3}$$

(d) *Base resisting moment* due to normal stresses:

$$M_b = \int_0^{\frac{B}{2}} \int_0^{2\pi} (\sigma_z \cos\psi) r^2 d\psi dr \tag{3.4}$$

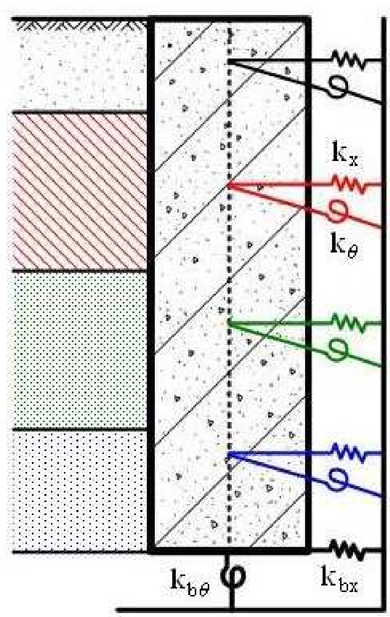


**Figure 3.2** The proposed four spring model

In order to capture these four mechanisms of resistance and therefore simulate the response of pier foundations to lateral loads given the target degree of accuracy, a four spring model is being here proposed. The four springs used in the model (schematically shown in **Figure 3.2**) are:

(a) $k_x$: Lateral translational springs used to characterize lateral force-displacement response of soil;

(b) $k_\theta$: Rotational springs used to characterize the moment developed at the centerline of pier due to vertical shear stress acting at the perimeter of pier, induced by pier rotation;

(c) $k_{bx}$: Base translational spring used to characterize horizontal shear force-base displacement response; and

(d) $k_{b\theta}$: Base rotational spring used to characterize moment developed due to normal stress acting at the base of pier, induced by base rotation.

The model is based on the assumption that the response of each soil layer is decoupled from the overlying and underlying ones, namely on the simplification of shear beam deformation of the soil column. As a result, in absence of coupling between adjacent soil resistance mechanisms, the total response can be obtained through integration of the total resistance offered by the individual springs for each layer. This assumption is not true in regions very close to the interface of two layers but for thick layers, as the distance from the interface increases, the coupling effect diminishes very rapidly and relative contribution of the coupling to total response becomes very small. Thus for thick layers, these effects can be safely neglected.

### 3.2 Formulation of stiffness matrix

Directly stemming from the fact that the elasticity modulus of concrete (30 GPa) or steel (250 GPa) is significantly higher than that of soil (2-5 MPa), the pier foundations investigated in this study, namely foundation elements of intermediate depth-to-diameter ratio (D/B), are here assumed to respond as a rigid bodies without significant loss of accuracy of the solution, As a result, application of a lateral force (V) and an overturning moment (M) at the top will result in a net translation and a rotation of the pier as shown in **Figure 3.3**. Based on the aforementioned assumption, the consequent response of the foundation is adequately described in terms of the displacement at the top ($u_t$), and the rotation angle of the rigid pier (θ).

Given these quantities, the horizontal displacement at any point is given by

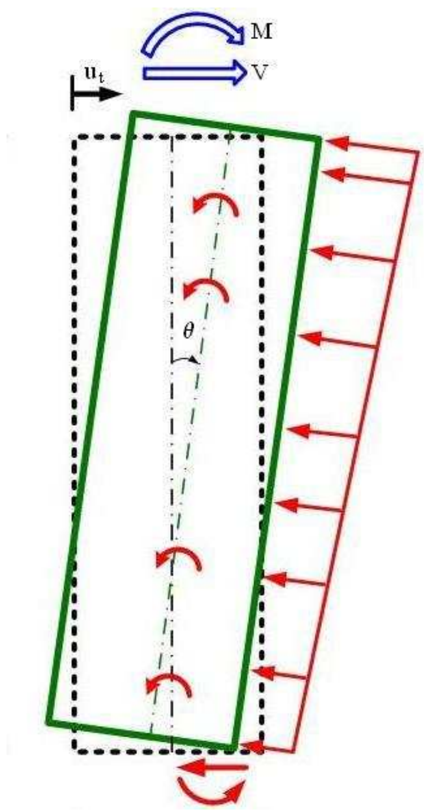


**Figure 3.3** Response of pier upon application of lateral load and overturning moment

$$u(z) = u_t - \theta z \tag{3.5}$$

Applying equilibrium of forces in horizontal direction we have:

$$V = \int_0^D k_x u(z) dz + k_{bx} u(D)$$

$$= \int_0^D k_x (u_t - \theta z) dz + k_{bx} (u_t - \theta D) \ = k_x (u_t D - \theta \frac{D^2}{2}) dz + k_{bx} (u_t - \theta D)$$

Or $$V = u_t (k_x D + k_{bx}) + \theta (-k_x \frac{D^2}{2} - k_{bx} D) \tag{3.6}$$

Successively, the moment equilibrium requirement evaluated at the top of pier results in:

$$M = \int_0^D k_x u(z) z dz + k_{bx} u(D).D + \int_0^D k_\theta \theta dz + k_{b\theta} \theta$$

$$= -\int_0^D k_x (u_t - \theta z) z dz - k_{bx} (u_t - \theta D).D + \int_0^D k_\theta \theta dz + k_{b\theta} \theta$$

$$= -k_x (u_t \frac{D^2}{2} - \theta \frac{D^3}{3}) - k_{bx} (u_t D - \theta D^2) + k_\theta \theta D + k_{b\theta} \theta$$

Or $$M = u_t (-k_x \frac{D^2}{2} - k_{bx} D) + \theta (k_x \frac{D^3}{3} + k_{bx} D^2 + k_\theta D + k_{b\theta}) \tag{3.7}$$

Equations (3.6) and (3.7) are next written in a matrix form as:

$$\begin{bmatrix} V \\ M \end{bmatrix} = \begin{bmatrix} K_{xx} & K_{xr} \\ K_{rx} & K_{rr} \end{bmatrix} \begin{bmatrix} u_t \\ \theta \end{bmatrix} \tag{3.8}$$

where the left-hand side of the equation represents the forcing function (*F*) applied at the top of the foundation, and the right-hand side corresponds to the product of the so-called stiffness matrix (*K*) of the soil-foundation system as interpreted from the foundation top to the response vector (*U*), namely the displacement and rotation of the caisson, i.e. $F = KU$ .

In equation (3.7.) the individual components of the stiffness matrix correspond to the following expressions:

$$K_{xx} = k_x D + k_{bx} \tag{3.9}$$

$$K_{xr} = k_{rx} = -(k_x \tfrac{D^2}{2} + k_{bx} D) \tag{3.10}$$

$$K_{rr} = (k_x \tfrac{D^3}{3} + k_{bx} D^2 + k_\theta D + k_{b\theta}) \tag{3.11}$$

As can be readily observed from the expressions above, the assumption of a rigid caisson results in a symmetric stiffness matrix for the overall foundation system.

### 3.3 Non-dimensional analysis - Parametric investigation

For parametric variation studies and for the purpose of generalization, all the terms are normalized with respect to the Young's modulus of soil (E) and the diameter of pier (B), namely the stiffness and geometry characteristics of the surrounding soil and foundation element respectively. In a non-dimensional form, the equations are given as follows:

$$\begin{bmatrix} \frac{V}{EB^2} \\ \frac{M}{EB^3} \end{bmatrix} = \begin{bmatrix} \frac{K_{xx}}{EB} & \frac{K_{xr}}{EB^2} \\ \frac{K_{rx}}{EB^2} & \frac{K_{rr}}{EB^3} \end{bmatrix} \begin{bmatrix} \frac{u_t}{B} \\ \theta \end{bmatrix} \tag{3.12}$$

where:

$$\frac{K_{xx}}{EB} = \frac{k_x}{E}\left(\frac{D}{B}\right) + \frac{k_{bx}}{EB} \tag{3.13}$$

$$\frac{K_{xr}}{EB^2} = -\left[\frac{1}{2}\frac{k_x}{E}\left(\frac{D}{B}\right)^2 + \frac{k_{bx}}{EB}\left(\frac{D}{B}\right)\right] \tag{3.14}$$

$$\frac{K_{rr}}{EB^3} = \left[\frac{1}{3}\frac{k_x}{E}\left(\frac{D}{B}\right)^3 + \frac{k_{bx}}{EB}\left(\frac{D}{B}\right)^2 + \frac{k_\theta}{EB^2}\left(\frac{D}{B}\right) + \frac{k_{b\theta}}{EB^3}\right] \tag{3.15}$$

These expressions, namely the static resistance of the soil-foundation system, will be used in the ensuing to describe the response of the foundation system for a wide variety of loading conditions, namely forced static loading and vibrations at the top, as well as the kinematic interaction of the foundation to incident seismic motion.

# CHAPTER 4

# NUMERICAL MODELING

## 4.1 Finite element software packages

Three-dimensional finite element simulations have been conducted in this study for the evaluation of the coefficients of subgrade reaction (springs) and the calibration of the proposed analytical model. The simulations are performed using the FEM software package DYNAFLOW (Prevost, 1983) and verified, for the case of static loading- using the FEM software package ABAQUS (Hibbitt, Karlsson, Sorensen, 1995). A direct Crout column solver has been used instead of an iterative one to achieve greater stability and minimize any approximation errors, which would in turn affect the accuracy of the analytical approximations developed on the basis of the numerical simulations. The Crout column solver uses Crout's method of matrix decomposition to decompose a matrix into a lower triangular matrix (L), an upper triangular matrix (U) and a permutation matrix (P) which is then used for inversion of matrices to find an exact solution to linear equations.

## 4.2 Mesh type and element properties

Taking advantage of the symmetry of the problem, only half of the numerical domain is here simulated, thus saving considerable computational effort. Both the soil formation and pier are simulated using 3D continuum soil elements (8 node brick elements). Both soil and pier element material models are here considered linear elastic, while perfect bonding is assumed at the interface, i.e., no separation even under tensile stress. This assumption is equivalent to that of a cylindrical foundation 'welded' in soil, as described by Elsabee et al. (1977). The far field, namely the truncated boundaries of the numerical domain, are placed at a distance equal to 5 times the diameter of the pier (B) at both sides and from the base (unless specified otherwise) to simulate the semi-infinite domain.

For the purpose of this study, two different kinds of meshes were used, hereby referred as Model A and Model B.

(a) Model A: In this model, the far field is cylindrical in shape. The mesh is finer in regions close to the pier to accurately capture the response but its coarseness (element size) increases in proportion to the distance from pier. The thickness (z-direction) of all elements is the same and equal to 0.25 B. The length to width ratio is kept constant as the element size increases. The ratio of maximum-to-minimum dimension, referred to as the foundation aspect ratio, is always kept less than 3 to avoid any distortion effects. The mesh is shown in **Figure 4.1**.

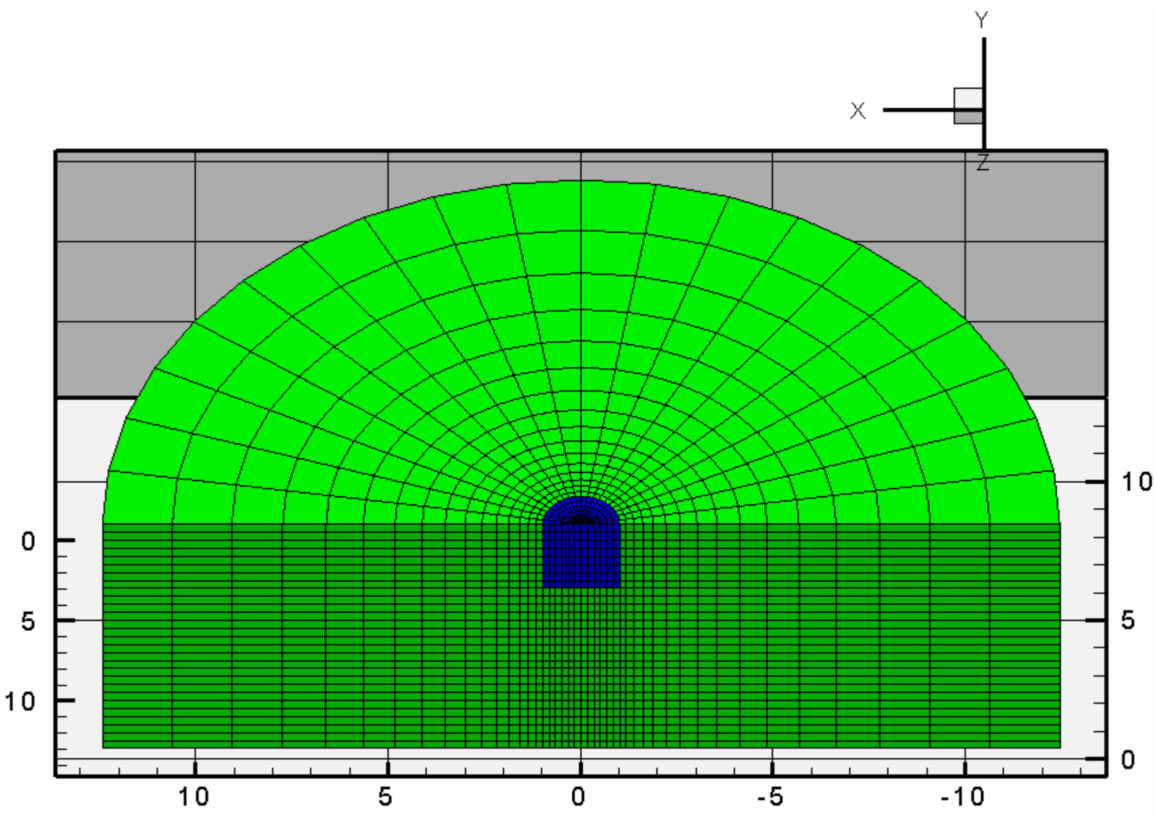


**Figure 4.1** Model A with a cylindrical far-field

(b) Model B: The far field is rectangular in shape. The mesh coarseness is almost of the same order throughout the model. The elements are mostly cubical in shape with dimension 0.25 B. There is a gradual transformation from cylindrical to rectangular shape as we move from pier to far field. The mesh is shown in **Figure 4.2.**

The element size of 0.25 B is determined by maximum capacity of direct solver. For finer meshes the number of elements becomes too large to be handled by a direct solver.

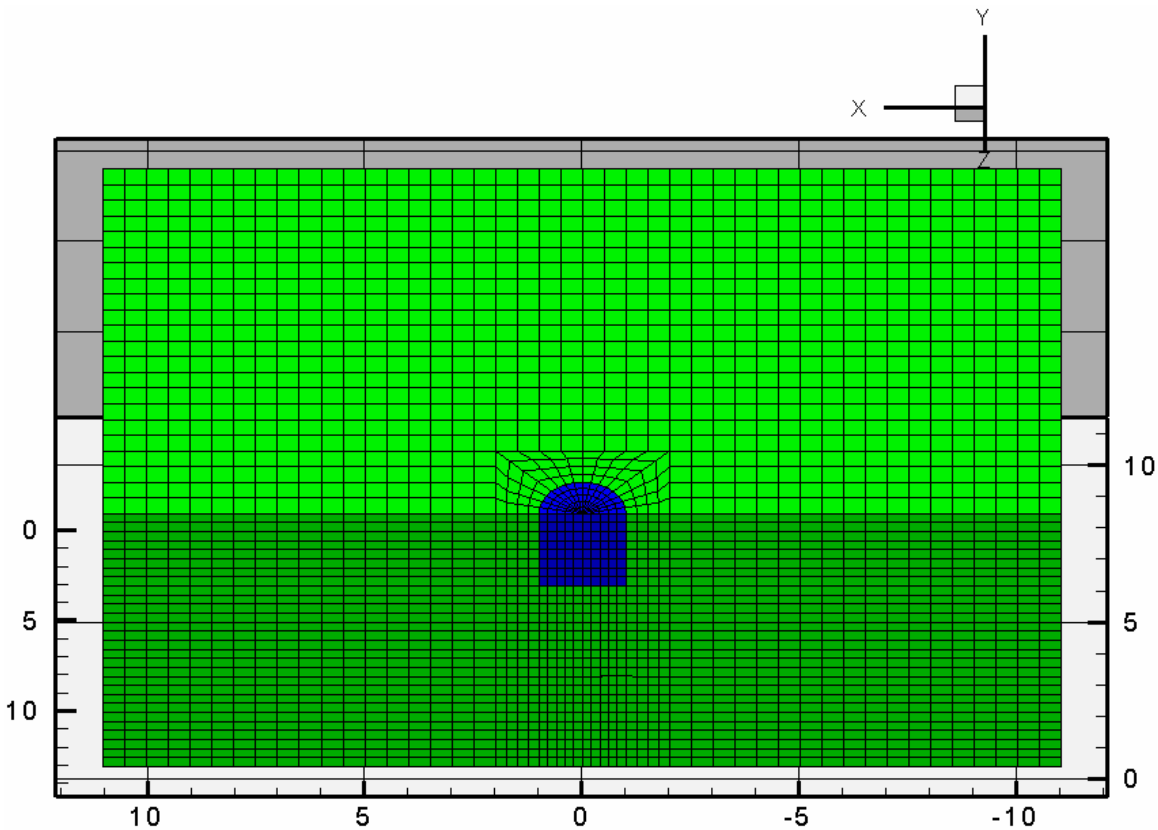


**Figure 4.2** Model B with rectangular far-field

### 4.3 Absorbing boundary layers

The infinite domain represented by finite element models needs to be truncated at some finite boundary. Nonetheless, for dynamic analysis involving wave propagation, the usual finite boundary of the finite element model will cause the elastic waves to be reflected and superimposed to the incident waves. The effect is much more pronounced in absence of damping in the system, as is the case with most of the simulations in this research.

Therefore, the boundary of the numerical model needs to radiate almost entirely the outgoing waves (no spurious reflections) and at the same time to allow for the application of far field motions as the ones imposed by incident seismic waves. In addition, optimization of the computational efficiency requires the boundary to be as close to the finite structure as possible. A simple solution to the problem is to impose finite damping to the material, and prescribe the boundary at a great distance from the finite structure so that the boundary does not influence the results. Inasmuch -however- as this method may be feasible, the increased required numerical model renders the approach computationally inefficient.

For 2D simulations, this can be achieved by using viscous damping elements at the boundary. Note that for wave propagation in unbounded media, the stress is evaluated as:

$$\sigma_i = \frac{\dot{u}_i}{\rho V}$$

where $\sigma_i$ : stress at a point (node)  $\dot{u}_i$ : velocity at the point (node)

$\rho$ : Density of material  $V$ : Wave velocity

Therefore, by using dashpots with coefficients $\rho v_p$ along the direction of propagation of wave and $\rho v_s$ along the other two perpendicular directions, we can successfully implement an approximate absorbing boundary condition.

Nonetheless, this formulation fails to result in successful absorption of the outgoing energy in the following cases:

(a) High angle of incidence (usually >20 degrees)

(b) More than one type of wave reaching the boundary.

In the course of this study, it was observed that surface waves are generated from the pier-soil interaction along with body waves, and the resulting wave field has very high angle of incidence at many locations. As a result, this boundary could not be implemented.

Another option is to use infinite elements at the boundary. Infinite elements are elements with special shape functions that decay for large distances such as $e^{-x}$ or $\frac{1}{x}$.

However, formulation of these elements requires some knowledge of the solution, so that the shape functions are close to the actual solution of the problem. Also, the boundary conditions at infinity have to be known approximately (a zero displacement or zero stress is typically used). These elements can thus be used in conjunction with finite elements in boundary value problems defined in unbounded domains or problems where the region of interest is small in size compared to the surrounding medium. Since, these elements simulate the infinite domain; they provide residual far-field stiffness for static problems and 'quiet' boundaries for dynamic problems. An overview for infinite elements is given by Bettes and Bettes (1984).

For dynamic case, the transmission of energy outside the finite element mesh without trapping or reflecting it, is optimized by making the boundary between the finite and infinite elements as close as possible to being orthogonal to the direction from which the waves will impinge on this boundary. "Close to a free surface, where Rayleigh waves may be important, or close to a material interface, where Love waves may be important, the infinite elements are most effective if they are orthogonal to the surface" (ABAQUS User's Manual, 1992). Thus, for higher angles of incidence, even the infinite elements are not able to absorb the waves completely. Simulations were performed using ABAQUS with infinite elements but the results obtained were not satisfactory.

Thus a new type of boundary is used, hereby referred to as *sponge boundary*. The reflection of outgoing waves back into the region of interest can be avoided by enclosing the region in a sponge layer having high damping coefficients. The mechanical impedance of the sponge layer is kept almost the same as that of soil to avoid any material contrast and hence minimize the generation of reflected waves. The damping is introduced by means of Rayleigh damping and is gradually increased with distance to avoid any spurious reflections due to sudden change in impedance.

For Rayleigh damping, also referred to as Modal damping, the damping matrix is assumed to be proportional to the mass and stiffness matrix as

$$C = \alpha M + \beta K \tag{4.1}$$

The modal damping ratio is then calculated as:

$$D' = \frac{1}{2}(\alpha\omega + \frac{\beta}{\omega}) \tag{4.2}$$

where α is mass proportional damping and β is stiffness proportional damping coefficients.

Assuming the propagation of a sinusoidal wave of the following form:

$$u(x,t) = e^{i\omega(t-\frac{x}{v})} \tag{4.3}$$

The use of the viscoelastic correspondence principle (Christensen, 1971) results in the following expressions:

$$E^* = E(1 + i2D') \tag{4.4}$$

$$V^* = \frac{V}{\sqrt{1+4D'^2}}\left[\frac{1+\sqrt{1+4D'^2}}{2} + iD'\right] \tag{4.5}$$

$$\frac{1}{V^*} = \frac{1}{V}\left[1 - i\frac{2D'}{1+\sqrt{1+4D'^2}}\right] = \frac{1}{V}\left[1 - i\alpha'\right] \tag{4.6}$$

$$\text{where } \alpha' = \frac{2D'}{1+\sqrt{1+4D'^2}} \tag{4.7}$$

$$\text{Thus, } u(x,t) = e^{i\omega(t-\frac{x}{v^*})} = e^{-\frac{\omega x}{v}\alpha'} e^{i\omega(t-\frac{x}{v})} = e^{-\frac{\omega x}{v}\alpha'} u_o(x,t) = A(\omega,x)u_o(x,t) \tag{4.8}$$

Given the limited maximum size of model due to computational restrictions and ensuring that the sponge layer is at sufficient distance from the pier to simulate the far-field conditions with sufficient accuracy, the thickness of sponge layer is chosen to be 2.0 B.

The coefficients $\alpha$ and $\beta$ are chosen using the following two criteria:

(a) The damping ratio D' should be relatively uniform over the frequency range being considered, which determines the $\alpha / \beta$ ratio.

(b) The amplitude of the damped waves should be less than 5% of the undamped amplitude, which determines the actual magnitude of $\alpha$ and $\beta$.

Using the first criteria a ratio of $\alpha / \beta$ = 400 is selected. The variation D' with frequency for the range being used in simulations is shown in **Figure 4.3.** Using the second criteria, a maximum value of $\alpha$ =20 and $\beta$=0.05 is selected. The damping in the model is applied progressively in 4 to 5 layers as given in **Table 4.1**.

| Layer no. | 1 | 2 | 3 | 4 |
|---|---|---|---|---|
| $\alpha$ | 5 | 10 | 15 | 20 |
| $\beta$ | 0.0125 | 0.0250 | 0.0375 | 0.05 |

**Table 4.1** Mass and stiffness dependent damping coefficient used for 'sponge boundaries'

The variation of amplitude reduction function A with frequency is shown in **Figure 4.4**.

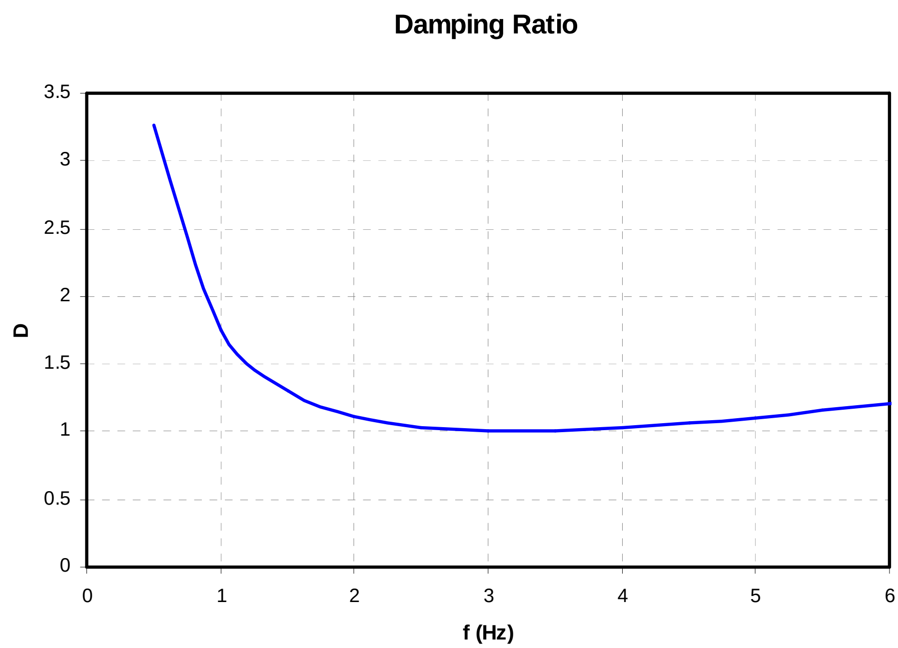


**Figure 4.3** Variation of Rayleigh damping ratio with frequency

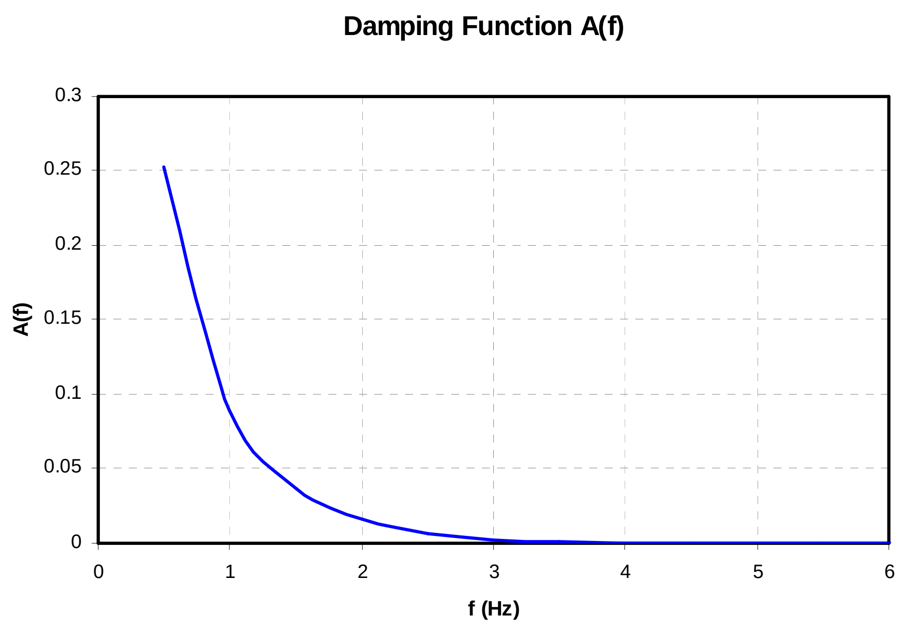


**Figure 4.4** Amplitude reduction as a function of frequency

**Figure 4.5** shows the model used with simulated zone of interest and sponge layers outside the far-field boundary.

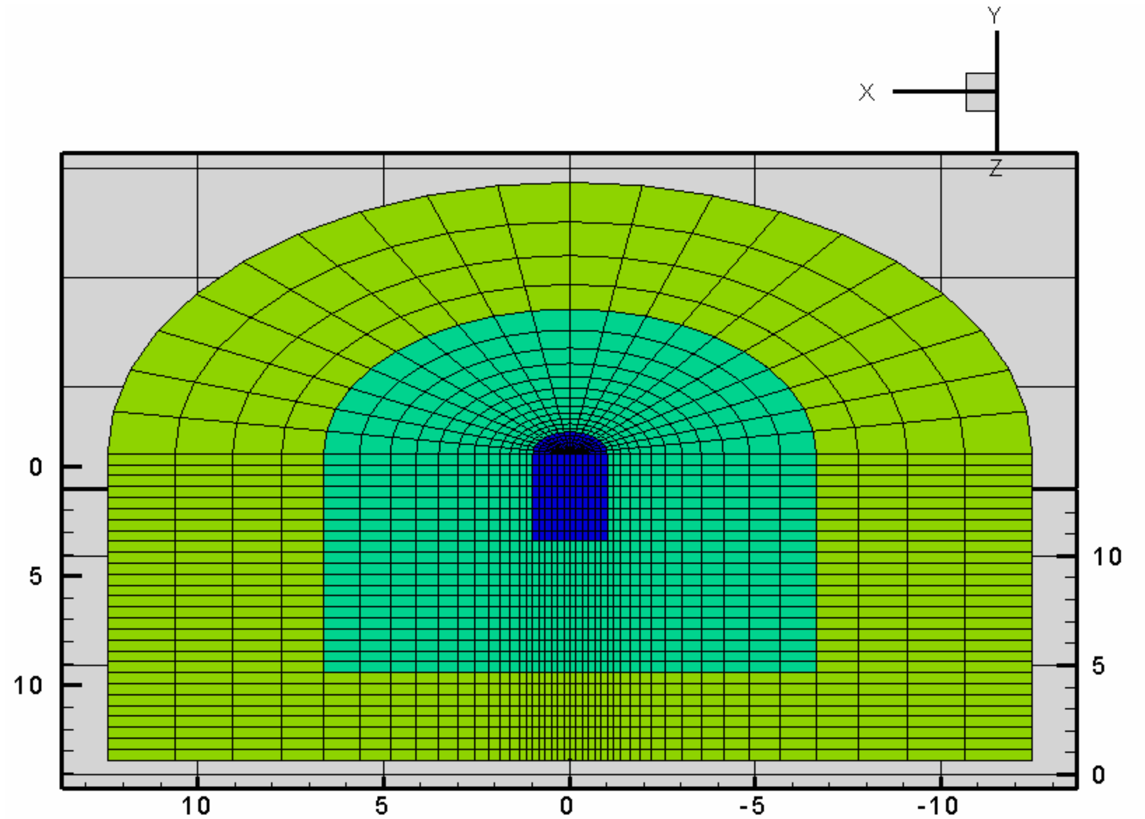


**Figure 4.5** The model depicting the simulated region of interest and sponge layers outside

### 4.4 Maximum frequency and time step

The numerically accurate representation of wave propagation problems corresponding to numerical attenuation because of undersampling requires at least 6-7 elements per wavelength. Based on this requirement, $\lambda / 6 \geq \kappa B$ where $\kappa$ = ratio of size of largest element to B. On the other hand the frequency of foundation vibration $a_o$ may be expressed in dimensionless form as $a_o = \omega B / V_s$.

As a result, the maximum frequency that can be simulated with sufficient accuracy is described by the following expression:

$$a_o = \frac{\omega B}{v_s} = \frac{2\pi f B}{v_s} = \frac{2\pi B}{\lambda} \leq \frac{2\pi}{6\kappa} \tag{4.8}$$

For the case of Model A, the ratio of element size to foundation width $\kappa = 0.67$, and therefore $a_{\max} \approx 3.5$. Similarly, for Model B, $\kappa = 0.50$ and therefore $a_{\max} \approx 4.0$.

Based on the aforementioned highest accurately represented frequency, the minimum time step is consequently given by the following expression:

$$t = \frac{\kappa B}{v_s} = \frac{\kappa B}{f\lambda} \leq \frac{1}{6f} = \frac{T_{\min}}{6}$$

where f = frequency of excitation

In the simulations presented in the ensuing of this study, a time step of $\frac{T_{\min}}{20}$ to $\frac{T_{\min}}{40}$ has been employed.

### 4.5 Advantages and limitations of Model A and Model B

As mentioned above, model A is an adaptive mesh (element size increases with distance from the pier), a fact which has the following implications:

(a) It consists of lesser number of elements thus considerably reducing the amount of computational time;

(b) the element size increases with distance from pier, which implies that the accurate representation of wave propagation restricts the far field to a maximum distance from the foundation center, namely the distance where the element size equals the maximum element size permitted by frequency consideration (2.5B in this case); and

(c) Beyond the far field, numerical attenuation is observed due to very large element size. Nonetheless, the attenuation only adds to the effective damping already accounted for in the sponge layers, and hence improves –in this case- the performance of the far-field truncated conditions.

Based on the aforementioned observations, Model A is here used in all dynamic simulations, while Model B has been used in the static case, and in particular for comparison purposes only.

### 4.6 Simulation of the far-field seismic motion

In order to evaluate the kinematic response of the foundation, namely the response of the element to the incidence of seismic waves, the input motion is prescribed directly to the region of interest in form of effective forcing functions at the base and lateral boundaries of the numerical domain bounded by sponge boundaries. The forcing functions for lateral boundaries are evaluated as the 1D response of the corresponding soil columns. The difference between the 1D motion and 2D response evaluated at the far-field is actually the scattered energy of the system, which propagates outwards from the irregularity and is absorbed by the artificial boundaries. The evaluation of consistent boundary conditions prescribed around the numerical domain of interest is based on the Substructure Theorem (Rosset, 1975). According to this theorem, the free-field vibration problem can be decomposed into substructures (the far-field and the soil-structure configuration, referred to as near-field) as shown schematically in **Figure 4.6**.

Since the excitation is exactly the same for the far-field and the interaction problem, differences in the interface displacements ($\Delta U = Ub - U^*b$) are solely attributed to differences in the interface stresses ($\Delta S = Sb - S^*b$). If the far-field is now subjected to forces $\Delta S$, in the absence of seismic excitation, displacements $\Delta U$ will be produced, such that $\Delta S = X\ \Delta U$, where X is the frequency-dependent dynamic impedance matrix of the far-field, i.e. the stiffness of the far-field as seen by the interface. Substituting the forces and displacement differences at the boundaries, we obtain:

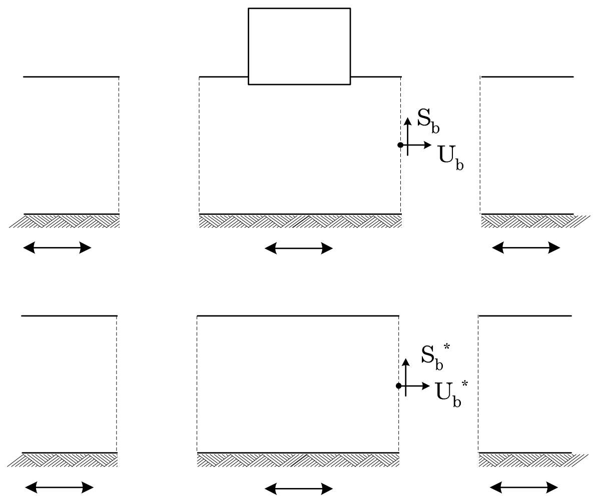


**Figure 4.6** Schematic representation of the Substructure Theorem for soil-structure interaction problems (the interaction problem is shown on the top, and the free-field problem on the bottom figure)

$$-S_b = -XU_b + XU_b^* - S_b^* \qquad (4.9)$$

Since the domain is infinite, the equivalent spring stiffness implied by X is zero. The stresses $XU_b^* - S_b^*$ correspond to the far-field motion and are applied to the lateral boundaries. For the wave-propagation problem analyzed herein, the far-field motion is defined as the response of a one-dimensional soil column, subjected to the input motion prescribed at the base of the two-dimensional configuration. Successively, the fictitious forces prescribed at the lateral boundaries of the three-dimensional model are determined as follows for the case of SH-wave incidence:

(a) $S_b^*$ corresponds to the vertical reaction preventing the vertical motion at the far field boundary; and

(b) $XU_b^* = V_s U_b^{'}$ corresponds to the product of the calculated far field (1D) response and impedance, where $U_b^{'}$ the velocity time history at the 1D column nodes, and $V_s$ the S-wave velocity at the corresponding location.

For the purpose of this study, the forces are applied in form of surface loads (tractions) both at the base and the lateral boundaries in the 3D model. It should be noted that the substructure theorem is based on the principle of superposition, and is therefore applicable to linear problems as well as approximately applicable to moderately inelastic systems.

# CHAPTER 5

# STATIC TRANSVERSE LOADING AT THE TOP OF CAISSON

This chapter discusses the methodology used to calculate the stiffness matrix and springs and its limitations. The effect of distance of far field boundaries is investigated. A parametric study for representative pier to soil stiffness ratios in the field is performed to verify the rigid behavior of the pier. The results are presented for static simulations and are also compared with other available analytical formulations. The springs obtained are then approximated using simple expressions. Various other parametric studies are also presented such as sensitivity to Poisson ratio and effect of eccentricity in loading.

## 5.1 Calculation of stiffness matrix and individual springs

Consider the matrix formulation of the equation of equilibrium of externally applied forces and soil reactions evaluated in Equation 3.8. This expression can also be written as:

$$\begin{bmatrix} u_t \\ \theta \end{bmatrix} = \begin{bmatrix} K_{xx} & K_{xr} \\ K_{rx} & K_{rr} \end{bmatrix}^{-1} \begin{bmatrix} V \\ M \end{bmatrix} = \begin{bmatrix} u_V & u_M \\ \theta_V & \theta_M \end{bmatrix} \begin{bmatrix} V \\ M \end{bmatrix} \tag{5.1}$$

In particular for the case of unit externally applied lateral force and moment at the top of the caisson:

$$\begin{bmatrix} K_{xx} & K_{xr} \\ K_{rx} & K_{rr} \end{bmatrix} = \begin{bmatrix} u_V & u_M \\ \theta_V & \theta_M \end{bmatrix}^{-1} \tag{5.2}$$

where the displacement components on the right-hand side of the equation are:

$u_V$ : displacement at top upon the application of a unit force

$\theta_V$ : rotation of the rigid body upon the application of a unit force

$u_M$ : displacement at top upon the application of a unit moment

$\theta_M$ : rotation upon the application of a unit moment

As a result, the stiffness matrix can be evaluated by simply computing the displacements at top and rotations of pier due to the application of a unit lateral force and a unit overturning moment separately and inverting the matrix in Equation 5.2. This method is typically referred to as the *flexibility approach* and is extensively applied in the field of structural mechanics.

The individual lateral springs along the length and at the base of the pier, namely $k_x$ and $k_{bx}$ correspondingly, are then back calculated by equating the overall lateral and coupled stiffness of the pier shown in equations (3.9) and (3.10) to the numerically evaluated stiffness as:

$$k_x = 2\left(\frac{K_{xx}D + K_{xr}}{D^2}\right) \tag{5.3}$$

$$k_{bx} = -\left(\frac{K_{xx}D + 2K_{xr}}{D}\right) \tag{5.4}$$

Successively, the overall rotational stiffness of the foundation as interpreted from the top, described in Equation 3.11, can be written as:

$$K_{rr} - (k_x \tfrac{D^3}{3} + k_{bx}D^2) = k_\theta D + k_{b\theta} \tag{5.5}$$

In order to evaluate $k_\theta$ and $k_{b\theta}$, we evaluate the equality described by Equation 5.5 for two different but close values of D. The inherent assumption of this approach is that the variation of these two springs with (D/B) is small.

## 5.2 Effect of far-field boundaries

Three-dimensional finite element simulations are here conducted using the computer code DYNAFLOW for both Model A and Model B with the far field conditions imposed at distance equal to 5B on both sides and away from the base. The results were compared to static simulations evaluated by means of ABAQUS using infinite elements at the boundary.

The stiffness matrix and springs evaluated by means ABAQUS were initially found to be approximately 20-25% lower than corresponding ones obtained by means of DYNAFLOW. This was attributed to the fact that a distance of 5B on the sides was not sufficient to simulate the semi-infinite domain for lateral loading, and therefore, the variability in far-field representation between the two approaches (infinite elements vs. sponge boundary conditions) results in large deviation between the two finite element numerical model solutions.

Based on that observation, more simulations were conducted in DYNAFLOW where the numerical domain was truncated at a increasing distance from the foundation center; at a distance equal to 10B, values were then found deviate approximately by 5% compared to the corresponding results obtained by means of ABAQUS. Results from this investigation show that a minimum far field distance of 10B on each side should be employed for static simulations, if standard fixities are used at the boundary. The results are however not sensitive to the far-field boundary below the foundation base at distances greater than 5B.

In the ensuing, results from the ABAQUS simulations are being presented, and selected simulations are compared across the two numerical solutions in **table 5.1**.

### 5.3 Validation of rigid body behavior and effect of Ep/E ratio

It has been shown above that based on the assumption of rigid body motion of the pier and consequent absence of flexural bending, the stiffness matrix obtained in Equation (3.10) is symmetric, namely the off-diagonal coupled stiffness terms are equal $K_{xr} = K_{rx}$. **Figure 5.1** depicts the sensitivity of coupled stiffness $K_{xr} = K_{rx}$ , namely the expression:

| D/B ratio | DYNAFLOW (far field distance 5B) | | | ABAQUS (with infinite elements) | | |
|---|---|---|---|---|---|---|
| | $K_{xx}$ | $K_{xr}$ | $K_{rr}$ | $K_{xx}$ | $K_{xr}$ | $K_{rr}$ |
| 0.25 | 1.83 | -0.37 | 0.51 | 1.53 | -0.31 | 0.49 |
| 0.5 | 2.36 | -0.84 | 1.02 | 2.12 | -0.76 | 0.98 |
| 0.75 | 2.85 | -1.43 | 1.83 | 2.52 | -1.28 | 1.74 |
| 1 | 3.32 | -2.15 | 3.00 | 2.91 | -1.90 | 2.83 |
| 1.25 | 3.78 | -2.99 | 4.59 | 3.28 | -2.61 | 4.28 |
| 1.5 | 4.23 | -3.94 | 6.67 | 3.63 | -3.41 | 6.16 |
| 1.75 | 4.68 | -5.02 | 9.28 | 3.98 | -4.30 | 8.50 |
| 2 | 5.13 | -6.21 | 12.49 | 4.33 | -5.28 | 11.35 |
| 2.25 | 5.58 | -7.52 | 16.35 | 4.67 | -6.35 | 14.76 |
| 2.5 | 6.03 | -8.96 | 20.94 | 5.00 | -7.51 | 18.76 |
| 2.75 | 6.49 | -10.52 | 26.31 | 5.34 | -8.75 | 23.42 |
| 3 | 6.94 | -12.21 | 32.52 | 5.67 | -10.09 | 28.76 |
| 3.25 | 7.41 | -14.03 | 39.66 | 6.01 | -11.52 | 34.85 |
| 3.5 | 7.88 | -15.98 | 47.78 | 6.35 | -13.05 | 41.74 |
| 3.75 | 8.35 | -18.07 | 56.97 | 6.69 | -14.67 | 49.48 |
| 4 | 8.84 | -20.31 | 67.31 | 7.03 | -16.39 | 58.12 |
| 4.25 | 9.34 | -22.71 | 78.89 | 7.38 | -18.23 | 67.74 |
| 4.5 | 9.84 | -25.27 | 91.83 | 7.74 | -20.17 | 78.39 |
| 4.75 | 10.37 | -28.01 | 106.22 | 8.10 | -22.24 | 90.17 |
| 5 | 10.90 | -30.94 | 122.20 | 8.47 | -24.43 | 103.13 |
| 5.25 | 11.46 | -34.08 | 139.90 | 8.85 | -26.77 | 117.39 |
| 5.5 | 12.04 | -37.45 | 159.51 | 9.25 | -29.24 | 133.04 |
| 5.75 | 12.65 | -41.07 | 181.22 | 9.65 | -31.89 | 150.21 |
| 6 | 13.28 | -44.96 | 205.22 | 10.08 | -34.70 | 169.00 |
| 6.5 | 14.66 | -53.75 | 261.28 | 10.98 | -40.94 | 212.18 |
| 7 | 16.24 | -64.16 | 330.44 | 11.98 | -48.15 | 264.09 |

**Table 5.1** Comparison between Global stiffness terms obtained using DYNAFLOW (lateral far field boundary 5B away from pier) and ABAQUS (infinite elements in far field)

$$\frac{dK_{xr}}{K_{xr}^{avg}} = 2\frac{(K_{xr} - K_{rx})}{(K_{xr} - K_{rx})} \tag{5.6}$$

as a function of the aspect ratio D/B for soil Poisson ratio ν=0.3 and foundation-soil impedance ratios ($E_p/E$ =$10^4$ and $10^5$ , which are representative for the case of concrete and steel respectively. For D/B ratios larger than 6, the deviation is shown to exceed 0.05 (5%) for $E_p/E = 10^4$. Thus, the assumption of a rigid pier is considered valid only for aspect ratios D/B ≤ 6.

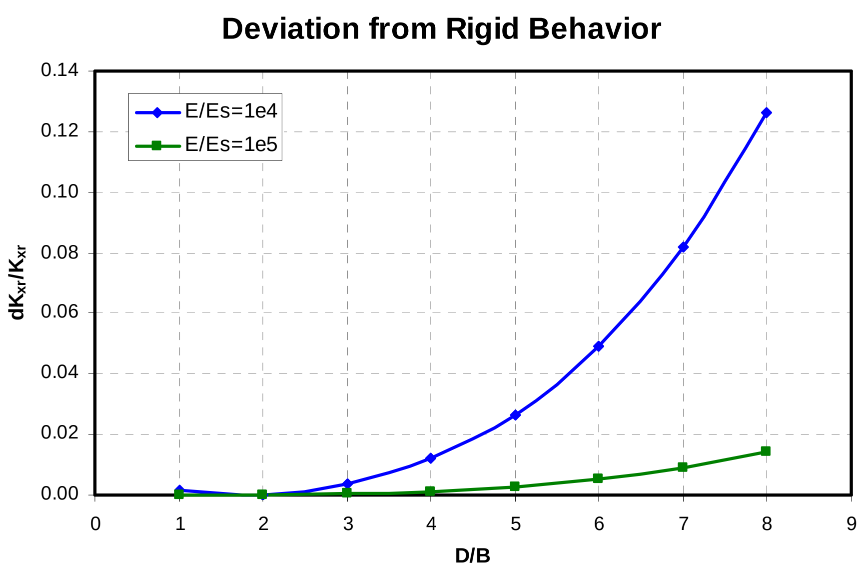


**Figure 5.1** Deviation of pier from rigid behavior for different pile to soil stiffness ratios – coupled stiffness sensitivity as a function of the aspect ratio D/B for two foundation-soil impedance contrasts.

**Figure 5.2a, b** and **c** compare the components of the stiffness matrix for constant $E_p/E$ ratios. As can be readily seen, for D/B > 6 there is significant difference in stiffness terms for both cases. However, below D/B = 6, the stiffness matrix is almost independent of stiffness contrast between the soil and pier.

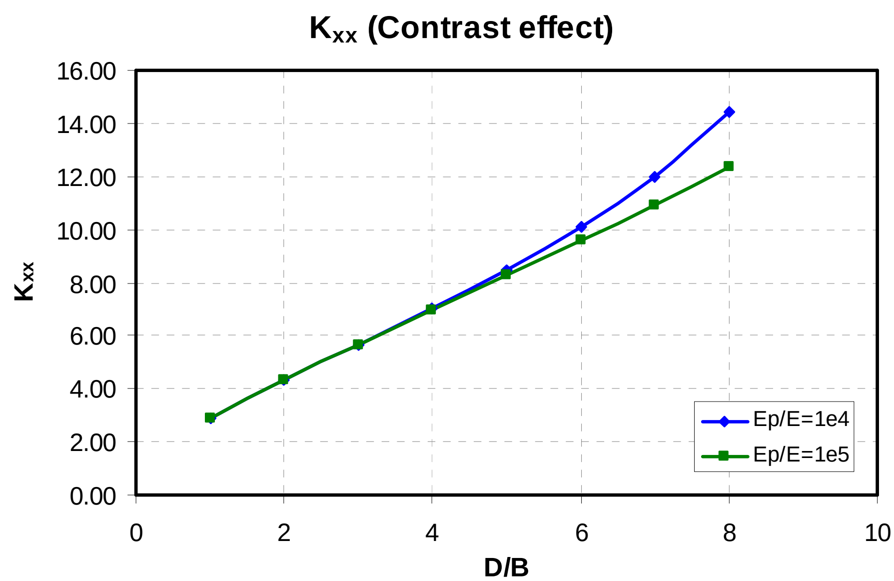


**Figure 5.2a** Variation of lateral stiffness $K_{xx}$ with pier to soil stiffness contrast ($E_p/E$).

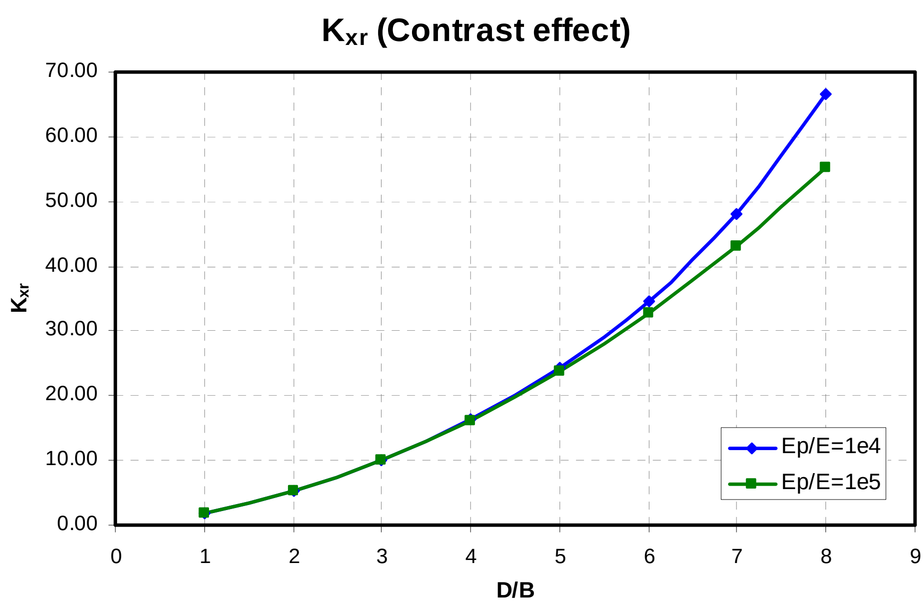


**Figure 5.2b** Variation of coupled stiffness $K_{xr}$ with pier to soil stiffness contrast ($E_p/E$).

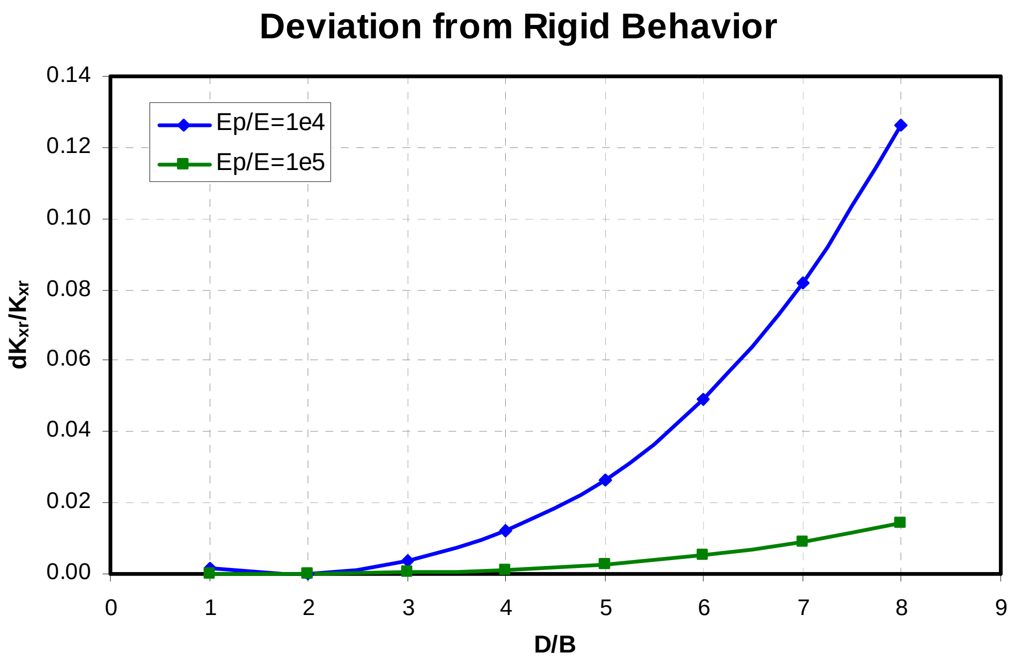


**Figure 5.2c** Variation of rocking stiffness $K_{rr}$ with pier to soil stiffness contrast ($E_p/E$).

### 5.4 Comparison of results to shallow foundation theory

In this part, we shall compare the overall foundation stiffness evaluated by means of finite element simulations to analytical solutions evaluated for shallow foundations, to examine the applicability of the latter for the analysis of intermediate foundation elements such as the caisson foundation investigated here. Multiple analytical solutions and formulations are available in the literature to describe the behavior of embedded foundations subjected to lateral loading. Among others, the formulations against which finite element results obtained in this study are being compared are shown below.

1. Wolf (1997) presents spring-dashpot-mass models for vibrations of rigid cylinder foundations embedded in halfspace as shown below in **Figure 5.4**. The stiffness elements of the model are evaluated as follows:

   $$f_K = 0.25e$$

   $$K_h = \frac{8Gr_o}{2-v}\left(1+\frac{e}{r_o}\right)$$

$$K_r = \frac{8Gr_o^{\,3}}{3(1-\nu)}\left(1+2.3\frac{e}{r_o}+0.58\left(\frac{e}{r_o}\right)^3\right)$$

$$K_{or} = K_r - \frac{Gr_o^{\,3}}{2(2-\nu)}\left(1+\frac{e}{r_o}\right)\left(\frac{e}{r_o}\right)^2$$

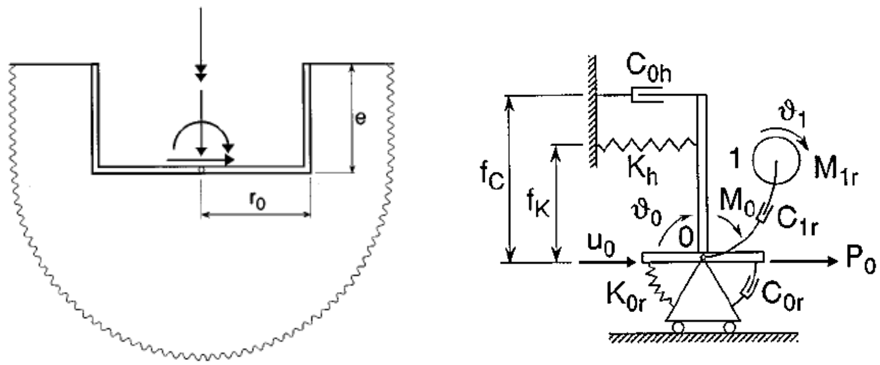


**Figure 5.3a** Cylinder embedded in half space and its equivalent model (Wolf, 1997)

From the above model, the stiffness matrix terms for static loading applied at the top of the foundation are calculated as follows:

$K_{xx} = K_h$

$K_{xr} = K_h f_K$

$K_{rr} = K_{or} + K_h f_K^2$

2. Elsabee et al. (1977) and Kausel (1974) developed formulations for stiffness of rigid embedded cylindrical foundations welded into a homogeneous soil stratum over bedrock as shown in **figure 5.3b**.

   According to these studies, the overall stiffness of the foundation as interpreted from the top of the element is expressed as:

$$K_{xx} = \frac{8GR}{2-\nu}\left(1+\frac{R}{2H}\right)\left(1+\frac{2D}{3R}\right)\left(1+\frac{5D}{4H}\right)$$

$$K_{xr} = 0.4k_{xx}D$$

$$K_{rr} = \frac{8GR^3}{3(1-\nu)}\left(1+\frac{R}{6H}\right)\left(1+\frac{2D}{R}\right)\left(1+\frac{0.7D}{H}\right)$$

These expressions are shown to be valid for D/H < 0.5 and D/R < 2.

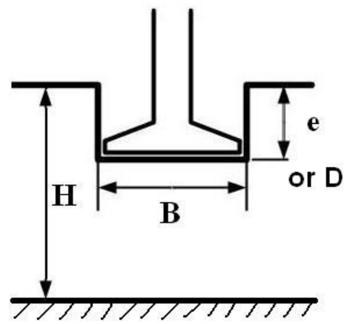


**Figure 5.3b** Rigid embedded cylindrical foundations welded into a homogeneous soil stratum over bedrock

3. Novak et. al (1978) evaluated the dynamic soil reactions for plane strain conditions. Despite the fact that for static loading conditions, the formulation results in zero soil reactions, for quasi-static loading (i.e. low dimensionless frequencies $a_o = 0.1$) and material Poisson's ratio $\nu = 0.3$, they result in the following expressions:

   $$\frac{k_x}{G} \approx 3$$

   $$\frac{k_\theta}{GB^2} \approx 0.75$$

   Assuming that along the length of the caisson, individual cross-sections will respond based on Novak's assumption for plane strain conditions, one needs to also account for the base lateral and rotational reaction of the foundation. For the case of weightless, linear elastic medium as investigated here, a multitude of formulations have been developed in the past for rigid circular foundations on halfspace; among others, the most well known are the expressions by Luco and

Westmann (1971), Velestos and Wei (1971) and Velestos and Verbic (1974), which describe the soil reaction at the base of the footing as:

$$k_{bx} = \frac{8GR}{2-\nu}$$

$$k_{b\theta} = \frac{8GR^3}{3(1-\nu)}$$

Combining the distributed springs approximated by Novak's approach and the base springs approximated by the reaction of surface foundations, the stiffness matrix was evaluated for the analytical model proposed in this study as shown in **figure 5.3c**, and results are compared to the numerical analyses in the ensuing.

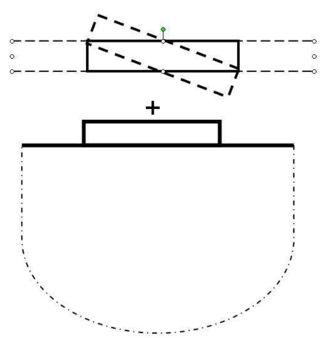


**Figure 5.3c** Combination of springs for Novak plane strain case and Velestos rigid circular footing on half-space

4. Electrical Power Research Institute (EPRI)(1982) also calibrated a four spring model from three dimensional simulations in ABAQUS using a stress based approach for static lateral loading applied at the top of drilled piers for Poisson ratio = 0.3; according to this study, the

$$\frac{k_h B}{E} = 5.18\left(\frac{D}{B}\right)^{-0.525}$$

$$\frac{k_\theta}{EB} = 0.476\left(\frac{D}{B}\right)^{-0.052}$$

$$\frac{k_b B}{E} = 1.64\left(\frac{D}{B}\right)^{-0.139}$$

$$\frac{k_{b\theta}}{EB} = 0.178\left(\frac{D}{B}\right)^{0.426}$$

According to this study, the soil reactions (i.e. springs) along the caisson and at the case are defined in terms of force per unit area, and converting to stress reactions according to the approach proposed here, the expressions become:

$$\frac{k_x}{E} = 5.18\left(\frac{D}{B}\right)^{-0.525}$$

$$\frac{k_\theta}{EB^2} = 0.476\left(\frac{D}{B}\right)^{-0.052}$$

$$\frac{k_{bx}}{EB} = \frac{\pi}{4}1.64\left(\frac{D}{B}\right)^{-0.139}$$

$$\frac{k_{b\theta}}{EB^3} = \frac{\pi}{4}0.178\left(\frac{D}{B}\right)^{0.426}$$

The displacements of pier in x and z direction for lateral loading are shown in **figure 5.4a-b**

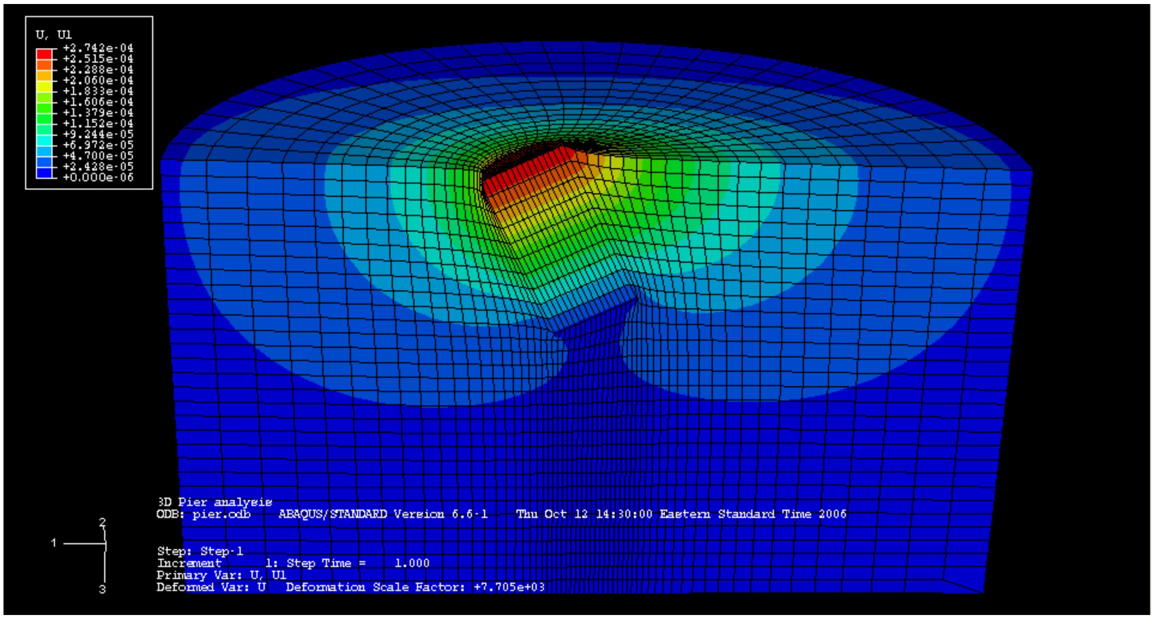


**Figure 5.4a**: Displacement contours in X-direction for lateral loading of pier

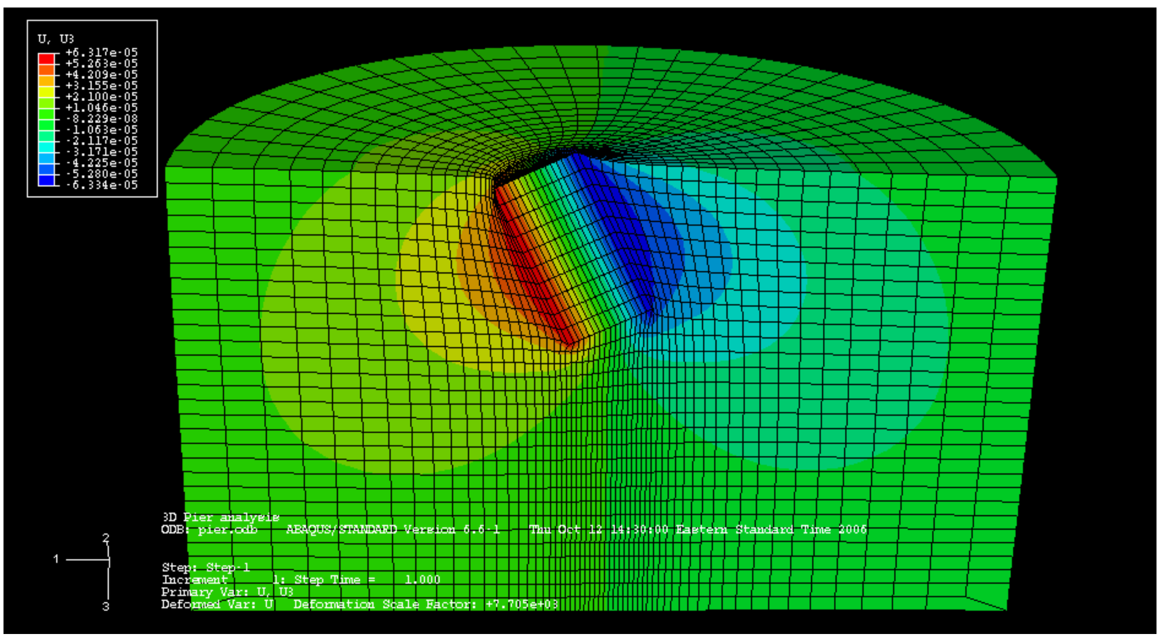


**Figure 5.4b**: Displacement contours in Z-direction for lateral loading of pier

In the ensuing, **Figures5.5a-c** depict the variation of overall foundation stiffness as interpreted from the top as a function of the aspect ratio (D/B), evaluated by means of the spring coefficients developed in this study according to Equation 3.9-3.11 .

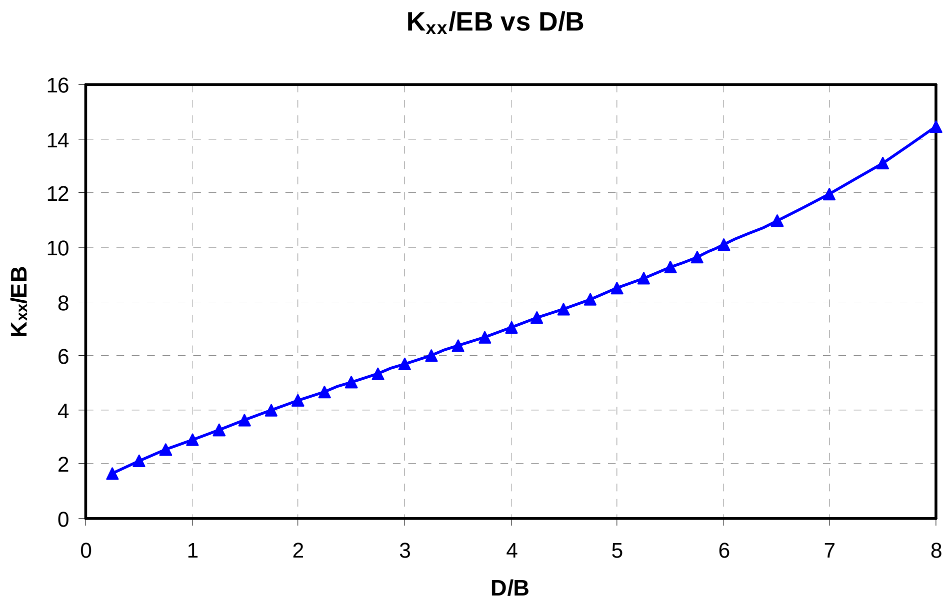


**Figure 5.5a** Variation of $K_{xx}$ with D/B ratio

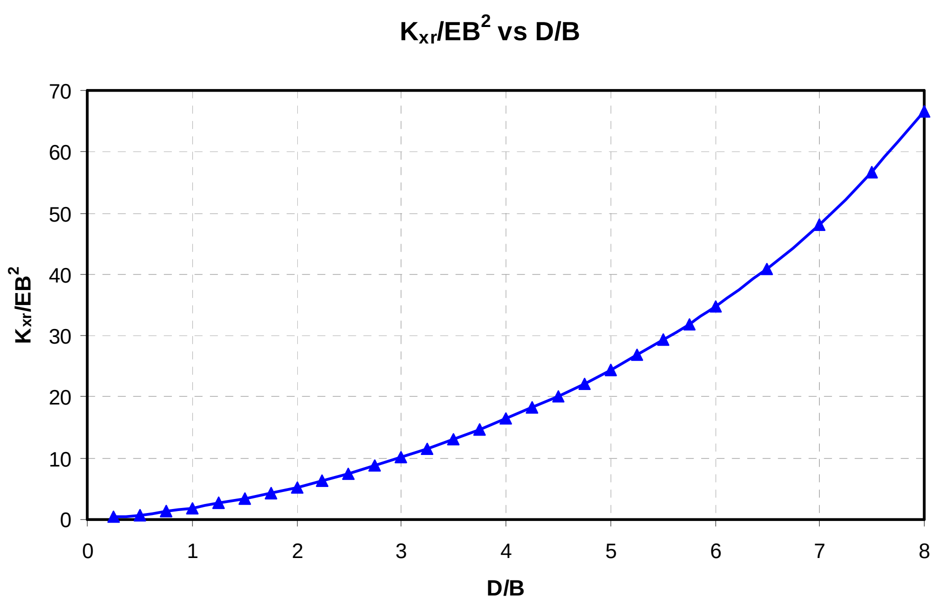


**Figure 5.5b** Variation of $K_{xr}$ with D/B ratio

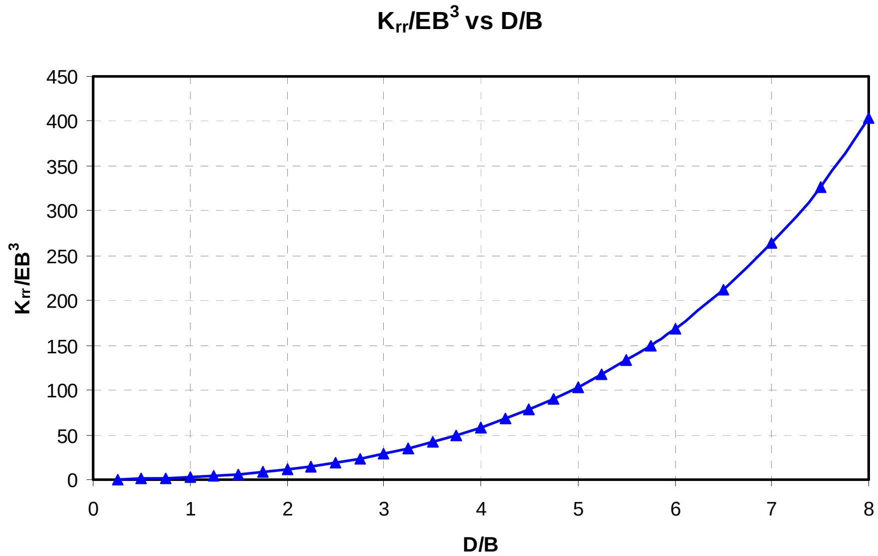


**Figure 5.5c** Variation of $K_{rr}$ with D/B ratio

Results for these components of the overall foundation stiffness matrix are next compared to the aforementioned available shallow foundation formulations and shown in **figure 5.6 (a)-(c).**

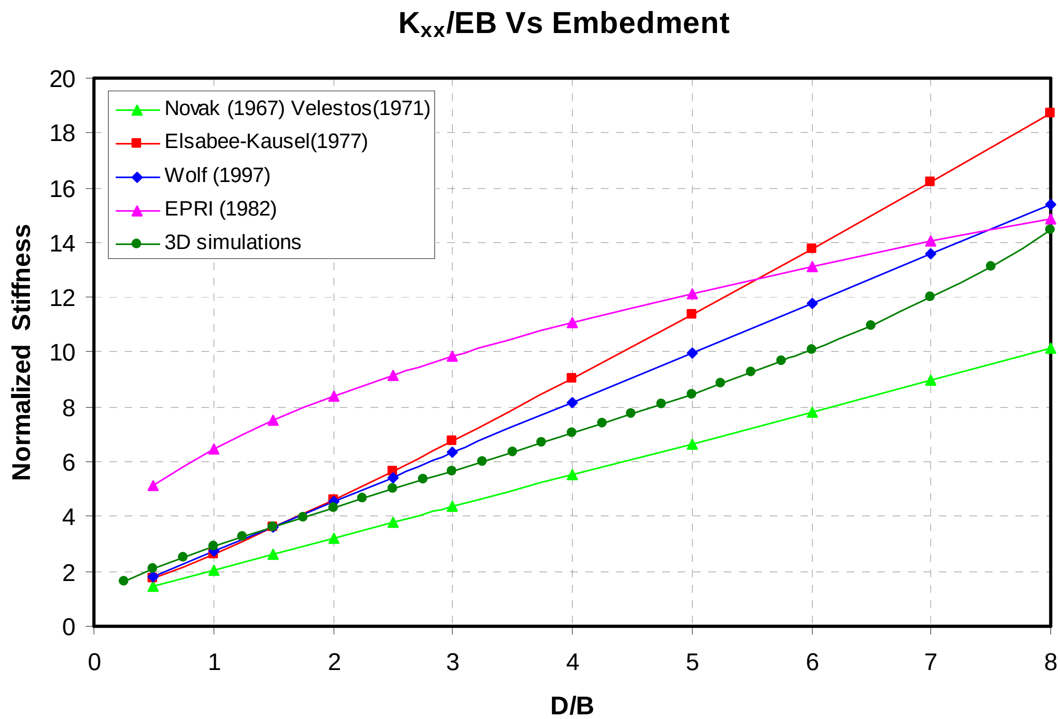


**Figure 5.6(a)** Comparison of $K_{xx}$ with different solutions available

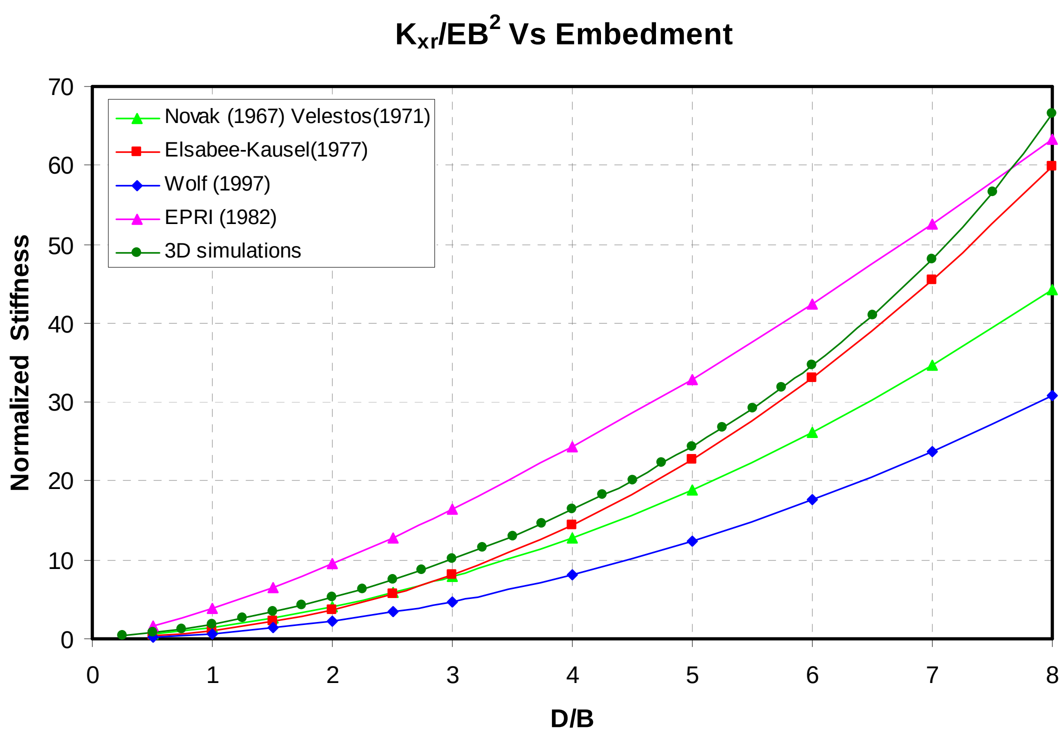


**Figure 5.6(b)** Comparison of $K_{xr}$ with different solutions available

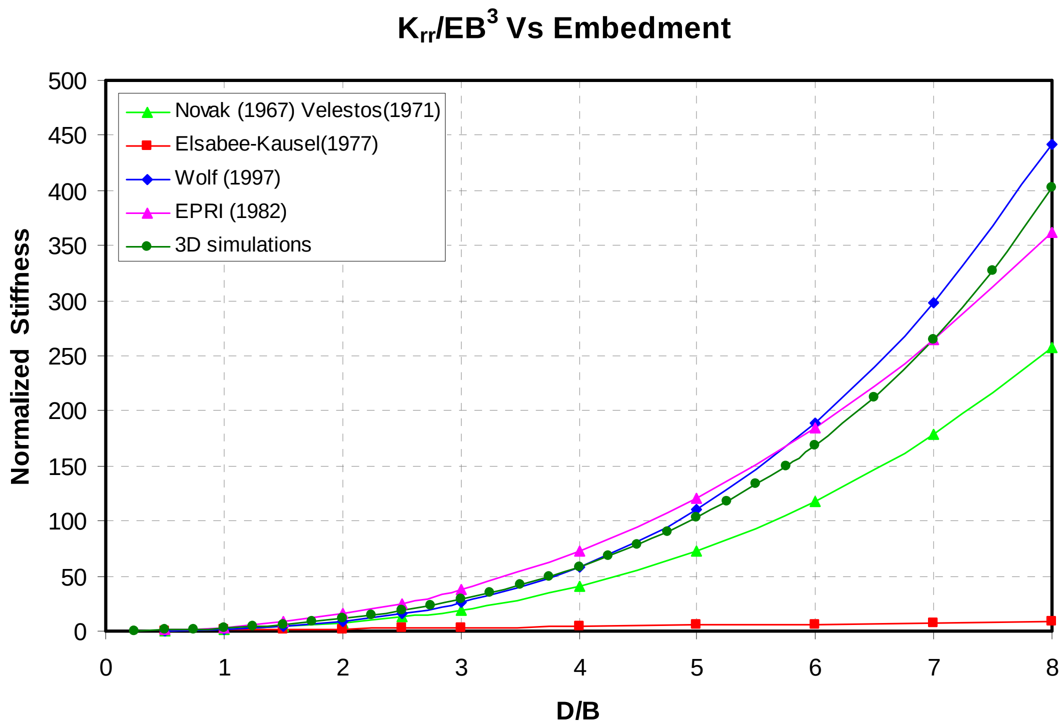


**Figure 5.6(c)** Comparison of $K_{rr}$ with different solutions available

Based on the results compared above, we conclude the following regarding the applicability of shallow foundation theories for the analysis of intermediate rigid foundation elements:

(a) The model proposed by Kausel (1974) and Elsabee (1977) captures the lateral and coupled stiffness very well, but significantly under-predicts the rocking resistance.

(b) The model proposed by Wolf (1997) captures the lateral and rocking stiffness very well, but under-predicts the coupled resistance.

(c) The EPRI (1982) model may be used to simulate the coupled and rocking stiffness components, but over-predicts the lateral resistance.

(d) The stiffness values predicted by springs obtained from combination of formulations by Novak (1978) and Velestos (1971), namely constant spring values independent of the foundation aspect ratio (D/B) is a good approximation to the configuration investigated here and qualitatively captures the overall variation of stiffness as a function of D/B, but quantitatively predicts lower stiffness values than the actual ones obtained.

Based on the aforementioned conclusions, none of the existing models may be used to capture all the three modes of soil resistance completely. There exists therefore a clear need to calibrate the springs of the proposed model, which may be successively employed for the evaluation of the overall foundation stiffness; evaluating the lateral, rocking an coupled stiffness at the top of the foundation may be successively used in analyses of structural response to replace the continuum formulation of the infinite domain and foundation element by the foundation-soil stiffness matrix. As explained in section 5.1, the proposed model is calibrated based on 3D finite element simulation results by equating stiffness components of the foundation system and back-calculating thus the spring expressions as a function of the material stiffness and geometry characteristics of the foundation.

### 5.5 Calculation of distributed and base springs

The variation of all four springs as a function of the foundation aspect ration is shown in **Figure 5.7.**

When the springs are estimated based on the finite element calculated stiffness matrix through the *flexibility approach*, it is observed that

(a) The base rotation spring $k_{b\theta}$ decreases very fast with D/B and becomes zero for D/B = 0.75. For higher D/B ratios it shows a random variation and gives negative values.

(b) The distributed rotational spring $k_{\theta}$ increases with D/B but beyond D/B = 5-6, its contribution decays and eventually becomes zero.

The trend observed above is interpreted as directly stemming from the spring derivation process itself. The stiffness coefficient $K_{rr}$ according to equation 3.15 is given as

$$\frac{K_{rr}}{EB^3} = \left[ \frac{1}{3}\frac{k_x}{E}\left(\frac{D}{B}\right)^3 + \frac{k_{bx}}{EB}\left(\frac{D}{B}\right)^2 + \frac{k_\theta}{EB^2}\left(\frac{D}{B}\right) + \frac{k_{b\theta}}{EB^3} \right]$$

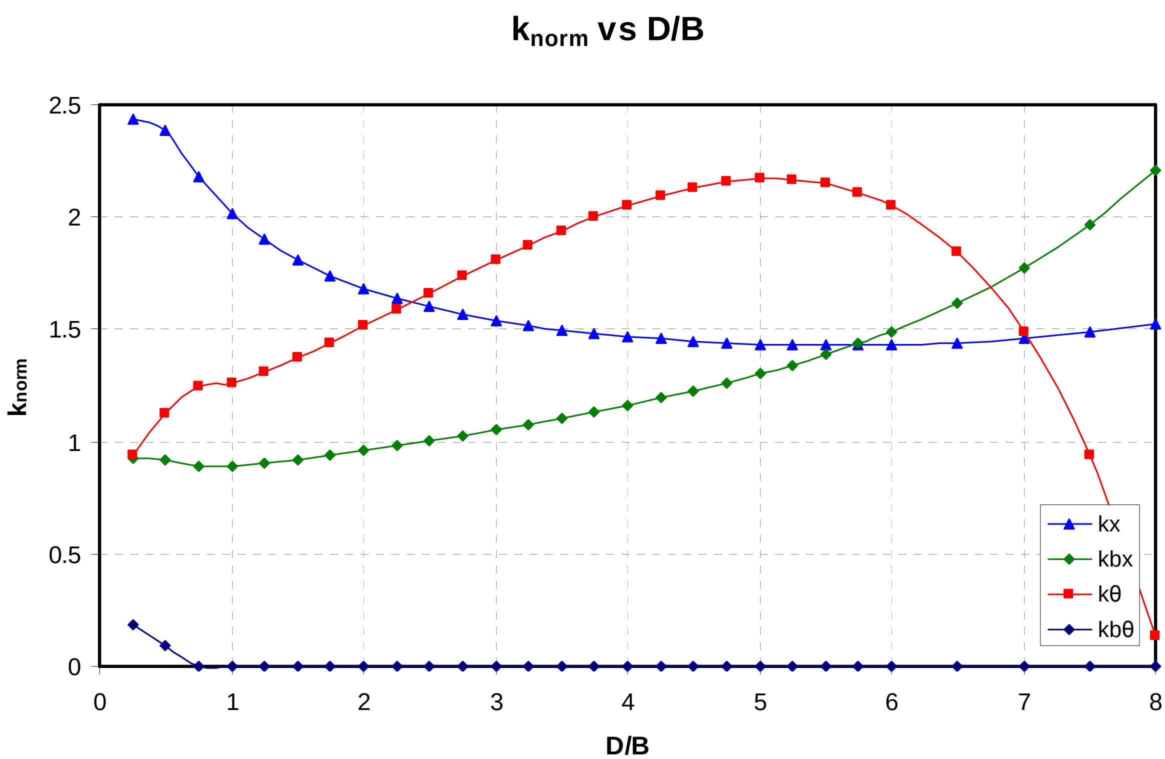


**Figure 5.7** Individual springs obtained as a function of D/B

As the aspect ratio D/B increases, the contribution of $k_\theta$ and $k_{b\theta}$ to the overall rotational stiffness $K_{rr}$ relative to other two terms decreases. As a result, for higher D/B ratios $K_{rr}$ becomes increasingly insensitive to changes in values of these two springs. Since the sensitivity of $K_{rr}$ to $k_\theta$ and $k_{b\theta}$ decreases as D/B increases, it is not possible to interpret the values of these two springs through the equation requirement on $K_{rr}$ beyond a certain D/B ratio, which corresponds to D/B=0.75 for $k_{b\theta}$ and D/B=5-6 for $k_\theta$. Since

$k_\theta$ is a function of D/B as well, the D/B range where $k_\theta$ may be interpreted without loss of accuracy is wider than the corresponding one for $k_{b\theta}$.

As can be readily seen, for the D/B region beyond which the rocking stiffness expression becomes insensitive to a given spring value, this spring (i.e. mechanism of soil resistance) may be neglected altogether resulting in a simplified version of the model. Based on this interpretation, the response of pier can be broadly classified into three main zones:

**Zone I**: D/B= 0-2 (four spring model)

(a) The distributed lateral spring $k_x$ decreases rapidly with D/B ratio. This behavior is most possibly attributed to the fact that at higher embedment depths, the soil layers respond almost independently to each other, and the shear resistance mobilized between the layers is not substantial; this is equivalent ot the assumption for plane strain conditions similar to the model proposed by Novak. On the other hand, for small foundation embedment depths, there is much more interaction between the adjacent layers, namely the plane strain assumption is not valid and hence higher resistance is mobilized due to shear interaction between consecutive soil layers.

(b) The base lateral spring $k_{bx}$ has an initial value of 0.92 which is almost identical to the value predicted by the formulation by Velestos for horizontal impedance of circular foundations on halfspace. However, as D/B ratio increases, $k_{bx}$ increases. This is explained by the so-called *trench effect*, according to which the soil at deeper layers is more constrained as compared to the surface and therefore mobilizes a higher shear resistance.

(c) The distributed rotational spring $k_\theta$ increases with D/B.

(d) The base rotation spring $k_{b\theta}$ has an initial value of 0.18 for D/B =0.25 which is a very good approximation to the theoretical rocking stiffness predicted by the formulation by Velestos. Nonetheless, since the relative contribution of this spring to total rocking stiffness is very small, it may be neglected with no loss of accuracy in the solution for D/B > 1.

**Zone II**: D/B=2-6 (three spring model)

(a) The distributed lateral spring $k_x$ decreases slightly with D/B and then remains practically constant. The normalized value of $k_x / E$ =1.48 which is somewhat comparable to the value of 1.15 predicted by Novak for very low frequencies.

(b) The base lateral spring $k_{bx}$ increases with D/B ratio throughout as expected due to *trench effect*.

(c) The distributed rotational spring $k_\theta$ increases with D/B and then becomes nearly constant. The increase is explained by the increase in confinement due to *trench effect* and higher shear resistance mobilized at the sides.

**Zone III:** D/B > 6 (two spring model)

(a) The distributed lateral spring $k_x$ remains almost constant with D/B.

(b) The base lateral spring $k_{bx}$ keep increasing with D/B.

However, as observed from the simulations for impedance contrast between the foundation and soil, for D/B > 6, for concrete piers, the response of pier starts deviating significantly from the perfectly rigid assumption. For D/B ratios greater than this, the caisson behaves as a flexible foundation and the response can be estimated by using the p-y curve approach. For a linear elastic medium, the p-y curve is represented by the constant lateral spring $k_x$.

### 5.5 Simplified expression for springs

The objective of this study is the spring model calibration for aspect ratios D/B = 2-6 since to behavior observed in Zones I and III may be captured by formulations available for embedded foundations and piles respectively. Using the values of springs obtained by means of the finite element simulations, simple expressions are derived by means of least-square curve fitting as follows:

$$\frac{k_x}{E} = 1.828\left(\frac{D}{B}\right)^{-0.15} \tag{5.7}$$

$$\frac{k_{bx}}{EB} = 0.669 + 0.129\left(\frac{D}{B}\right) \tag{5.8}$$

$$\frac{k_\theta}{EB^2} = 1.106 + 0.227\left(\frac{D}{B}\right) \tag{5.9}$$

The fitted expressions and standard deviation of the results is shown in **Figures 5.8a-c** for the lateral distributed, base concentrated lateral and distributed rotational stiffness respectively.

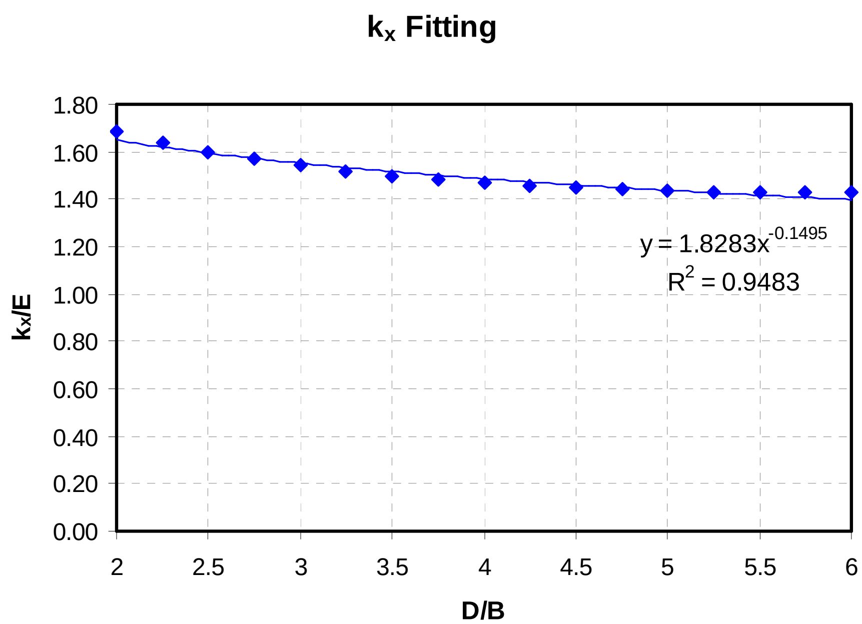


**Figure 5.8 (a)** Curve fitting to $k_x$

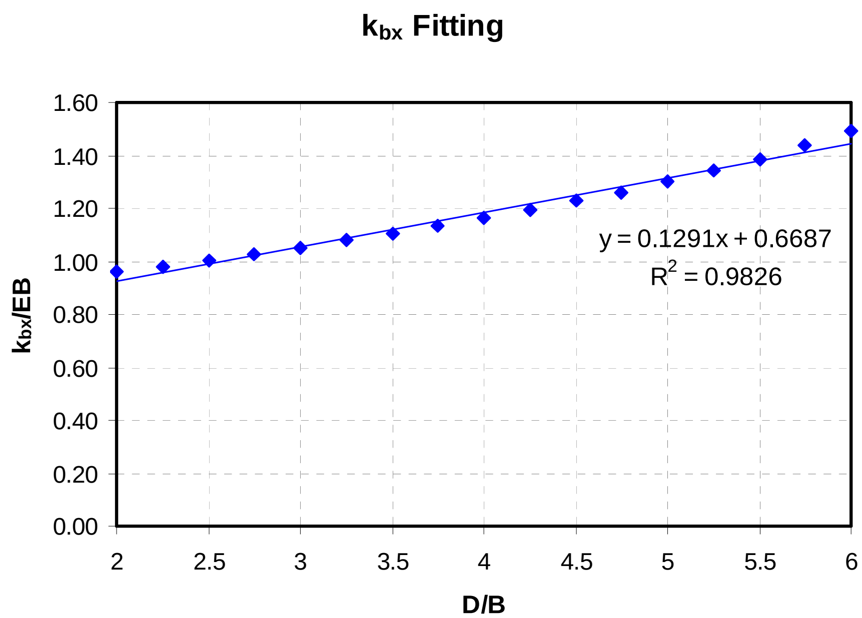


**Figure 5.8 (b)** Curve fitting for $k_{bx}$

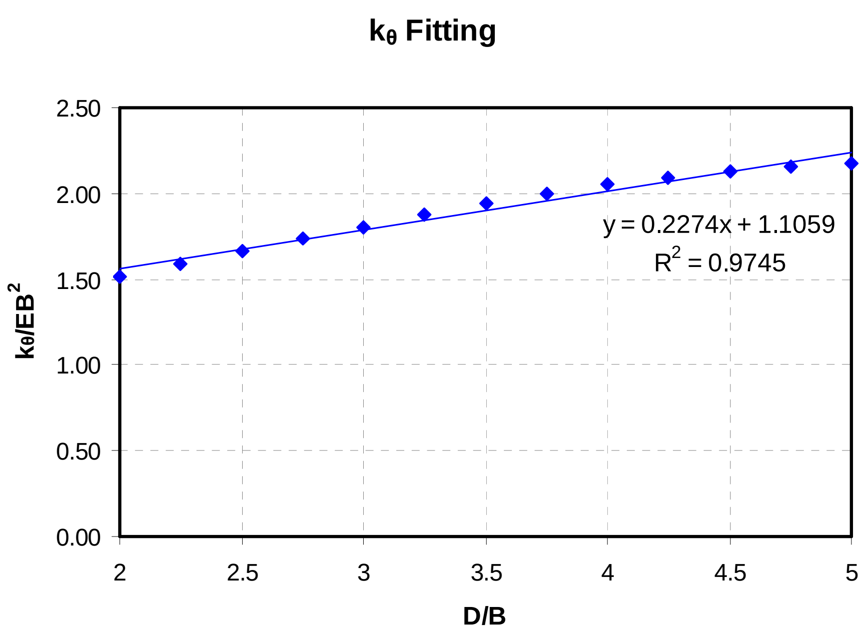


**Figure 5.8 (c)** Curve fitting for $k_{\theta}$

Using the expressions derived by curve fitting, the overall foundation stiffness terms are calculated and the comparison with the corresponding values obtained directly through 3D finite element simulations is shown in **Figures 5.9a-c**. The excellent agreement between the analytically evaluated and numerical values shows that the error propagation due to the curve fitted approach used to evaluate the individual expressions is minimal.

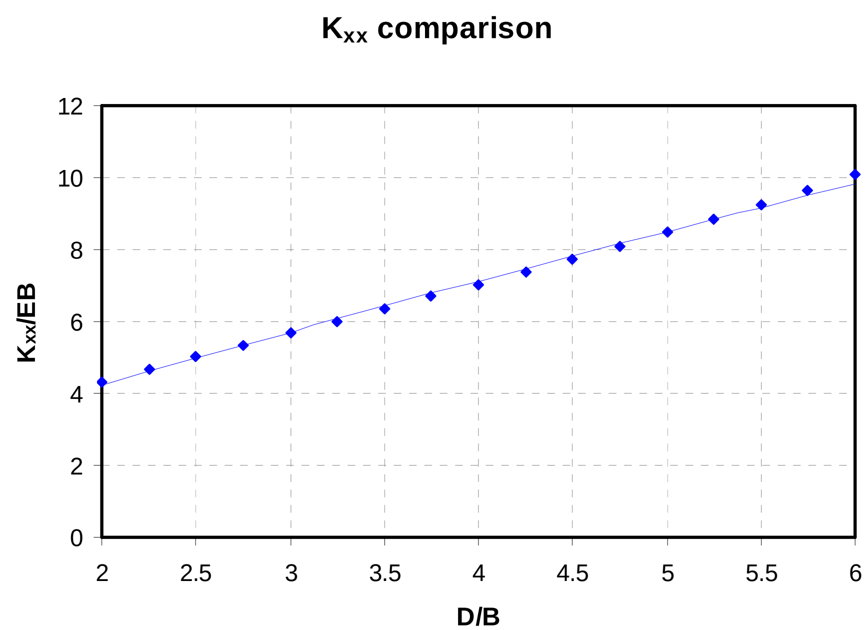


**Figure 5.9 (a)** Comparison showing $K_{xx}$ obtained from fitted springs and 3D simulations

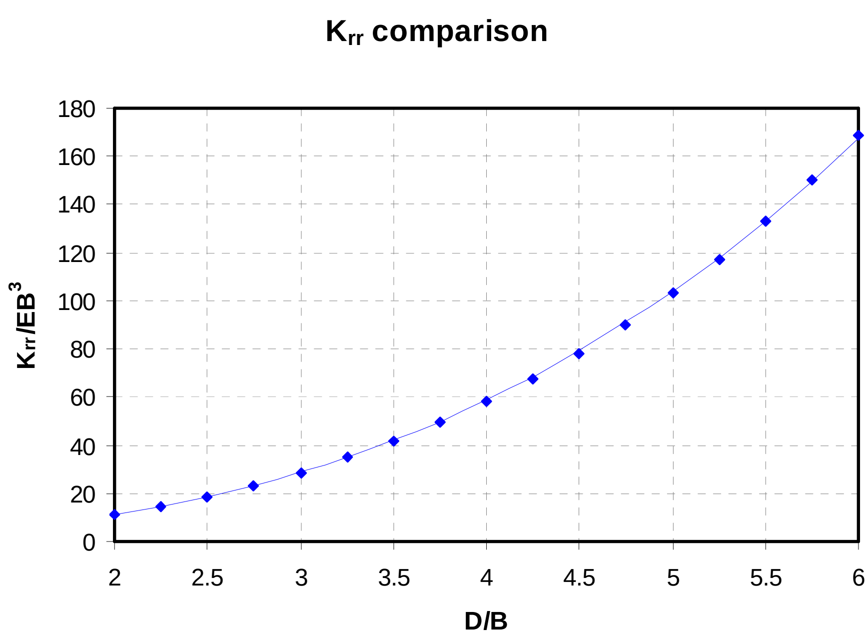


**Figure 5.9 (b)** Comparison showing $K_{rr}$ obtained from fitted springs and 3D simulations

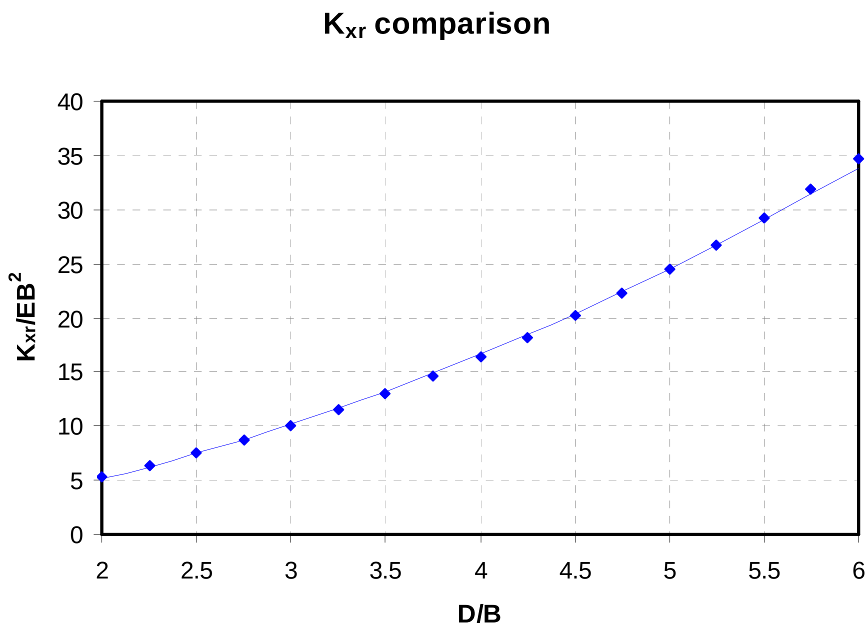


**Figure 5.9 (c)** Comparison showing $K_{xr}$ obtained from fitted springs and 3D simulations

### 5.6 Effect of Poisson Ratio

In the foregoing, the simulations have been conducted for a soil Poisson's ratio equal to $\nu$= 0.3. Additional simulations were next conducted for Poisson ratio varying from 0.1 to 0.49. **Figures 5.10 (a)-(c)** illustrate the effect of Poisson ratio on the stiffness of the various model springs.

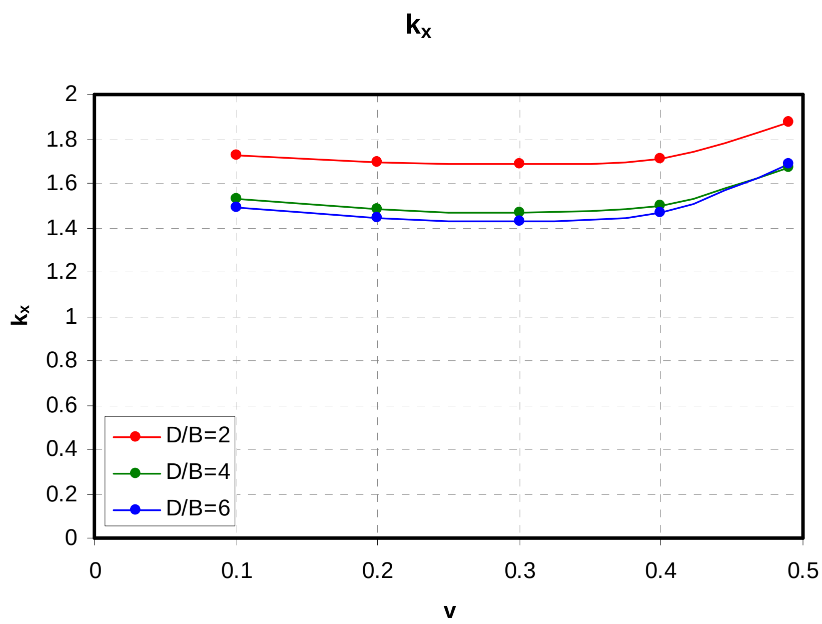


**Figure 5.10 (a)** Effect of Poisson ratio on $k_x$

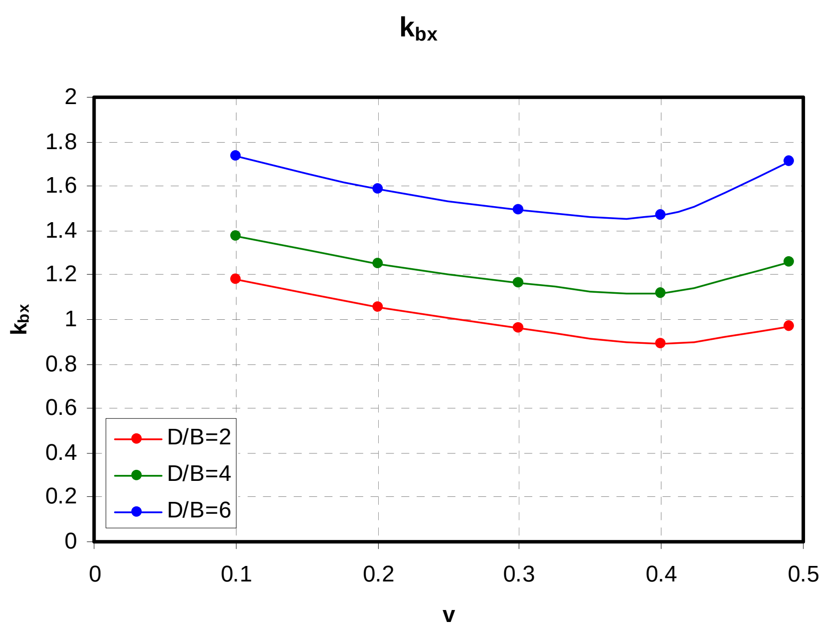


**Figure 5.10 (b)** Effect of Poisson ratio on $k_{bx}$

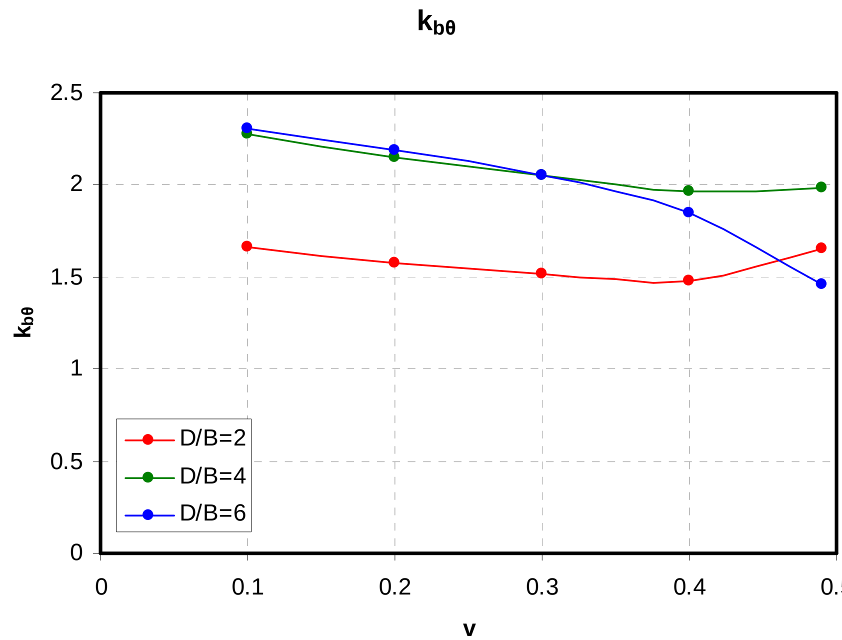


**Figure 5.10 (c)** Effect of Poisson ratio on $k_\theta$

Based on the results shown above, it is concluded that:

1. $k_x$ is almost constant with Poisson ratio except for values very close to 0.5, which is probably due to inability of FEM method to capture perfectly incompressible soils.

2. $k_{bx}$ decreases with Poisson ratio and the decrease can be quite accurately captured by a factor of $\frac{1}{(1+\nu)(2-\nu)}$ which follows logically from the analytical formulation by Velestos.

3. $k_\theta$ decreases slightly with Poisson ratio, but since the sensitivity of total stiffness terms is very little to this spring, the variation can be ignored.

Nonetheless, the overall stiffness terms are practically insensitive to changes in Poisson ratio as shown in **Figures 5.11 (a)-(c)** and **Figures 5.12 (a)-(c)**. Thus, as a simplification, the variation of spring coefficients with Poisson ratio may be safely neglected without loss of accuracy, and the springs are heretofore assumed to be constant and independent of the value of Poisson ratio.

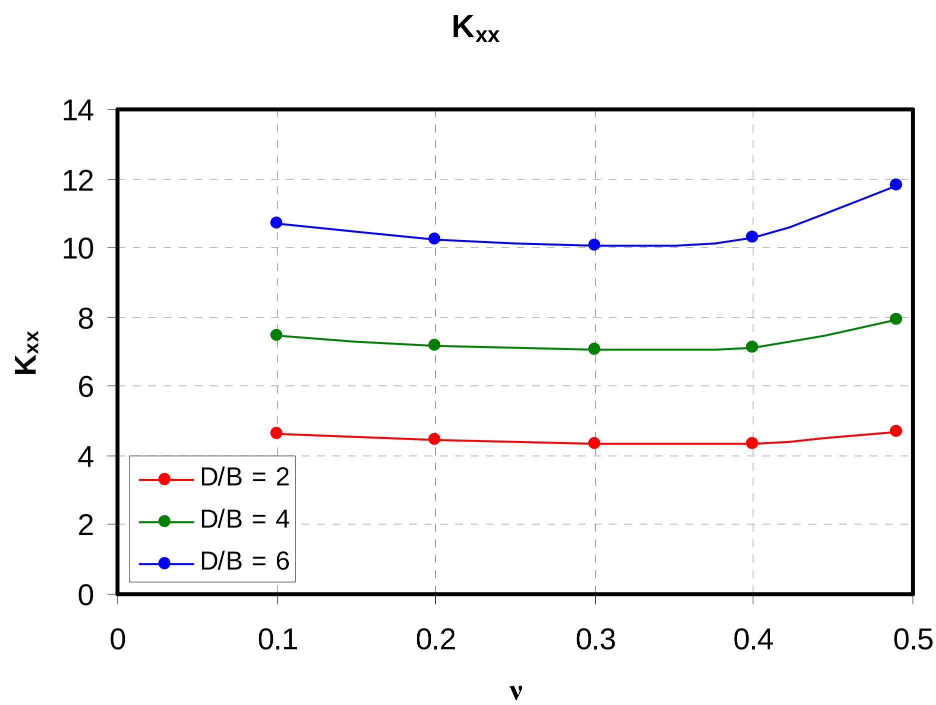


**Figure 5.11 (a)** Effect of Poisson ratio on $K_{xx}$ for different D/B ratios

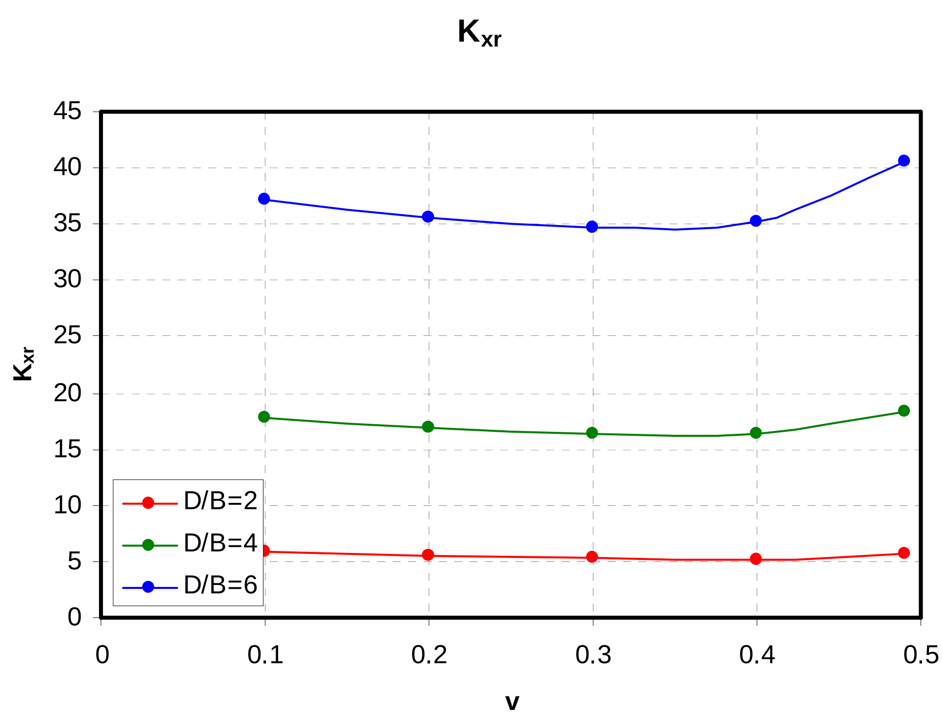


**Figure 5.11 (b)** Effect of Poisson ratio on $K_{xr}$ for different D/B ratios

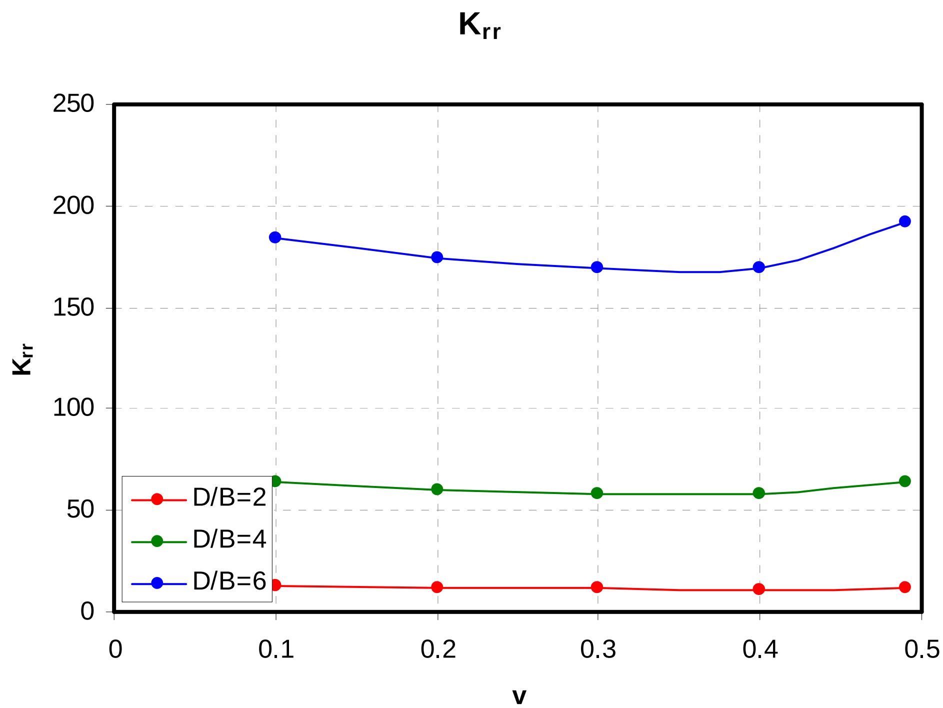


**Figure 5.11 (c)** Effect of Poisson ratio on $K_{rr}$ for different D/B ratios

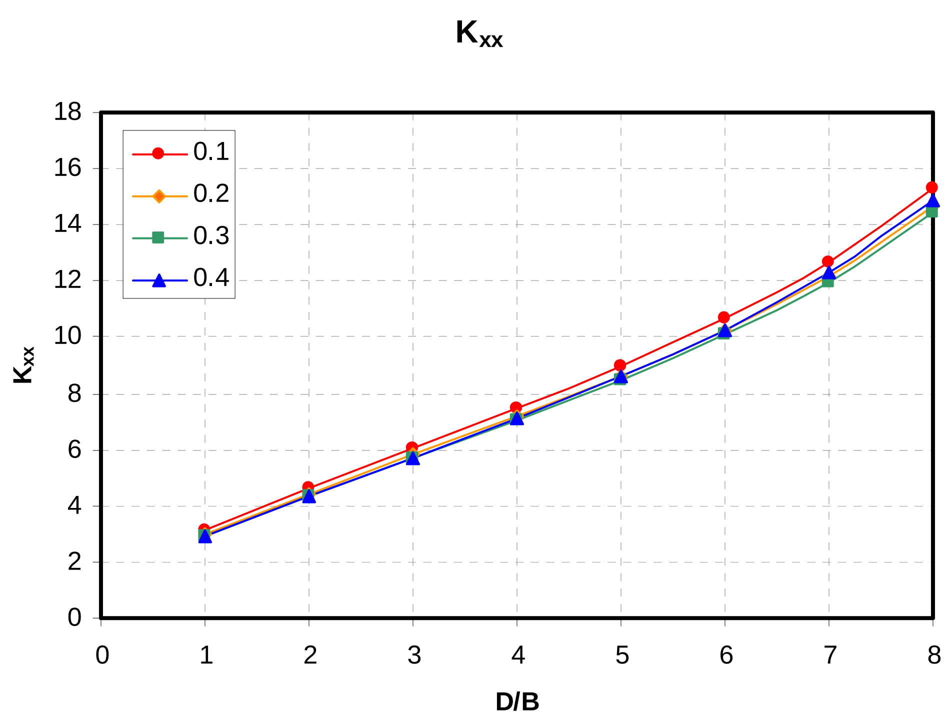


**Figure 5.12 (a)** Variation of $K_{xx}$ with D/B for different Poisson ratios

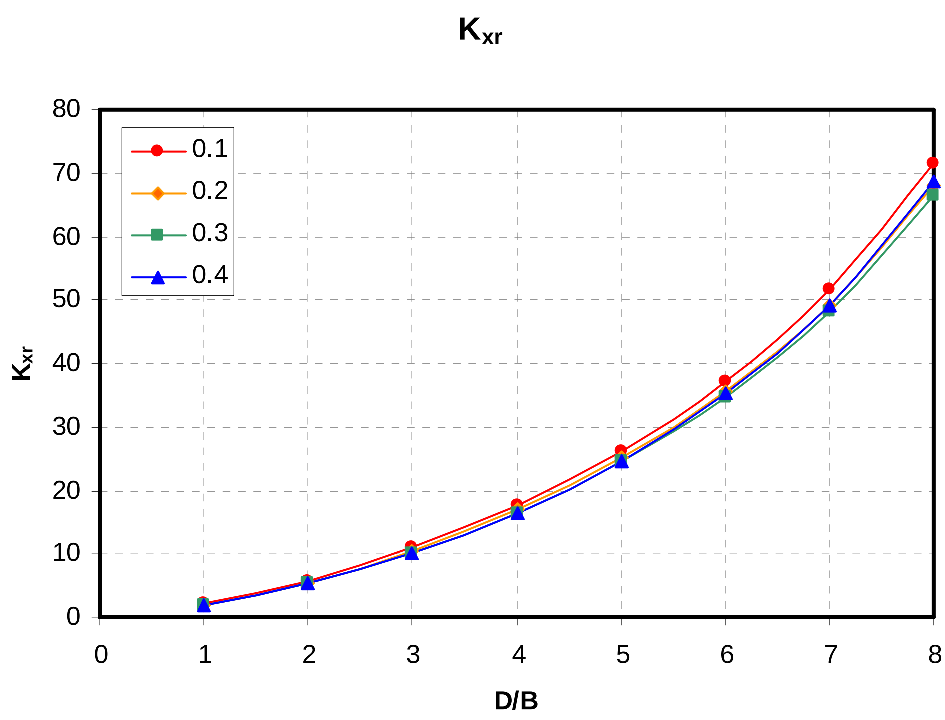


**Figure 5.12 (b)** Variation of $K_{xr}$ with D/B for different Poisson ratios

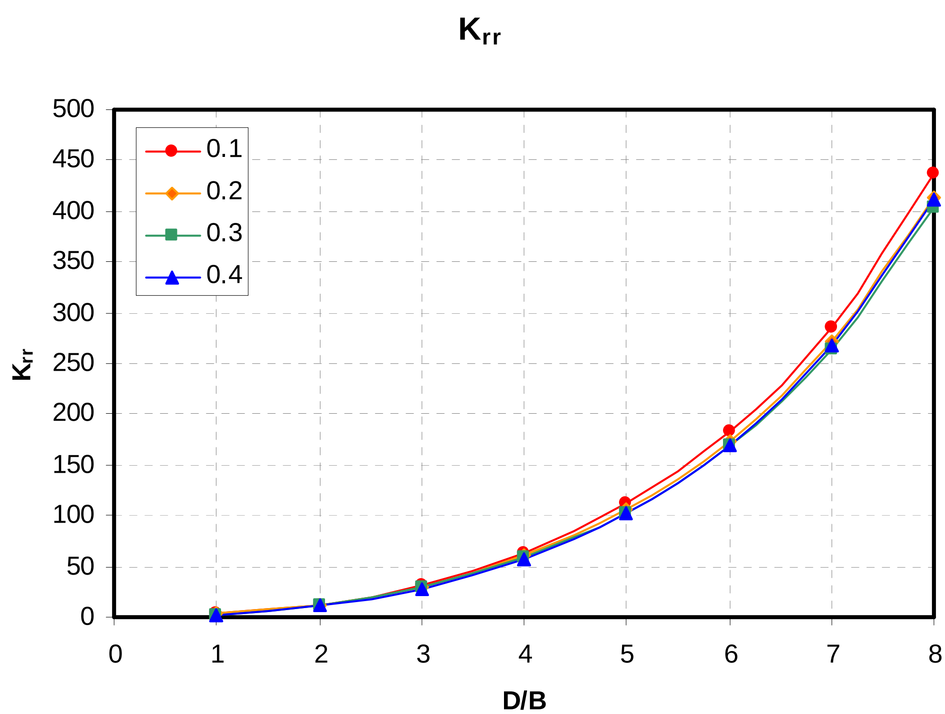


**Figure 5.12 (c)** Variation of $K_{rr}$ with D/B for different Poisson ratios

### 5.7 Eccentric loading and center of foundation rotation

Additional parametric studies have been conducted for simultaneous application of lateral load and overturning moment. The results are presented as a function of dimensionless eccentricity $e = VD / M$ . **Figure 5.13** shows the change of location of the centre of rotation as a function of eccentricity of loading. The concept is shown in **Figure 5.14.**

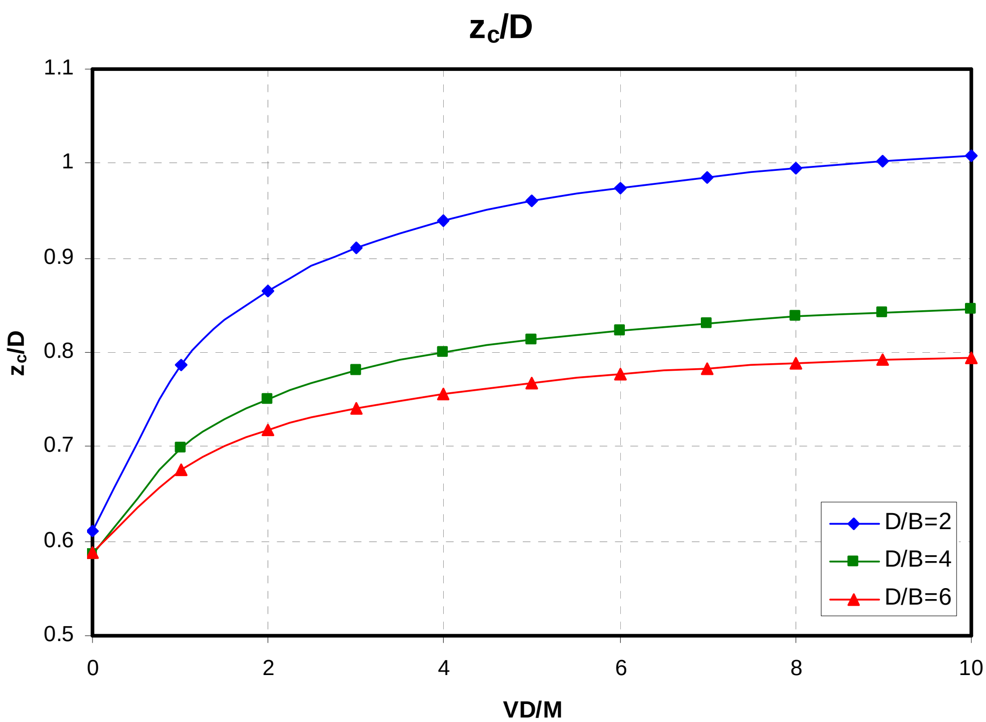


**Figure 5.13** Movement of centre of rotation with change in loading eccentricity

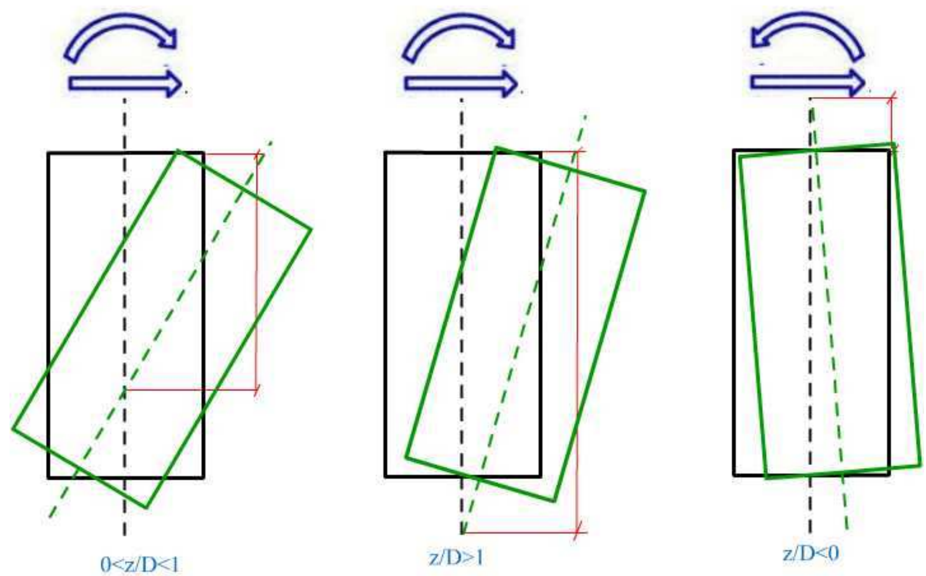


**Figure 5.14** Figure showing the physical interpretation of 0 <$z_c$/D<1, $z_c$/D>1, and <0

Successively, **Figures 5.15 (a)-(b)** show the effective lateral stiffness $V/EBu$ and rocking stiffness $M/EB^3\theta$ as a function of eccentricity in loading.

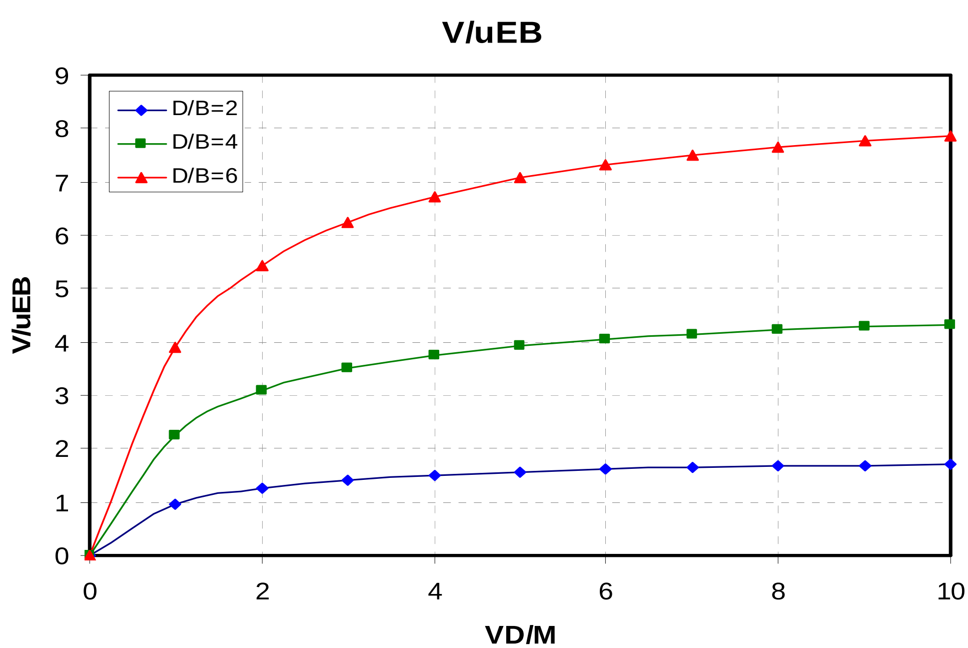


**Figure 5.15(a)** Effective lateral stiffness as a function of loading eccentricity

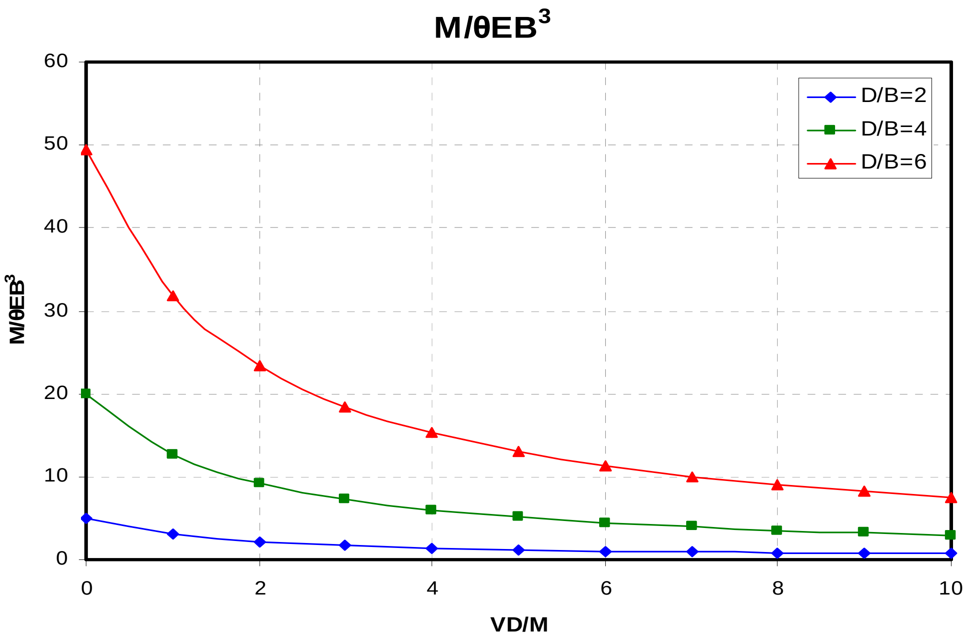


**Figure 5.15(b)** Effective rocking stiffness as a function of loading eccentricity

# CHAPTER 6

# FORCED TRANSVERSE VIBRATION OF CAISSON

This chapter describes how the static springs are modified to complex springs to account for stiffness and attenuation in the system. The methodology to obtain the dynamic impedance matrix uses sinusoidal loads instead of static step functions. Approximate expressions are then obtained for stiffness and attenuation coefficients of the springs as a function of D/B ratio and dimensionless frequency parameter. Finally, a comparison is presented between the values of dynamic impedance matrix obtained using fitted expressions and those obtained from 3D simulations.

## 6.1 Formulation and calculation of stiffness matrix and springs

For the dynamic loading case evaluated in this part of the study, the static springs previously evaluated are replaced by complex impedance functions of the form:

$$K^* = K_{stat} k'(a_o) + i a_o C(a_o) \tag{6.1}$$

where

$K_{stat}$ = Static stiffness

$a_o$ = Dimensionless frequency $a_o = \dfrac{\omega B}{V_s}$

$k(a_o)$ = Frequency dependent stiffness coefficient

$C(a_o)$ = Frequency dependent damping parameter.

As discussed in Chapter 2, $C(a_o)$ represents the effective damping of the soil-foundation system, which is a combination of energy radiation towards the far-field and material damping. Thus Equation 3.8 for displacement and rotation due to any loading changes for the dynamic loading case to:

$$\begin{bmatrix} V^* \\ M^* \end{bmatrix} = \begin{bmatrix} K_{xx}^* & K_{xr}^* \\ K_{xr}^* & K_{rr}^* \end{bmatrix} \begin{bmatrix} u_r^* \\ \theta^* \end{bmatrix} \tag{6.2}$$

and equation 5.2 for back derivation of stiffness matrix becomes equivalently:

$$\begin{bmatrix} K_{xx}^* & K_{xr}^* \\ K_{xr}^* & K_{rr}^* \end{bmatrix} = \begin{bmatrix} u_V^* & u_M^* \\ \theta_V^* & \theta_M^* \end{bmatrix}^{-1} \tag{6.3}$$

where the displacements and rotations are complex values as well, representing the response amplitude and phase lag between externally applied loading and foundation response. The Eigen-functions of the system of equations shown above are represented by sinusoidal functions.

Therefore, for the case of dynamic analyses, lateral forces and moments are applied on the top of the pier in the form of a sinusoidal function, and the magnitude and phase difference between the applied function and the foundation response, namely the displacement and rotation sinusoids, are evaluated.

The complex stiffness matrix can then be evaluated by inverting the matrix in Equation 6.3, similarly to the static case and accounting for the complex form of the response in this case. The real and imaginary parts for the springs can successively be calculated from the real and imaginary parts of the stiffness matrix, respectively.

## 6.2 Model simplification – 3 spring model

In Chapter 5, it was shown that for the D/B range of interest (namely in the range D/B=2-6), the stiffness component of base rotational spring $k_{b\theta}$ is negligible.

Gazetas (1983) showed that for base rotational resistance mechanism, any two points located on the opposite side of the base give rise to waves that are 180 degrees out of phase with each other, and hence tend to cancel each other out when they meet at distant location along the centerline. As a result they cannot reach long distances and no significant amount of energy is radiated.

Since, the base resistance mechanism doesn't contribute significantly to either stiffness or the damping part it can be completely neglected, and the resulting model is a simplified 3-spring Winkler formulation.

### 6.3 Variation of stiffness coefficient and damping with frequency

The variation of stiffness coefficient $k'$ and damping parameter C with dimensionless frequency $a_o$ is shown in **Figures 6.1 (a)-(f)**. Approximate expressions for the stiffness coefficients and soil-foundation attenuation that have been developed as part of this work are given below, and the comparison between approximated and actual values is also shown in **Figures 6.1 (a)-(f)**.

(a) $k_x^{'}$: The lateral resistance distributed stiffness coefficient decreases with increasing frequency as shown in **Figure 6.1 (a)**. The numerically derived variation shows many fluctuations with frequency, which are probably caused by local resonances inside the model due to

a. The finite dimensions of the model; and

b. The imperfect absorbing conditions in the far-field numerical boundaries.

Nonetheless, for all three D/B ratios presented here, the variation may be approximated by the following expression

$k_x^{'} = 1 - 0.1 a_o$

(b) $k_{bx}^{'}$: The lateral base resistance stiffness coefficient also shows some fluctuations with frequency as shown in **Figure 6.1(b)**, most probably due to the same effects discussed above. However, for practical purposes and simplicity, it can be assumed to be almost constant, namely

$k_{bx}^{'} = 1$

(c) $k_\theta^{'}$: The side rotational stiffness coefficient also shows a decreasing trend with frequency as shown in **Figure 6.1(c)**. The decreasing trend can be approximated as:

$k_\theta^{'} = 1 - 0.225 a_o$.

The validity of the approximate expressions derived above will be evaluated in the ensuing by comparison of the analytically predicted response computed by means of the fitted expressions to the numerically predicted response of the foundation-soil system.

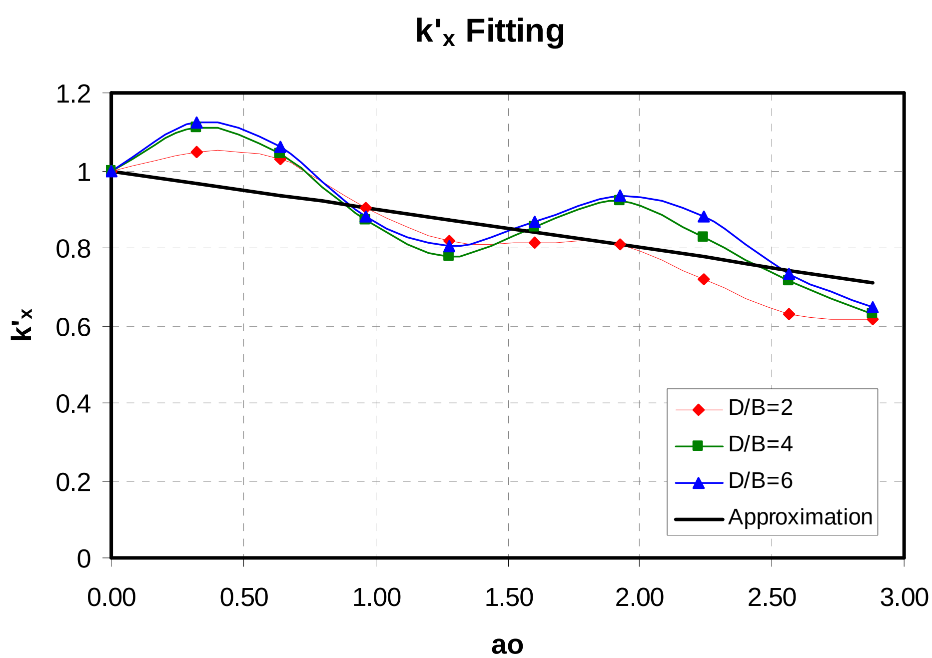


**Figure 6.1(a)** Variation of $k_x^{'}$ with frequency

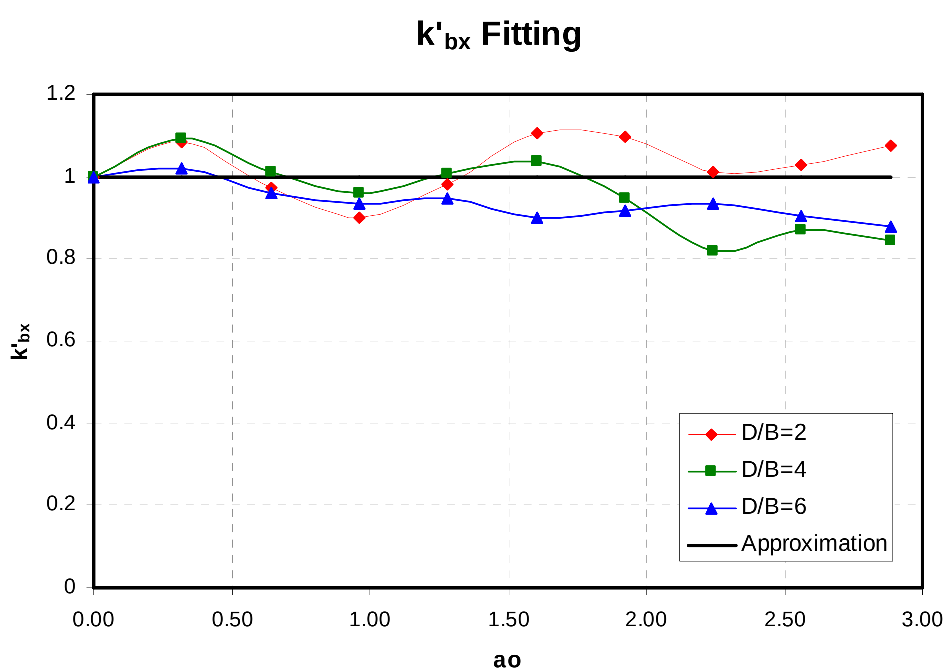


**Figure 6.1(b)** Variation of $k_{bx}^{'}$ with frequency

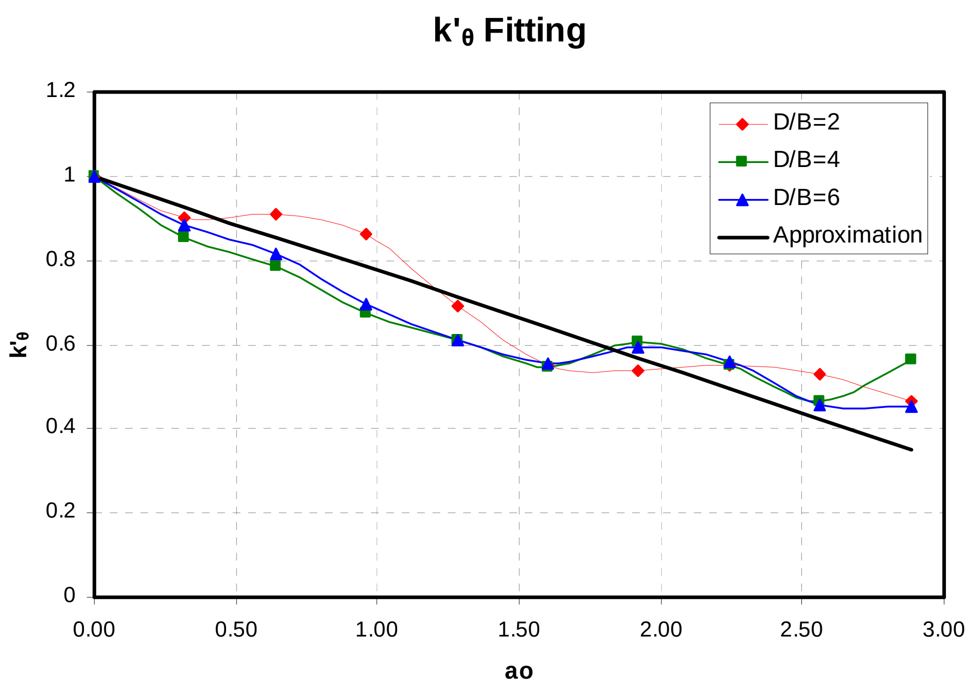


**Figure 6.1(c)** Variation of $k_\theta^{'}$ with frequency

(d) $C_x$: The attenuation (material and radiation damping) for lateral side resistance increases as frequency increases, but becomes constant for normalized frequencies beyond $a_o$ =1. The approximation is given as:

$$C_x = \begin{cases} 1.85a_o & a_o < 1 \\ 1.85 & a_o > 1 \end{cases}$$

This expression implies that the overall system energy attenuation increases almost linearly with frequency for $a_o$ >1.

(e) $C_{bx}$: The attenuation coefficient associated with base shear also shows a similar trend as $C_x$ as shown in **Figure 6.1(e)** and is approximated as:

$$C_{bx} = \begin{cases} 0.6a_o & a_o < 0.6 \\ 0.36 & a_o > 0.6 \end{cases}$$

(f) $C_\theta$: Unlike the attenuation coefficients presented above, $C_\theta$ results in a negative value as shown in **Figure 6.1(f)**. Counter-intuitively, the negative value does not imply the supply of energy into the system; instead, it indicates that the waves produced by the side shear resistance are out of phase with those produced by other resisting mechanisms. As a result the wavefield produced by this mechanism destructively interferes with the wavefield produced by other mechanisms to some extent and reduces the radiation of energy away from the system.

This attenuation coefficient increases with frequency for values of normalized frequency $a_o$ <1, beyond which it decreases. Above values of normalized frequency $a_o$ =2, it becomes almost zero indicating that no energy is being radiated towards the far-field due to this mechanism, and the wavefield for higher frequency excitations tend destructively interfere for the rocking mechanism. This behavior for side rotational resistance mechanism is quite similar to the one for base rotational resistance as described above. Furthermore, the value of this parameter is found to increase with increasing D/B ratio. A simple approximation is given by:

$$C_\theta = \begin{cases} -0.21\left(\frac{D}{B}\right)a_o & a_o < 1 \\ -0.21\left(\frac{D}{B}\right)(2 - a_o) & 1 < a_o < 2 \\ 0 & a_o > 2 \end{cases}$$

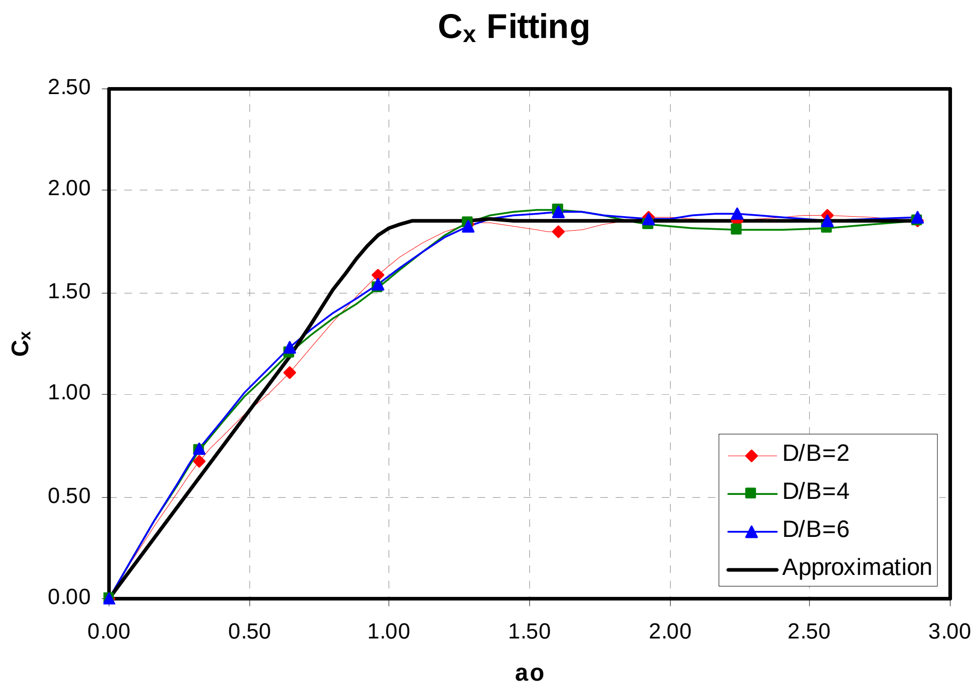


**Figure 6.1(d)** Variation of $C_x$ with frequency

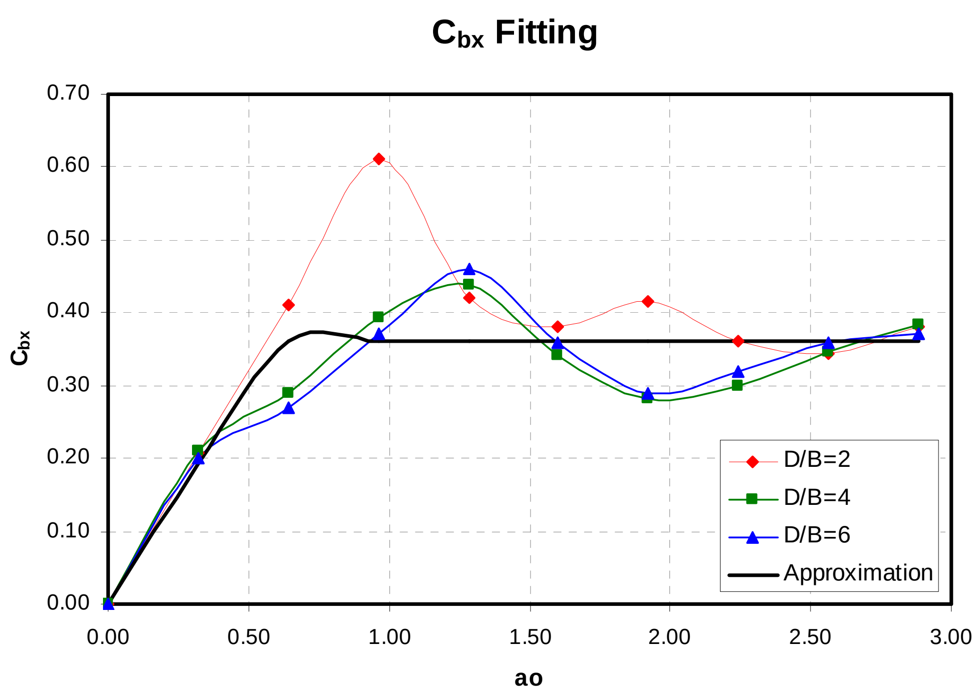


**Figure 6.1(e)** Variation of $C_{bx}$ with frequency

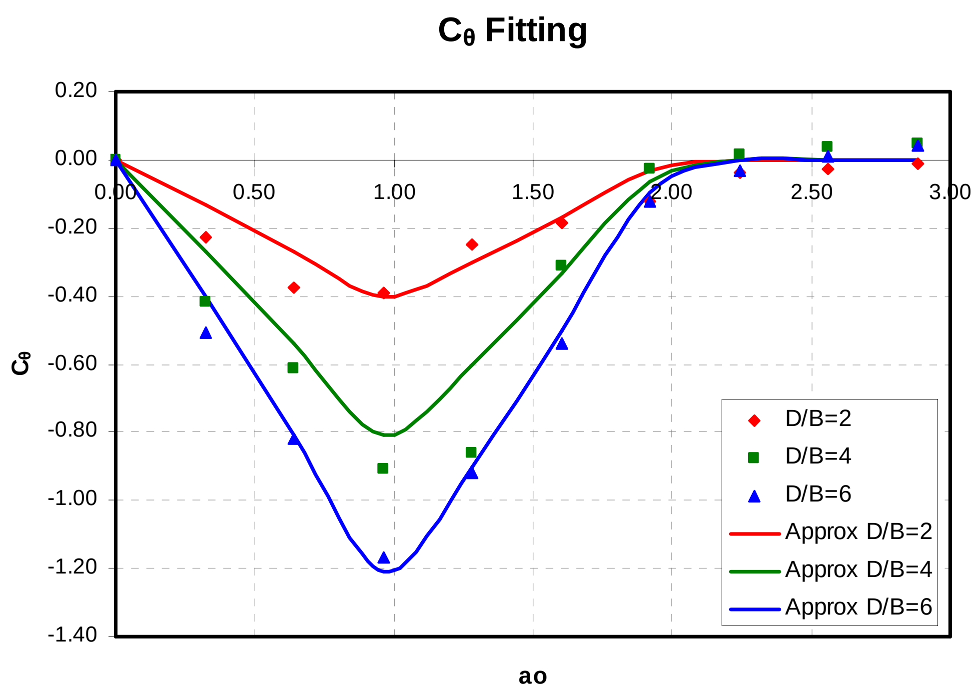


**Figure 6.1(f)** Variation of $C_\theta$ with frequency

### 6.4 Comparison of analytically and numerically evaluated complex stiffness matrix

**Figures 6.2(a)-(f)** show a comparison between the components of the overall foundation stiffness matrix obtained by means of the numerical simulations and the ones obtained by means of the approximate expressions for dynamic impedances. As can be readily seen from the figures, a good approximation is obtained when the fitted expressions derived above are employed.

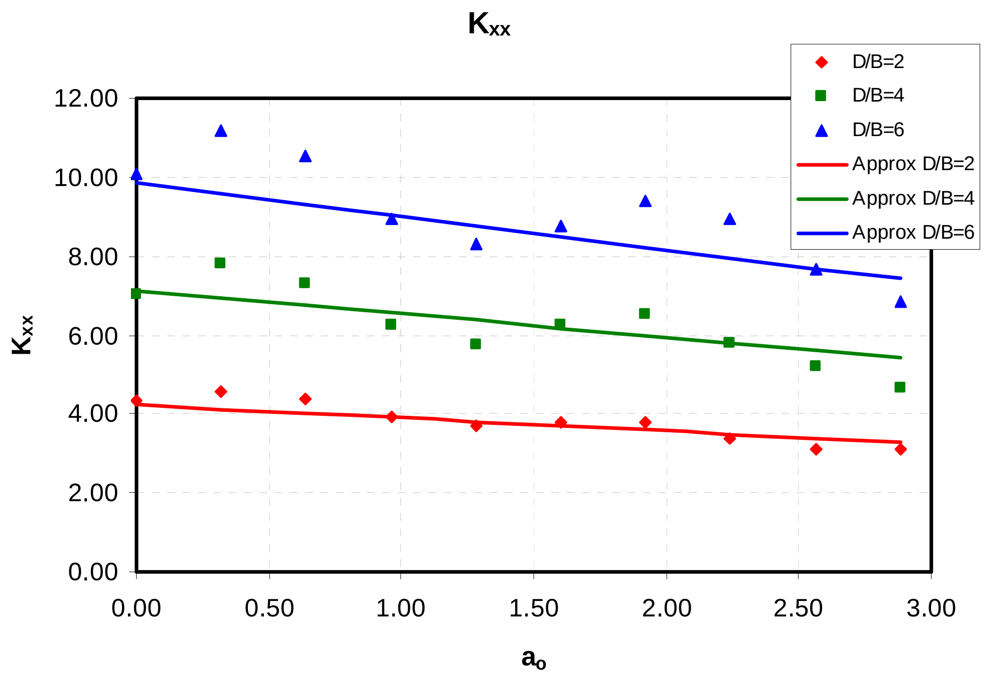


**Figure 6.2(a)** Comparison of $K_{xx}$ with that obtained from approximate expressions

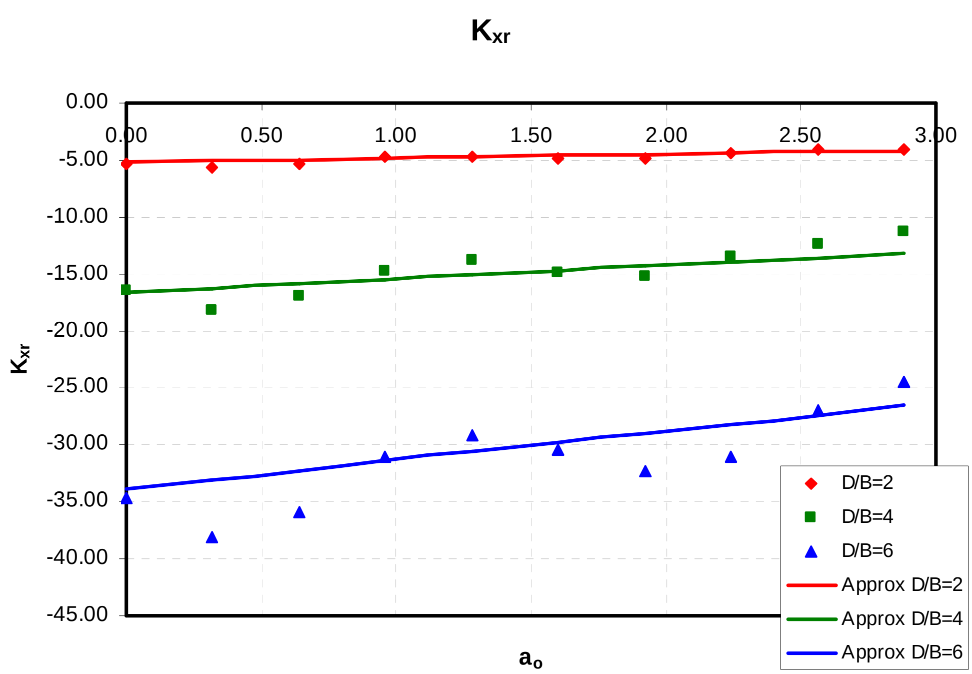


**Figure 6.2(b)** Comparison of $K_{xr}$ with that obtained from approximate expressions

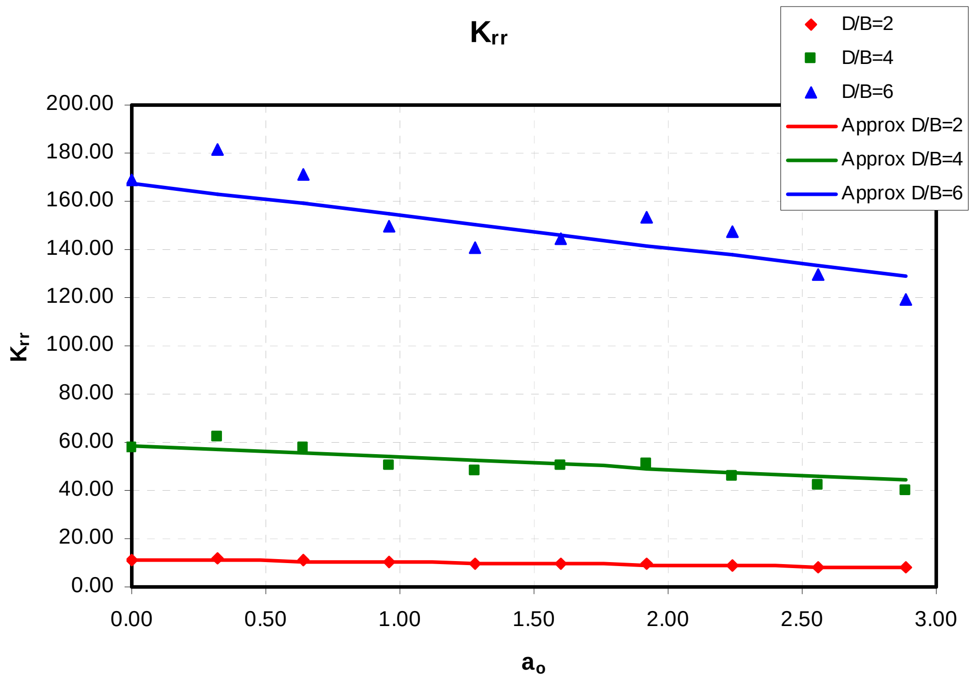


**Figure 6.2(c)** Comparison of $K_{rr}$ with that obtained from approximate expressions

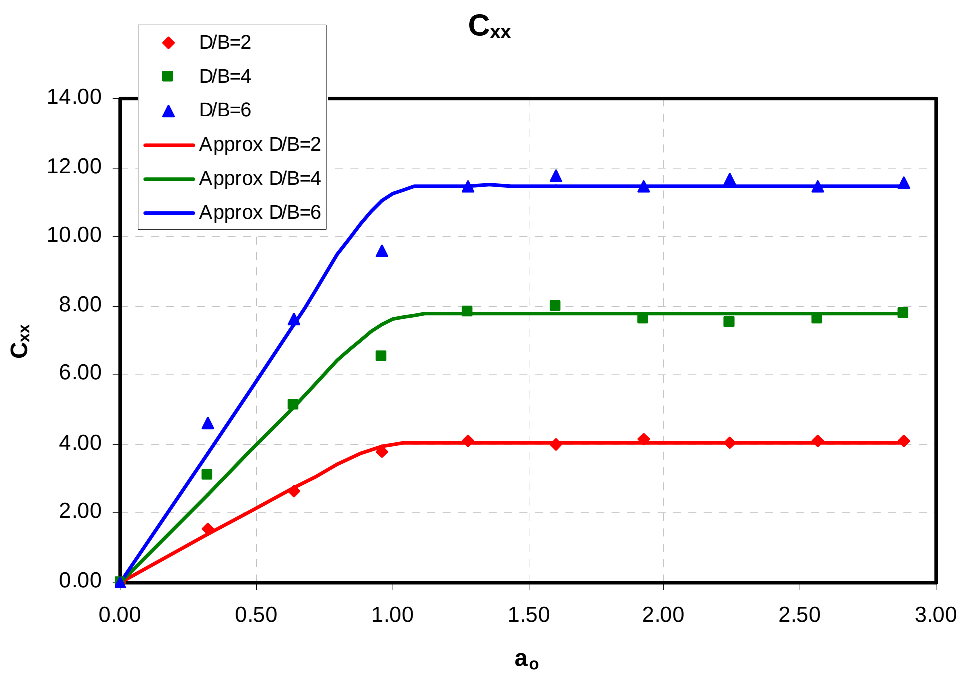


**Figure 6.2(d)** Comparison of $C_{xx}$ with that obtained from approximate expressions

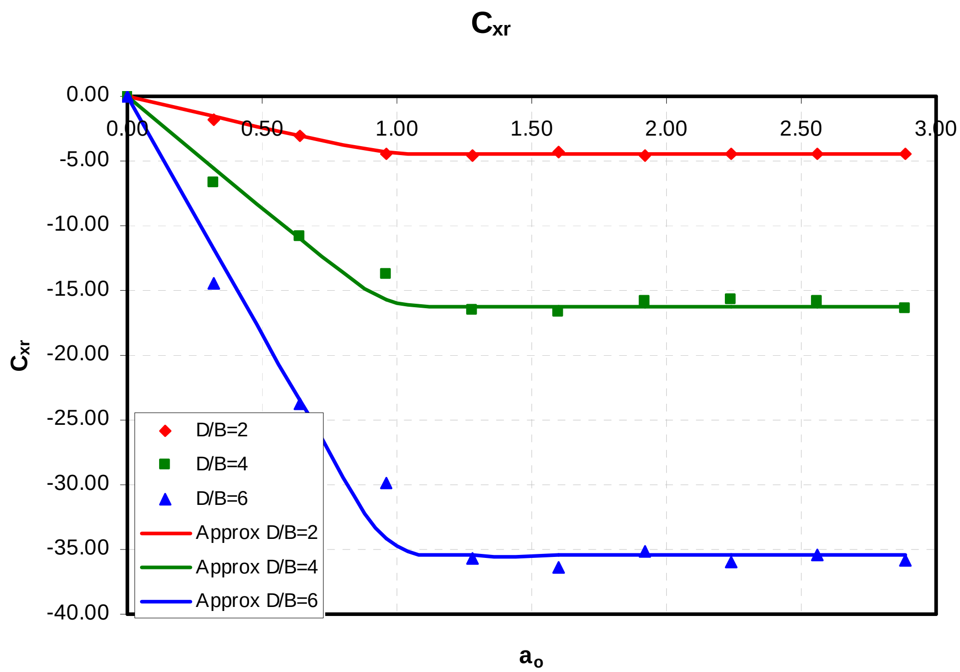


**Figure 6.2(e)** Comparison of $C_{bx}$ with that obtained from approximate expressions

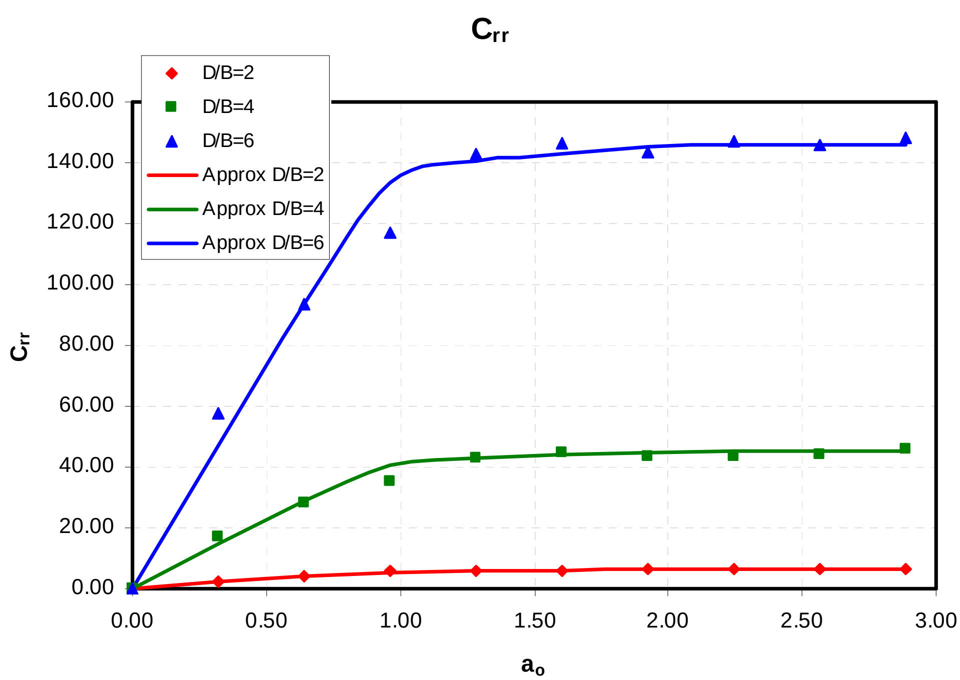


**Figure 6.2(f)** Comparison of $C_{\theta}$ with that obtained from approximate expressions

# CHAPTER 7

# KINEMATIC INTERACTION

This chapter discusses the importance of kinematic interaction effects by presenting some results obtained by Elsabee and Morray (1977) and Day (1977) for embedded shallow foundations. Using the Winkler model proposed, an analytical solution for kinematic interaction of caissons is derived in terms of transfer functions for top displacement and rotation. A comparison between analytically derived transfer functions and those obtained from numerical simulations is also presented.

## 7.1 Significance of kinematic interaction effects

As discussed in Chapter 2, the inability of a stiff foundation to comply to the deformation field imposed by the soil in the free-field, leads to incompatible motion between free-field and the foundation. This difference in motion results in forces and moments being applied on the foundation by free field as shown in **figure 7.1**.

In turn, the rigid behavior of the foundation results in filtering the effects of far-field motion. The filtering is expected to be higher for short wavelengths (i.e. high frequencies). The overall effect of kinematic interaction is expressed in terms of transfer functions

$$H_u(a_o) = \frac{u_t}{u_{ff}} \tag{7.1}$$

$$H_\theta(a_o) = \frac{\theta B}{u_{ff}} \tag{7.2}$$

Day (1977) employed finite element analyses to evaluate the base motion of a shallow rigid cylindrical foundation embedded in half space and subjected to vertically incident coherent SH-waves. Elsabee and Moray (1977) performed similar studies for visco-elastic soil of finite depth over a rigid base, and also proposed approximate transfer functions for the translational and rocking motion of the foundation as follows:

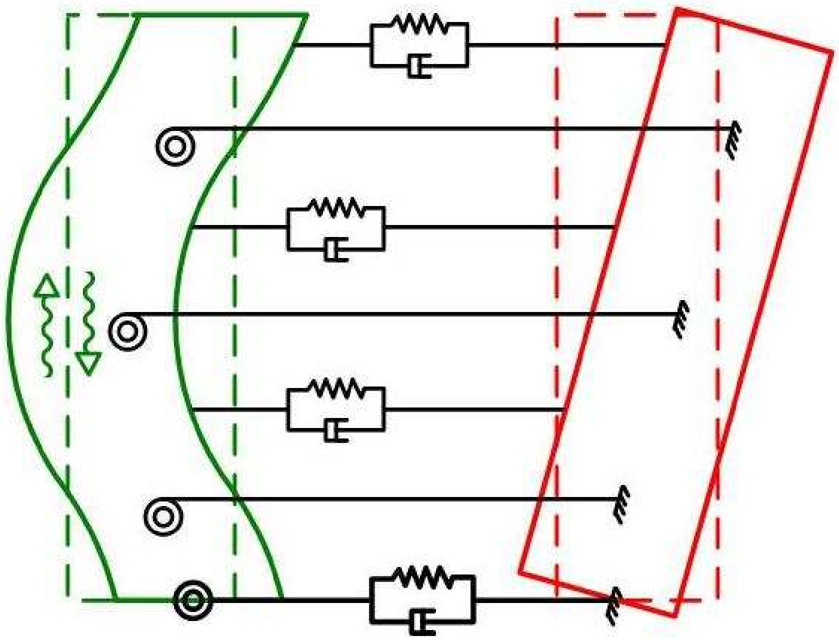

**Figure 7.1** Incompatible motions between foundation and free field

$$|H_u(\omega)| = \begin{cases} \cos\left(\frac{e}{R}a_o\right) & a_o < 0.7\overline{a_o} \\ 0.453 & a_o > 0.7\overline{a_o} \end{cases}$$

$$|H_\theta(\omega)| = \begin{cases} \frac{0.257}{R}\left(1-\cos\left(\frac{e}{R}a_o\right)\right) & a_o < \overline{a_o} \\ \frac{0.257}{R} & a_o > \overline{a_o} \end{cases}$$

where $\overline{a_o} = \frac{\pi}{2}\frac{R}{e}$ and $a_o = \frac{2\pi fR}{V_s}$.

For the finite depth case, due to multiple reflections of waves at surface and from bedrock, the response is a sinusoid with time varying amplitude (i.e., similar to a beat function) instead of a sinusoid with constant amplitude. The frequency of amplitude variation is controlled by the thickness of soil layer. Thus, the transfer functions refer to the maximum displacement and rotation observed instead of the amplitude of the sinusoid as in case of halfspace.

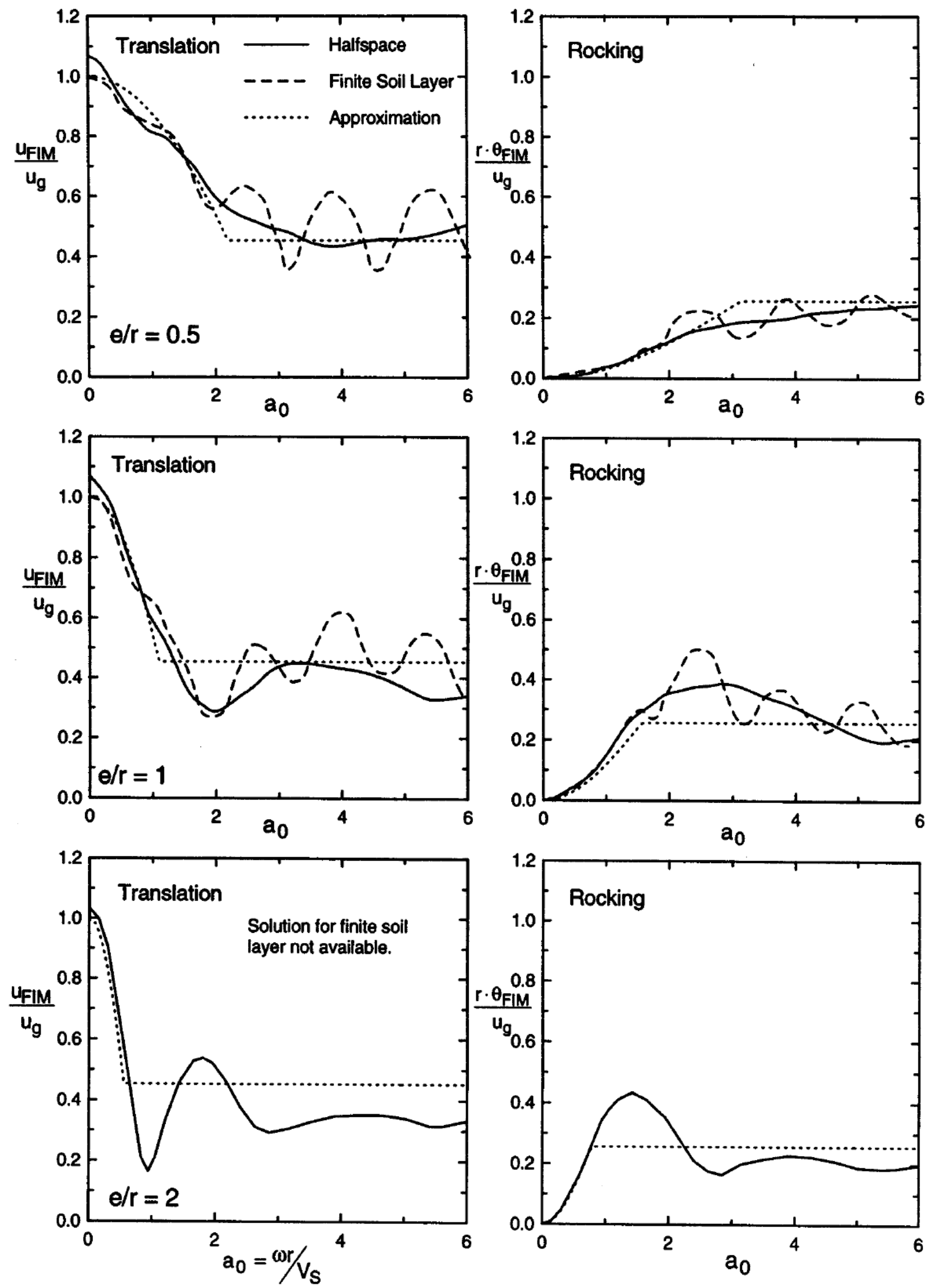


**Figure 7.2** Comparison of amplitude of transfer function for rigid cylindrical foundations embedded in halfspace (Day, 1977), in soil layer of finite thickness and approximation (Elsabee and Morray, 1977). Figure from Stewart et al. (1998)

**Figure 7.2** shows a comparison between the transfer functions obtained by Day (1977) for the case of an underlying halfspace, Elsabee and Morray (1977) for a finite thickness soil layer, and the approximation for three embedment ratios denoted as e/r = 0.5,1 and 2 which correspond to D/B = 0.25, 0.5 and 1.0.

The significant differences between the finite thickness soil layer and the half space arise from the oscillations in transfer function for frequencies $a_o$ >1 due to resonance effects in the finite layer. As a general observation, significant filtering of translational motions is observed for $a_o$ >0.5 and significant rocking motions for $a_o$ >1.0. The filtering effect is shown to increase with frequency for low frequencies, where it is more or less insensitive to frequencies for higher frequencies. By contrast to a circular foundation on the surface of a halfspace, which would experience no reduction in translational motion and no induced rocking, the embedment length increases the kinematic interaction significantly and cannot be neglected even for D/B ratios equal to unity, namely shallow foundations.

For extension of these formulations to cases such like depth-varying soil formations, horizontally propagating SH waves and non-circular foundations, the reader is referred to Elsabee and Morray (1977), Day (1977) and Mita and Luco (1989).

### 7.2 Analytical Solution for kinematic interaction for three spring model

For a sinusoidal SH wave propagating vertically upward in a half space, the solution to the displacement field is given by

$$u_{ff}(\mathrm{z}) = u_{ff}\cos(2\pi\frac{z}{\lambda}) = u_{ff}\cos(\frac{\omega z}{v_s}) = u_{ff}\cos(\frac{\omega B}{v_s}\frac{z}{B}) = u_{ff}\cos(a_o\frac{z}{B})$$

where z is the depth from the surface. For the configuration shown in Figure 7.1, using equilibrium of forces in horizontal direction, the following expression is obtained:

$$\int_0^D k_x^* u_r^*(z)dz + k_{bx}^* u_r^*(D) = 0$$

$$\int_0^D k_x^*\left(u^*(z)-u_{ff}^*(z)\right)dz+k_{bx}^*\left(u^*(D)-u_{ff}^*(D)\right)=0$$

$$\int_0^D k_x^*\left(u_t^*-\theta^* z-u_{ff}^*\cos(a_o\frac{z}{B})\right)dz+k_{bx}^*\left(u_t^*-\theta^* D-u_{ff}^*\cos(a_o\frac{D}{B})\right)=0$$

$$k_x^*u_t^*D-k_x^*\theta^*\frac{D^2}{2}-k_x^*u_{ff}^*\frac{B}{a_o}\sin(a_o\frac{D}{B})+k_{bx}^*u_t^*-k_{bx}^*\theta^* D-k_{bx}^*u_{ff}^*\cos(a_o\frac{D}{B})=0$$

which can be simplified to the following expression:

$$u_t^*\left(k_x^*D+k_{bx}^*\right)+\theta^*\left(-k_x^*\frac{D^2}{2}-k_{bx}^*D\right)=u_{ff}^*\left(k_x^*\frac{B}{a_o}\sin(a_o\frac{D}{B})+k_{bx}^*\cos(a_o\frac{D}{B})\right) \quad (7.3)$$

Similarly, applying moment equilibrium at the top of pier, we obtain the following:

$$-\int_0^D k_x^*u_r^*(z)zdz-k_{bx}^*u_r^*(D)D+\int_0^D k_\theta^*\theta_r^*(z)dz+k_{b\theta}^*\theta_r^*(D)=0$$

$$-\int_0^D k_x^*\left(u^*(z)-u_{ff}^*(z)\right)zdz-k_{bx}^*\left(u^*(D)-u_{ff}^*(D)\right)D+\int_0^D k_\theta^*\left(\theta^*(z)-\theta_{ff}^*(z)\right)dz+k_{b\theta}^*\left(\theta^*(D)-\theta_{ff}^*(D)\right)=0$$

$$-\int_0^D k_x^*\left(u_t^*-\theta^* z-u_{ff}^*\cos(a_o\frac{z}{B})\right)zdz-k_{bx}^*\left(u_t^*-\theta^* D-u_{ff}^*\cos(a_o\frac{D}{B})\right)D$$
$$+\int_0^D k_\theta^*\left(\theta^*+u_{ff}^*\frac{a_o}{B}\sin(a_o\frac{z}{B})\right)dz+k_{b\theta}^*\left(\theta^*+u_{ff}^*\frac{a_o}{B}\sin(a_o\frac{D}{B})\right)=0$$

$$-k_x^*u_t^*\frac{D^2}{2}+k_x^*\theta^*\frac{D^3}{3}+k_x^*u_{ff}^*\left(\frac{B}{a_o}D\sin(a_o\frac{D}{B})+\left(\frac{B}{a_o}\right)^2\left(\cos(a_o\frac{D}{B})-1\right)\right)-k_{bx}^*Du_t^*+k_{bx}^*\theta^* D^2$$
$$+k_{bx}^*u_{ff}^*D\cos(a_o\frac{D}{B})+k_\theta^*D\theta^*-k_\theta^*u_{ff}^*\left(\cos(a_o\frac{D}{B})-1\right)+k_{b\theta}^*\theta^*+k_{b\theta}^*u_{ff}^*\frac{a_o}{B}\sin(a_o\frac{D}{B})=0$$

which can be simplified to the following expression:

$$u_t^*\left(-k_x^*\frac{D^2}{2}-k_{bx}^*D\right)+\theta^*\left(k_x^*\frac{D^3}{3}+k_{bx}^*D^2+k_\theta^*D+k_{b\theta}^*\right)=$$

$$u_{ff}^*\begin{bmatrix} k_x^*\left(\frac{B}{a_o}\right)^2\left(\left(1-\cos(a_o\frac{D}{B})\right)-a_o\frac{D}{B}\sin(a_o\frac{D}{B})\right)-... \\ ...-k_{bx}^*D\cos(a_o\frac{D}{B})-k_\theta^*\left(1-\cos(a_o\frac{D}{B})\right)-k_{b\theta}^*\frac{a_o}{B}\sin(a_o\frac{D}{B}) \end{bmatrix} \tag{7.4}$$

Equations 7.3 and 7.4 can be written in matrix form as

$$\begin{bmatrix} K_{xx}^* & K_{xr}^* \\ K_{xr}^* & K_{rr}^* \end{bmatrix}\begin{bmatrix} u_t^* \\ \theta^* \end{bmatrix}=\begin{bmatrix} V_{eff}^* \\ M_{eff}^* \end{bmatrix} \tag{7.5}$$

where the effective forces are formulated as follows:

$$V_{eff}^*=u_{ff}^*\left(k_x^*\frac{B}{a_o}\sin(a_o\frac{D}{B})+k_{bx}^*\cos(a_o\frac{D}{B})\right)$$

$$M_{eff}^*=u_{ff}^*\begin{bmatrix} k_x^*\left(\frac{B}{a_o}\right)^2\left(\left(1-\cos(a_o\frac{D}{B})\right)-a_o\frac{D}{B}\sin(a_o\frac{D}{B})\right)-... \\ ...-k_{bx}^*D\cos(a_o\frac{D}{B})-k_\theta^*\left(1-\cos(a_o\frac{D}{B})\right)-k_{b\theta}^*\frac{a_o}{B}\sin(a_o\frac{D}{B}) \end{bmatrix} \tag{7.6}$$

In non-dimensional form, Equations 7.5 and 7.6 can be written as

$$\begin{bmatrix} \frac{K_{xx}^*}{EB} & \frac{K_{xr}^*}{EB^2} \\ \frac{K_{xr}^*}{EB^2} & \frac{K_{rr}^*}{EB^3} \end{bmatrix}\begin{bmatrix} \frac{u_t^*}{B} \\ \theta^* \end{bmatrix}=\begin{bmatrix} \frac{V_{eff}^*}{EB^2} \\ \frac{M_{eff}^*}{EB^3} \end{bmatrix} \tag{7.7}$$

$$\frac{V_{eff}^*}{EB^2}=\frac{u_{ff}^*}{B}\left(\frac{k_x^*}{E}\frac{1}{a_o}\sin(a_o\frac{D}{B})+\frac{k_{bx}^*}{EB}\cos(a_o\frac{D}{B})\right)$$

$$\frac{M_{eff}^*}{EB^3}=\frac{u_{ff}^*}{B}\begin{bmatrix}\frac{k_x^*}{E}\left(\frac{1}{a_o}\right)^2\left(\left(1-\cos(a_o\frac{D}{B})\right)-a_o\frac{D}{B}\sin(a_o\frac{D}{B})\right)-\frac{k_{bx}^*}{EB}\frac{D}{B}\cos(a_o\frac{D}{B})-\ldots\\ \ldots-\frac{k_\theta^*}{EB^2}\left(1-\cos(a_o\frac{D}{B})\right)-\frac{k_{b\theta}^*}{EB^3}a_o\sin(a_o\frac{D}{B})\end{bmatrix} \tag{7.8}$$

The transfer functions can thus be written as

$$\begin{bmatrix}H_u(a_o)\\ H_\theta(a_o)\end{bmatrix}=\begin{bmatrix}\left|\frac{u_t^*}{u_{ff}}\right|\\ \left|\frac{\theta^* B}{u_{ff}}\right|\end{bmatrix}=\left|\begin{bmatrix}\frac{K_{xx}^*}{EB} & \frac{K_{xr}^*}{EB^2}\\ \frac{K_{xr}^*}{EB^2} & \frac{K_{rr}^*}{EB^3}\end{bmatrix}^{-1}\begin{bmatrix}f_1^*\\ f_2^*\end{bmatrix}\right| \tag{7.9}$$

where

$$f_1^*=\left(\frac{k_x^*}{E}\frac{1}{a_o}\sin(a_o\frac{D}{B})+\frac{k_{bx}^*}{EB}\cos(a_o\frac{D}{B})\right) \tag{7.10}$$

$$f_2^*=\begin{bmatrix}\frac{k_x^*}{E}\left(\frac{1}{a_o}\right)^2\left(\left(1-\cos(a_o\frac{D}{B})\right)-a_o\frac{D}{B}\sin(a_o\frac{D}{B})\right)-\frac{k_{bx}^*}{EB}\frac{D}{B}\cos(a_o\frac{D}{B})-\ldots\\ \ldots-\frac{k_\theta^*}{EB^2}\left(1-\cos(a_o\frac{D}{B})\right)-\frac{k_{b\theta}^*}{EB^3}a_o\sin(a_o\frac{D}{B})\end{bmatrix} \tag{7.11}$$

## 6.3 Comparison with 3D finite element simulation results

Three dimensional finite element numerical simulations were performed to evaluate the transfer functions $H_u$ and $H_\theta$ for vertically propagating SH waves. The far-field motion is applied in the form of effective forcing functions in the interior of the truncated numerical domain, as discussed in Chapter 3. A comparison with the values derived by means of the analytical expression using both fitted and numerically derived unfitted spring constants is shown in **Figure 7.3 (a), (b**) for D/B =2 and **Figures 7.4(a), (b)** for D/B =4.

From the results illustrated above, it can be readily seen that using the analytical solution for the kinematic response of rigid intermediate embedded foundations and the numerically derived fitted spring functions, the kinematic interaction for pier foundation elements may be captured to a certain degree of accuracy. Despite the fact that the 3D finite element simulations show values that deviate from the analytically derived ones (even on the order of 50% for the case of rocking motions), the following conclusions are drawn:

(a) The model predicts the frequencies corresponding to maxima and minima of transfer functions with sufficient accuracy;

(b) The values predicted by the model are for the most part conservative, i.e., lower reduction in translational motion and higher induced rocking motions, and show substantial improvement from the assumption of no kinematic interaction; and

(c) The results are bounded by the transfer functions obtained using Elsabee and Morray (1977) approximation for shallow foundations and Gazetas (1993) simple Winkler spring model for pile foundations

$$k_x = 1.2E \text{ or } \frac{k_x}{E} = 1.2$$

$$C_x = 1.6\rho V_s B\left(\frac{\omega B}{V_s}\right)^{-0.25} \text{ or } \frac{\omega C_x}{E} = 0.62 a_o^{0.75}$$

which is as expected but still none of the approaches captures the actual response as good as the proposed model. This further highlights the importance of a separate model for caisson foundations.

Using the analytical formulation and the fitted spring values, the transfer functions can be easily programmed into a simple script (see MATLAB script attached in APPENDIX A) and can be used to predict -to a first approximation- the pier response subjected to transient excitation or earthquake loading given the aspect ratio of the foundation D/B.

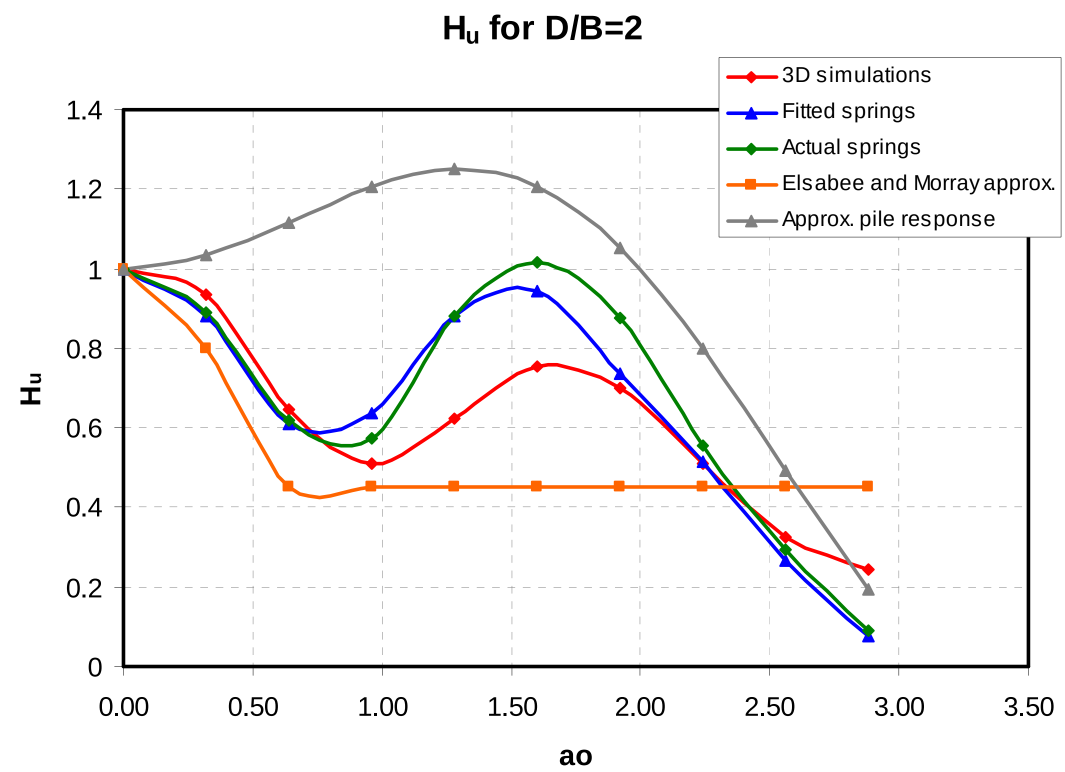


**Figure 7.3 (a)** Displacement transfer function for D/B =2

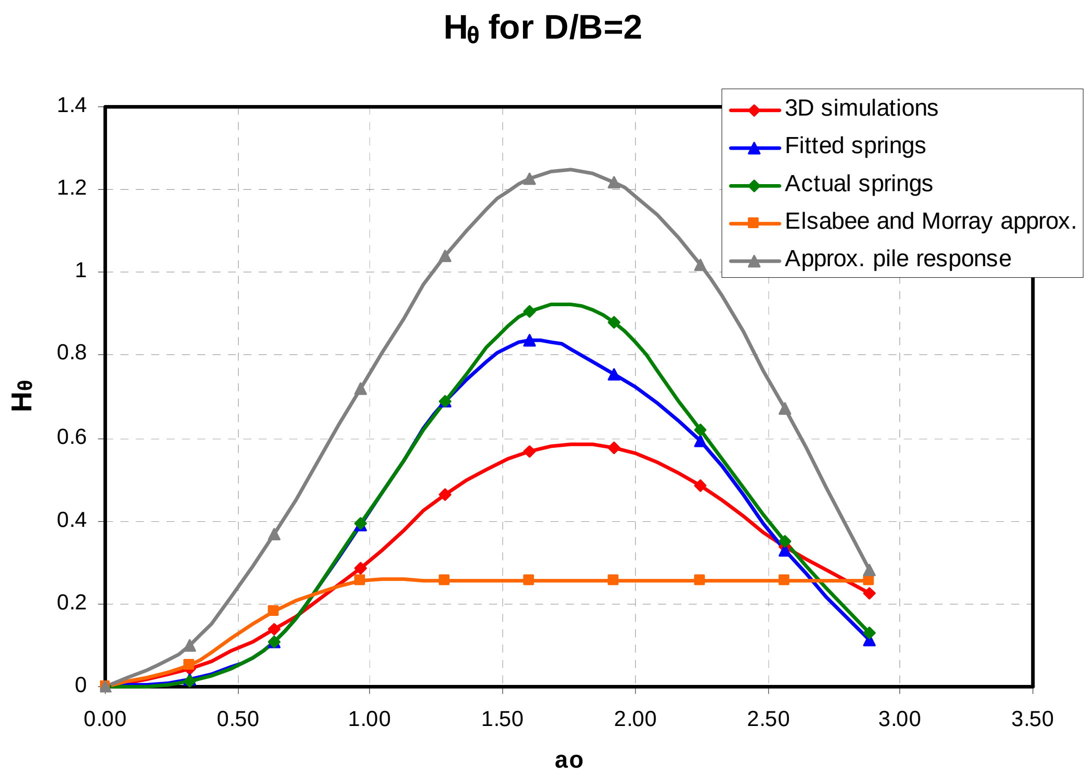


**Figure 7.3 (b)** Rotation transfer function for D/B =2

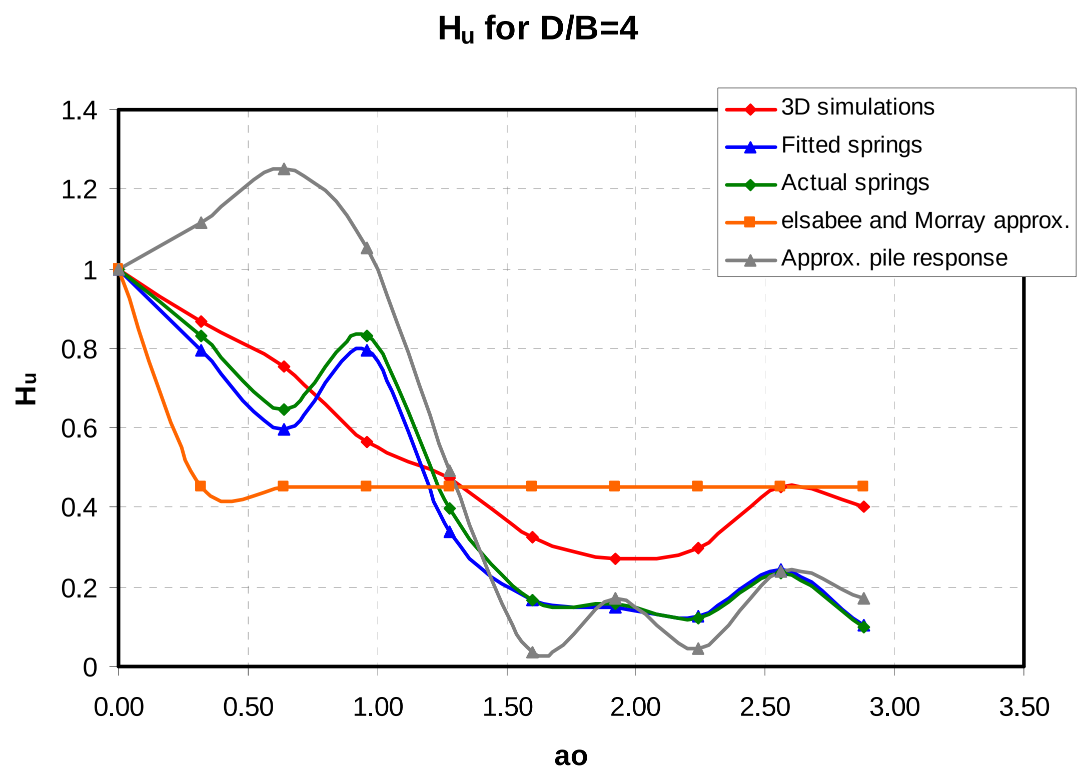


**Figure 7.4 (a)** Displacement transfer function for D/B =4

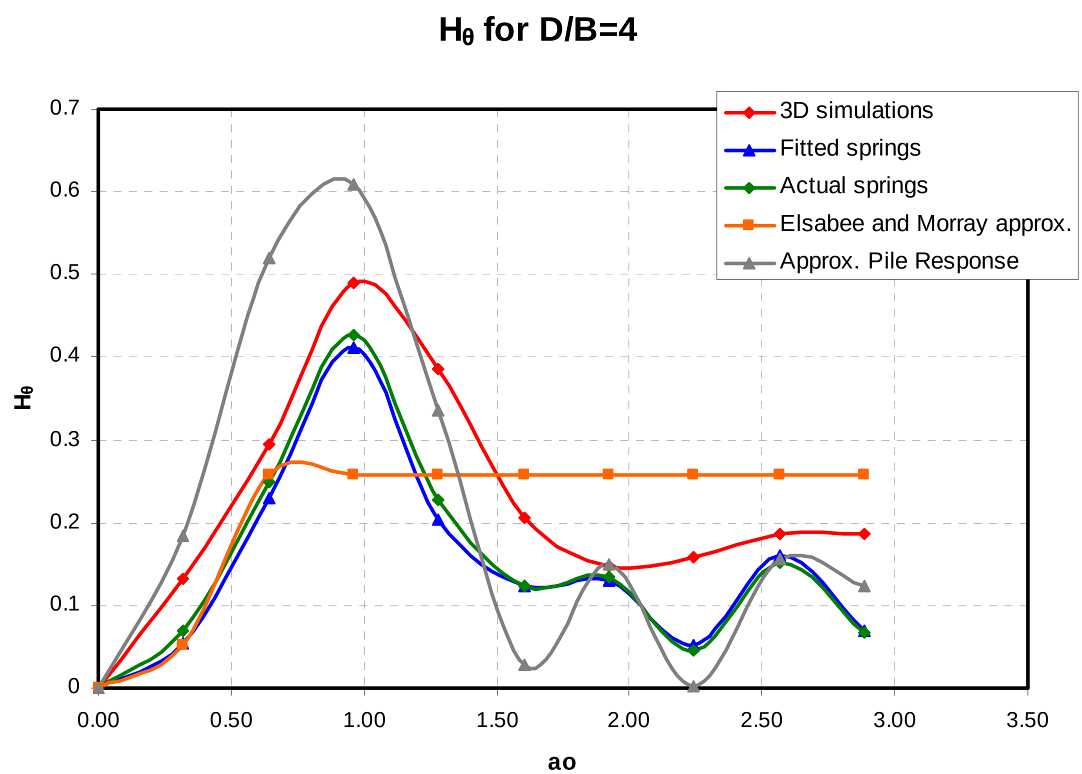


**Figure 7.4 (b)** Rotation transfer function for D/B =4

# CHAPTER 8

# APPLICATIONS OF THE PROPOSED MODEL

In this chapter, we present applications of the proposed model and coefficients of soil reaction for the estimation of the static and dynamic response of pier foundations in multi-layered profiles, and the kinematic response of the foundation elements to incident transient seismic motion. Results are also evaluated by means of three-dimensional finite element simulations, and compared to the proposed methodology.

## 8.1 Static Loading: Multi layered soil profile

Initially, we examine the soil-structure interaction problem for the layered profile shown in **Figure 8.1**, where the stiffness of the three layers is $E_1$=10 MPa, $E_2$=30 MPa and $E_3$=50 MPa respectively. The thickness of the top layer is $d_1$= 3m, the thickness of the second layer is $d_2$=4m; the two layers are overlying a linear elastic halfspace. The diameter of pier B = 2 m and the depth of embedment D = 8 m.

A lateral load of 1000 kN and an overturning moment of 2000 kN.m are applied at the top of the caisson, and the response of the foundation element is here evaluated using the proposed three-spring model for intermediate foundations.

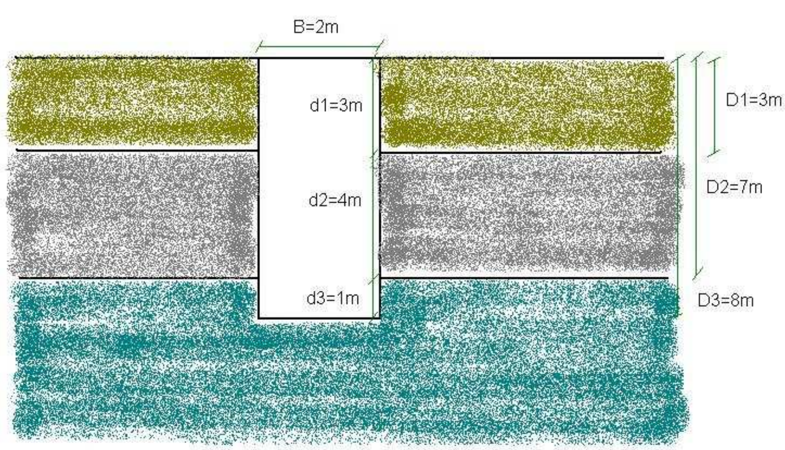


**Figure 8.1** The layered soil profile considered in Problem 1 and 2

Using the model proposed, the distributed translational springs are given as:

$$k_{xi} = 1.83\left(\frac{D}{B}\right)^{-0.15} E_i$$

and for the three formations of the layered medium, the corresponding values are:

$k_{x1}$ = 14.9 MPa, $k_{x2}$ = 44.6 MPa and $k_{x3}$ = 74.3 MPa.

The translational stiffness at the base of the foundation is given by the following expression:

$$k_{bx} = \left[0.67 + 0.13\left(\frac{D}{B}\right)\right] E_3 B = 119 \text{ MPa.m}$$

Finally, the distributed rotational springs are evaluated for each layer as follows:

$$k_{\theta i} = \left[1.11 + 0.23\left(\frac{D}{B}\right)\right] E_i B^2$$

and the corresponding values are computed as:

$k_{\theta 1}$ = 81.2 MPa.m$^2$, $k_{\theta 2}$ = 243.6 MPa.m$^2$ and $k_{\theta 3}$ = 406 MPa.m$^2$.

Using $D_1 = d_1 = 3$m

$D_2 = d_1 + d_2 = 7$m

$D_3 = d_1 + d_2 + d_3 = 8$m

the overall stiffness of the foundation element as interpreted from the top of the caisson is computed from the following expressions:

$$K_{xx} = k_{x1}D_1 + k_{x2}(D_2 - D_1) + k_{x3}(D_3 - D_2) + k_{bx} = 416.4 \text{ MPa.m}$$

$$K_{xr} = -\left[k_{x1}\frac{D_1^2}{2} + k_{x2}\left(\frac{D_2^2 - D_1^2}{2}\right) + k_{x3}\left(\frac{D_3^2 - D_2^2}{2}\right) + k_{bx}D_3\right] = \text{-2468.3 Mpa.m}^2$$

$$K_{rr} = k_{x1}\frac{D_1^3}{3} + k_{x2}\left(\frac{D_2^3 - D_1^3}{3}\right) + k_{x3}\left(\frac{D_3^3 - D_2^3}{3}\right) + k_{bx}D_3^2 = 18257.5 \text{ MPa.m}^3$$
$$+ k_{\theta 1}D_1 + k_{\theta 2}(D_2 - D_1) + k_{\theta 2}(D_3 - D_2)$$

In a matrix form, the displacement-force relation of the foundation-soil system is:

$$\begin{bmatrix} u_t \\ \theta \end{bmatrix} = \begin{bmatrix} K_{xx} & K_{xr} \\ K_{rx} & K_{rr} \end{bmatrix}^{-1} \begin{bmatrix} V \\ M \end{bmatrix}$$

and substituting the corresponding values of the stiffness matrix and externally applied loads at the top, the response is computed as:

$$\mathbf{u_t = 0.0153\ m = 1.53\ cm}$$

$$\boldsymbol{\theta} \mathbf{= 0.00218\ rad}$$

Results of the 3D finite element simulation for the same configuration and externally applied loading correspond to the following response at the top of the caisson:

$$\mathbf{u_{t\,[NUM]} = 0.0178\ m = 1.78\ cm}$$

$$\boldsymbol{\theta}_{\mathbf{[NUM]}} \mathbf{= 0.00239\ rad}$$

The analytically obtained values deviate from the numerical results by a factor of 10-15%. As can be readily seen, the assumption of individually responding soil layers may be applied with no significant loss of accuracy, and thus the model can be employed for the case of multi-layered soil profiles.

## 8.2 Dynamic Loading: layered soil profile

For the same configuration described above, we here evaluate the pier response to a dynamic steady-state lateral load applied at the top of the foundation, with amplitude 1000 kN and frequency 5 Hz.

The density of layers 1, 2 and 3 is assumed to be 1500, 1600 and 1800 kg/m$^3$ respectively, whereas a common Poisson's ratio is assumed throughout the medium and equal to $\nu$=0.3.

The shear wave velocity of the soil layers and the dimensionless frequency describing the soil resistance and radiation damping dependence on the frequency content of the pier response are calculated as:

$$V_s = \sqrt{\frac{E}{2(1+\nu)\rho}} \text{ and } a_o = \frac{2\pi f B}{V_s}$$

Therefore, for each layer the corresponding values are:

$V_{s2}$ = 50 m/s $a_{o1}$ = 1.25

$V_{s2}$ = 85 m/s $a_{o2}$ = 0.74

$V_{s3}$ = 103 m/s $a_{o3}$ = 0.61

Given the dependency of stiffness and attenuation coefficients on the frequency content of the pier response, namely:

$$k_x^{'} = 1 - 0.1a_o \qquad C_x = \begin{cases} 1.85a_o & a_o < 1 \\ 1.85 & a_o > 1 \end{cases}$$

$$k_{bx}^{'} = 1 \qquad C_{bx} = \begin{cases} 0.6a_o & a_o < 0.6 \\ 0.36 & a_o > 0.6 \end{cases}$$

$$k_\theta^{'} = 1 - 0.225a_o \qquad C_\theta = \begin{cases} -0.21\left(\tfrac{D}{B}\right)a_o & a_o < 1 \\ -0.21\left(\tfrac{D}{B}\right)(2-a_o) & 1 < a_o < 2 \\ 0 & a_o > 2 \end{cases}$$

The dynamic springs (distributed translational, base translational and distributed rotational stiffness and attenuation coefficients) in this case are calculated as:

$k_{x1}^{*}$ = 13.04 + 23.12 i, $k_{x2}^{*}$ = 41.30 + 30.39 i, and $k_{x3}^{*}$ = 69.77 + 34.42 i

$k_{bx}^{*}$ = 119.0 + 21.96 i

$k_{\theta 1}^{*}$ = 58.36 – 31.5 i, $k_{\theta 2}^{*}$ = 203.04 – 55.20 i, and $k_{\theta 3}^{*}$ = 350.27 – 61.51 i

Using the above values, the global stiffness matrix can be written as

$K_{xx}^{*} = 393.1 + 247.3\,i$

$K_{xr}^{*} = -2359.9 - 1145.7\,i$

$K_{rr}^{*} = 17351.3 + 6735.9\,i$

Using the displacement-loading system of equations described in 8.1 and solving for the complex response of the foundation, the resulting amplitude predicted by the proposed model is:

$$\left|u_t\right| = \mathbf{0.011\ m = 1.1\ cm}$$

$$\left|\theta\right| = \mathbf{0.00147\ rad}$$

Results of the 3D finite element simulation for the same configuration and externally applied loading correspond to the following response at the top of the caisson:

$$\left|u_t\right|_{[\mathrm{NUM}]} = \mathbf{0.015\ m = 1.4\ cm}$$

$$\left|\theta\right|_{[\mathrm{NUM}]} = \mathbf{0.00186\ rad}$$

Based on the comparison presented above, the model may be employed to predict the dynamic response with fair accuracy. Despite the fact that the presence of multiple layers causes multiple reflections of waves at the interfaces arising from the impedance contrast, it appears that the radiated waves are primarily parallel to the layer interfaces (except for the base spring for which they are normal to the interface). As a result, the layers act more like a waveguide for waves moving away from the pier and layering has little effect on the total response.

### 8.3 Response to a transient seismic loading

As discussed in Section 7.3, the analytical expressions developed for the load-displacement and rotation transfer functions of the pier response caused by vertically propagating SH seismic waves in the free field may be easily implemented in a computer script (e.g. MATLAB) and successively be used to calculate the motions corresponding to any transient loading by means of Fourier reconstruction of the response signal, provided that the medium of propagation is linear elastic or moderately nonlinear.

This section presents a comparison between the pier response obtained by means of the analytical kinematic response formulation using the approximated spring formulae developed in this study, and the numerically evaluated response by means of 3D finite element time-domain simulations.

**Figures 8.2a** and **b** show the applied free-field displacement time history and Fourier transform correspondingly. The comparison between the analytically-predicted and numerically-evaluated response is shown in **Figures 8.3 and 8.4**.

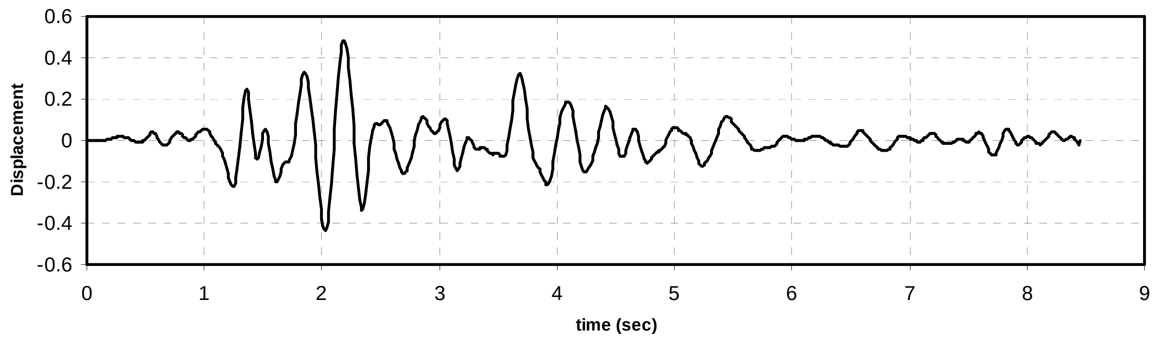


**Figure 8.2a** The displacement time history applied to free-field

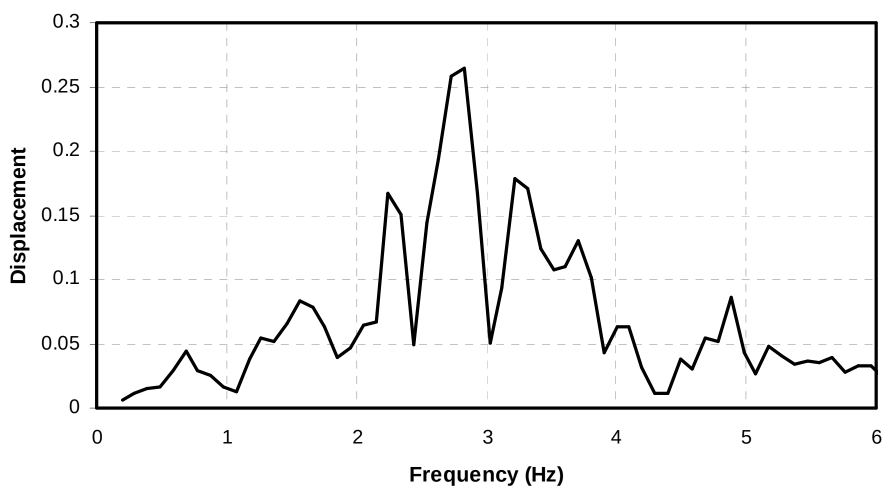


**Figure 8.2b** Fourier spectrum of free-field displacement time history

In particular, **Figures 8.3a-b** show the theoretically predicted and numerically-computed time histories of the pier displacement at the top and the pier rotation. The numerically-obtained time histories have been shifted in time to account for the wave propagation duration of the excitation traveling from the far-field to the pier. The Fourier spectra of the translational motion are compared in **Figure 8.4 (a)** and for the rocking motion in **Figure 8.4 (b)**.

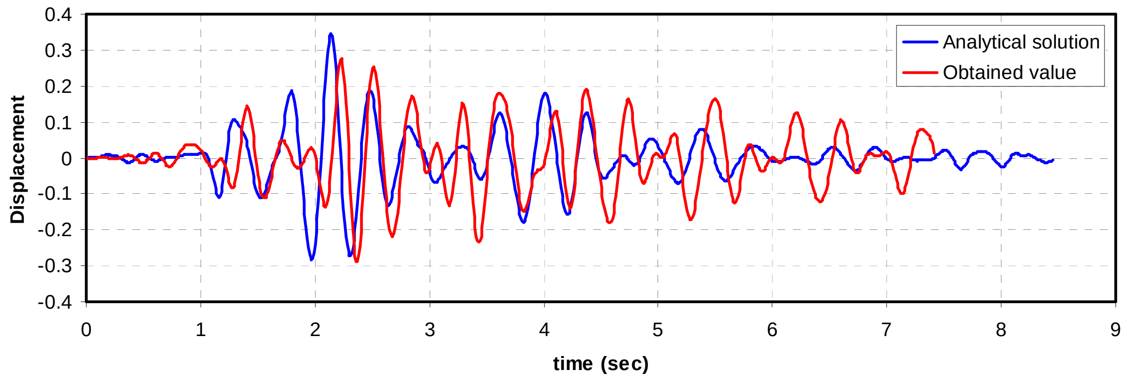


**Figure 8.3a** Comparison between obtained and theoretically predicted translation motion at the top of pier.

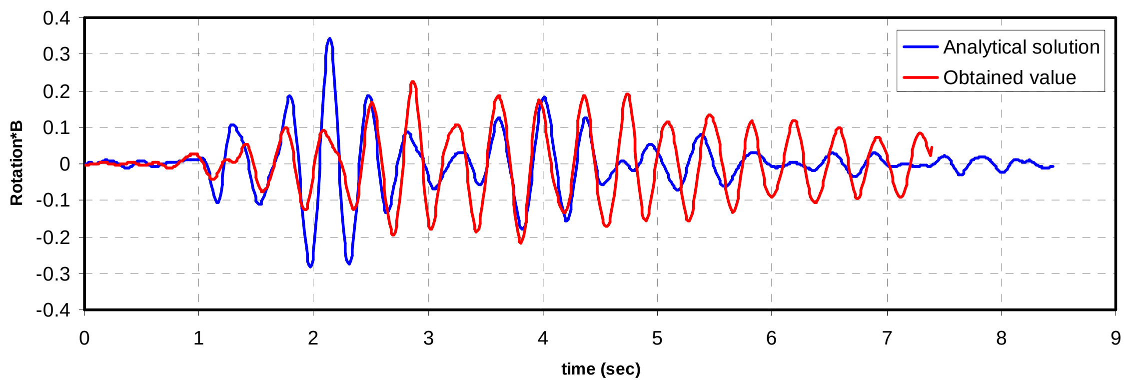


**Figure 8.3b** Comparison between obtained and theoretically predicted rocking motion of pier.

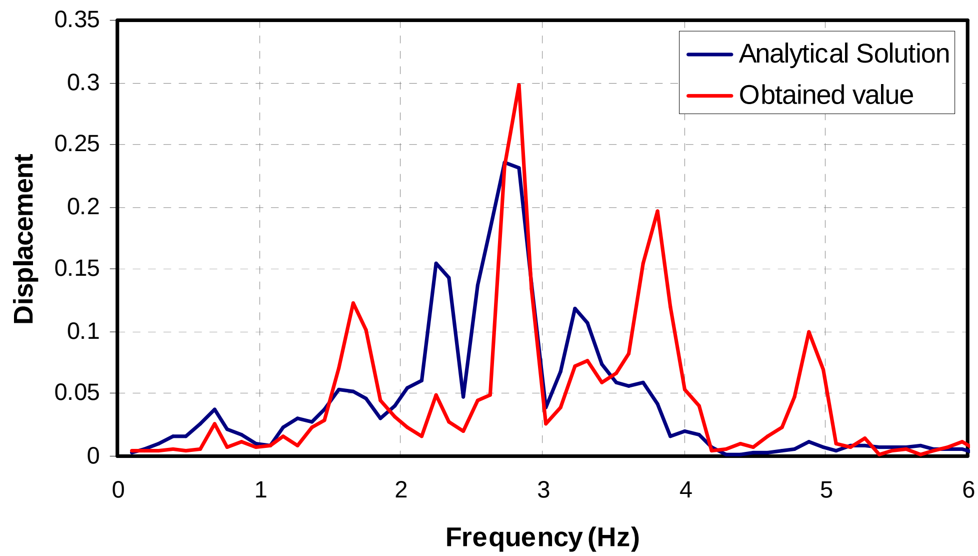


**Figure 8.4a** Comparison between Fourier spectra (obtained from numerical simulation and analytical model predictions) for translational motion at the top of pier

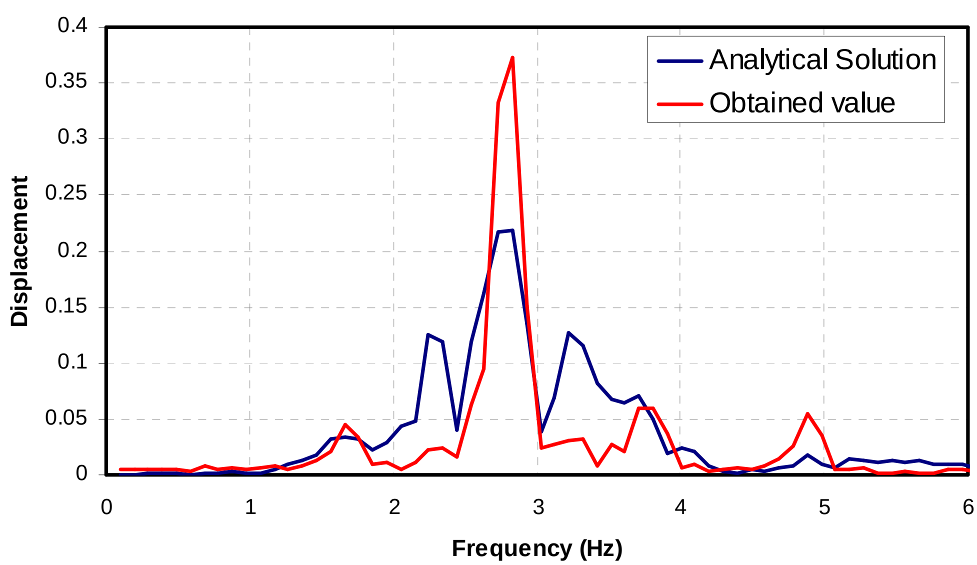


**Figure 8.4b** Comparison between Fourier spectra (obtained from numerical simulation and analytical model predictions) for rocking motion of pier

From the comparison of results presented above, it can be readily seen that that the model is able to capture the response of pier within an acceptable degree of prediction accuracy. In particular, the dominant frequency in both translational and rocking motion response evaluated by means of the analytical model is in excellent agreement with the numerical results. However, the maximum translation predicted by the analytical model is 0.37m which is higher compared to the numerically-obtained value, namely $u_{max}$ = 0.23m. Also, the pier rotation is predicted to be 0.34rad by means of the analytical model and 0.22rad is obtained by means of the numerical simulations. Overall, the results predicted are conservative (higher translations and higher rotations than the numerical model predicts) but still they are much better approximation than the simulation of the response in absence of kinematic interaction effects.

# CHAPTER 9

# CONCLUSIONS AND FUTURE

## 9.1 Conclusions

In this study, we developed an analytical model to be employed for the prediction of the response of rigid cylindrical caisson foundations characterized by aspect ratios D/B = 2-6 and embedded in linear elastic soil media, using a simple Winkler spring model with four springs namely:

(a) $k_x$: Lateral translational springs used to characterize lateral force-displacement response of soil;

(b) $k_\theta$: Rotational springs used to characterize the moment developed at the centerline of pier due to vertical shear stress acting at the perimeter of pier, induced by pier rotation;

(c) $k_{bx}$: Base translational spring used to characterize horizontal shear force-base displacement response; and

(d) $k_{b\theta}$: Base rotational spring used to characterize moment developed due to normal stress acting at the base of pier, induced by base rotation.

Based on the results obtained in this study, we have conclude that for the range aspect ratio of interest (D/B = 2-6), the effect of base rotational spring is negligible and therefore, a simplified three spring model may instead be used to capture the pier response with sufficient accuracy. Approximate expressions have been developed for the three springs as a function of both the D/B ratio and the dimensionless frequency. The expressions of the static springs are given by the following expressions:

$$\frac{k_x}{E} = 1.828\left(\frac{D}{B}\right)^{-0.15}$$

$$\frac{k_{bx}}{EB} = 0.669 + 0.129\left(\frac{D}{B}\right)$$

$$\frac{k_\theta}{EB^2} = 1.106 + 0.227\left(\frac{D}{B}\right)$$

For dynamic loading applied at the foundation top, the springs are expressed as dynamic impedances, namely:

$$K^* = K_{stat} k'(a_o) + i a_o C(a_o)$$

where

$$k_x' = 1 - 0.1a_o \qquad C_x = \begin{cases} 1.85a_o & a_o < 1 \\ 1.85 & a_o > 1 \end{cases}$$

$$k_{bx}' = 1 \qquad C_{bx} = \begin{cases} 0.6a_o & a_o < 0.6 \\ 0.36 & a_o > 0.6 \end{cases}$$

$$k_\theta' = 1 - 0.225a_o \qquad C_\theta = \begin{cases} -0.21\left(\frac{D}{B}\right)a_o & a_o < 1 \\ -0.21\left(\frac{D}{B}\right)(2 - a_o) & 1 < a_o < 2 \\ 0 & a_o > 2 \end{cases}$$

The global dynamic impedance matrix of the pier is then expressed in terms of the distributed translational, rotational and base concentrated springs as:

$$\frac{K_{xx}}{EB} = \frac{k_x}{E}\left(\frac{D}{B}\right) + \frac{k_{bx}}{EB}$$

$$\frac{K_{xr}}{EB^2} = -\left[\frac{1}{2}\frac{k_x}{E}\left(\frac{D}{B}\right)^2 + \frac{k_{bx}}{EB}\left(\frac{D}{B}\right)\right]$$

$$\frac{K_{rr}}{EB^3} = \left[\frac{1}{3}\frac{k_x}{E}\left(\frac{D}{B}\right)^3 + \frac{k_{bx}}{EB}\left(\frac{D}{B}\right)^2 + \frac{k_\theta}{EB^2}\left(\frac{D}{B}\right) + \frac{k_{b\theta}}{EB^3}\right]$$

Using the global impedance matrix, the response of the pier subjected to any static or dynamic loading may be obtained, which was shown to be in good agreement with numerically evaluated results of the configuration subjected of the same externally applied loading.

Successively, accounting for the motion incompatibility between the pier and the free field response upon the incidence of vertically propagating anti-plane shear waves, an analytical formulation was obtained for the Winkler spring model kinematic response. The theoretical values of free-field/pier response transfer functions for translational and rocking motion resulting from the free field excitation were compared to the corresponding values obtained by means of 3D finite element simulations. Despite the fact that the proposed formulation does not simulate the pier response exactly, a fact that is attributed to the complex load transfer mechanisms applied at the soil-foundation interface that cannot be captured by the simplified 3-spring proposed model, it may be applied to capture the important response parameters, namely the frequency content and evolution of time-history variation.

In conclusion, we have developed a simple approach that may be used for the evaluation of the response of intermediate embedded foundations instead of the heretofore employed; the simplicity of the approach, the applicability of the methodology for multi-layered media and seismic incident motion, as well as the advantages compared to the embedded foundations or pile theoretical solutions for the analysis of caisson foundations, render the proposed model suitable for the design and performance evaluation of these elements for low and intermediate levels of target degree of accuracy required for non-critical facilities.

## 9.2 Future work

1) The Winkler springs developed in this study are applicable for linear elastic medium with no material damping. Nonetheless, the effect of material damping can be easily accounted for using the elasticity-visco-elasticity correspondence principle. According to this principle, the elasticity modulus can be expressed as a complex modulus given by

   $$E^* = E(1 + i2D')$$

   where D’ is the material damping ratio.

2) The current approach assumes no separation between the soil and pier interface. Nonetheless, modified Winkler springs that include a stiffness element, a damper and a Coulomb friction element with low tension resistance may be developed to take into account the separation at the soil-foundation interface.

3) The approach may be further extended to capture the non-linearities in soil behavior by the use of non-linear springs. It should be noted, however, that in the case of kinematic interaction, a first approximation to the nonlinear response of the soil-foundation system (provided that the foundation material is always responding within the linear elastic range) would be the application of equivalent linear analyses (e.g. by means of the computer program SHAKE, Schnabel et al, 1972) in the far-field, which would then be used as the effective forcing function at the base and soil-foundation interface for the reduced stiffness and material damping evaluated at convergence of the algorithm.

4) Based on the developed computational platform, analytical formulations may also be developed for the motion-response transfer functions of the pier subjected to horizontally propagating coherent SH waves or for different geometries of foundation cross-sections.

# APPENDIX A

# MATLAB SCRIPT FOR RESPONSE TO TRANSIENT FREE FIELD EXCITATION

## A.1 Transfer function to calculate displacement and rotation for a given dimensionless frequency and D/B ratio.

---

```
function Y = transfxn(a,D)

    if (a < 1.0)
       kx = 1.828*D^(-0.15)*(1-0.1*a) + i*1.85*a*a;
    else
       kx = 1.828*D^(-0.15)*(1-0.1*a) + i*1.85*a;
    end

    if (a < 0.6)
       kbx = 0.669+0.129*D+i*0.6*a*a;
    else
       kbx = 0.669+0.129*D+i*0.36*a;
    end

    if (a < 1.0)
       kt = (1.106+0.227*D)*(1-0.225*a)-i*0.21*D*a*a;
    elseif (a < 2.0)
       kt = (1.106+0.227*D)*(1-0.225*a)-i*0.21*D*(2.0-a)*a;
    else
       kt = (1.106+0.227*D)*(1-0.225*a)-i*a*0;
    end

    Kxx = kx*D+kbx;

    Kxr = -1*(kx*D^2)/2-1*kbx*D;

    Krr = (kx*D^3)/3+kbx*D^2+kt*D;

    f1 = kx*sin(a*D)/a + kbx*cos(a*D);

    f2 = kx/(a^2)*((1-cos(a*D))-a*D*sin(a*D))-kbx*D*cos(a*D)-kt*(1-cos(a*D));
```

```
      f11 = Krr/(Kxx*Krr-Kxr^2);

      f12 = -1*Kxr/(Kxx*Krr-Kxr^2);

      f22 = Kxx/(Kxx*Krr-Kxr^2);

   if (a == 0)
      Y(1,1)=1;
      Y(1,2)=0;
      Y(2,1)=0;
      Y(2,2)=0;
   else
      u =f1*f11+f2*f12;
      t =f1*f12+f2*f22;
      Y(1,1)=real(u);
      Y(1,2)=imag(u);
      Y(2,1)=real(t);
      Y(2,2)=imag(t);
   end

end
```
--------------------------------------------------------------------------------------------------------

## A.2 Response function to calculate the response of pier to a given transient free field loading

The following parameters are needed

(a) A: The loading time history
(b) dt: Time step in loading time history
(c) B: Diameter of pier
(d) D: D/B ratio of foundation
(e) Vs: shear wave velocity of soil

--------------------------------------------------------------------------------------------------------
```
function Y = response(A,dt,D,vs,B)
N = length(A);
da = 2*pi*B/(N*dt*vs);
FA = fft(A);
FT(1)=FA(1);
FR(1)=0;
for p=2:N/2+1
   temp = transfxn((p-1)*da,D);
   FT(p)=FA(p)*(temp(1,1)+i*temp(1,2));
   FT(N+2-p)=FA(N+2-p)*(temp(1,1)-i*temp(1,2));
   FR(p)=FA(p)*(temp(2,1)+i*temp(2,2));
```

```
    FR(N+2-p)=FA(N+2-p)*(temp(2,1)-i*temp(2,2));
end
Y(:,1) = real(ifft(FT));
Y(:,2) = real(ifft(FR));
Y(:,3) = imag(ifft(FT));
Y(:,4) = imag(ifft(FR));
End
```

-----------------------------------------------------------------------------------------------------------

# REFERENCES


ABAQUS User's Manual (1992) Pawtucket, Rhode Island

Bettes, P. and Bettess, J.A. (1984) Infinite elements for static problems, Engineering Computations, 1:4-16.

Christensen, RM (1971) Theory of Viscoelasticity: An Introduction, Academic Press, NY

Davidson, H.L. (1982) Laterally Loaded Drilled Pier Research, Research Rep. EL-2197, EPRI

Day, S.M. (1977). "Finite element analysis of seismic scattering problems," *Ph.D. Dissertation*, Univ. of California, San Diego.

Dobry, R. and Gazetas, G. (1986), Dynamic Response of arbitrary shaped foundations. ASCE Journal of Geotechnical Engineering, Vol. 112, No. 2, pp.109-135

Elsabee, F and Morray, J.P. (1977) Dynamic behavior of embedded foundations, Research Rep. R77-33, MIT

Gazetas, G. (1983) "Analysis of Machine Foundation Vibrations: state of the art," J. Soil Dynamics and Earthquake Engng., 2, 2-42.

Gazetas, G., Fan, K. and Kynia, A. (1993) Dynamic response of pile groups with different configurations, J. Soil Dynamics and Earthquake Engng., 12, pp. 239-257

Hibbitt,. Karlsson and Sorensen (1995) ABAQUS: Finite Element analysis Program

Kausel, E. (1974) Forced vibrations of circular foundations on layered media, Research Rep. R74-11, MIT

Kausel E and Rosset JM (1975) Dynamic stiffness of circular foundations. . J. Eng Mech Div, ASCE, 101(6): 770-85

Kausel, E. and Ushijima, R. (1979) Vertical and torsional stiffness of cylindrical footing, Research Rep. R79-6, MIT

Lam, I.P. and Chaudhury, D. (1997) “Modeling of drilled shafts for seismic design” NCEER reprt for task no II-2D-2.5, NCEER, SUNY Buffalo.

Luco, J. E. (1974) “Impedance Functions for a Rigid Foundations on a Layered Medium,” Nuclear Engineering and Design, 31, 204-217.

Luco, J.E. and Westmann, R.A. (1971) Dynamic response of circular footings, J. Engrg. Mech. Div. ASCE, 97.EM5, 1381

Mita, A. and Luco, J. E. (1989) Dynamic response of a square foundation embedded in an elastic halfspace”, Soil Dynamics and earthquake engineering, 8(2), 54-67.

Novak M, Nogami T and Aboul-Ella (1978) F. Dynamic soil reactions for plane strain case. J. Eng Mech Div, ASCE, 104(4): 953-9

O’Neil, M.W. and Reese L.C. (1999) Drilled shaft: Construction procedures and design methods, Research Rep. FHWA-IF-99-025

Prevost, J.H. (1983) Dynaflow. Princeton University, Princeton, NJ 08544

Roesset, J.M. (1975) Dynamic Stiffness of Circular Foundations, Journal of the Engineering Mechanics Division, ASCE, Vol. 101(6), 771-785.

Schnabel, P.B., J. Lysmer, and H.B. Seed (1972): “SHAKE: a computer program for earthquake response analysis of horizontally layered sites,” Report EERC 72-12, Earthquake Engineering Research Center, University of California, Berkeley.

Stewart, J.P., Seed, R.B. and Fenves, G.L. (1998) Empirical Evaluation of Inertial Soil Structure Interaction Effects, Research Rep. PEER-98/07, UCB

Velestos, A.S. and Verbic, B. (1974) Basic response functions for elastic foundations, J.Engrg. Mech. Div, ASCE, 100, EM2, 189

Velestos, A.S. and Wei, Y.T. (1971) Lateral and rocking vibrations of footings, J. Soil Mech. Found. Div., ASCE, 97, SM9, 1227.

Wolf, J.P. (1997) Spring-Dashpot-Mass models for foundation Vibrations, Earthquake Engg. and Structural Dynamics, Vol. 26, pp. 931-949

Wong, H. L and Luco, J. E., (1985) “Tables of Impedance Functions for Square Foundation on Layered Media,” Soil Dynamics and Earthquake Engng., 4, 64-8